ABSTRACT

Title of dissertation: NONLINEAR SELF-CHANNELING
OF HIGH-POWER LASERS
THROUGH TURBULENT ATMOSPHERES

Gregory P. DiComo, Doctor of Philosophy, 2018

Dissertation directed by: Professor Thomas Antonsen
Department of Electrical and Computer Engineering

A variety of laser applications have been considered which depend on long-distance atmospheric propagation of the beam to attain practical utility. The effectiveness of these applications is limited to some extent by beam distortions caused by atmospheric optical turbulence. Often the limiting factor is the instantaneous beam spreading due to turbulence, which makes it impossible to create a small laser spot at the receiver.

In the absence of turbulence, laser beams of sufficient peak power propagating in atmosphere have been shown to undergo nonlinear self-guiding, in which the beam size remains constant over multiple Rayleigh lengths. Recent research suggests that self-guiding beams of sufficiently small diameter might exhibit resistance to turbulent spreading, in a propagation mode known as nonlinear self-channeling. Presented here is an experimental demonstration of such self-channeling through an artificially controlled turbulent atmosphere, with investigation into the region of parameter space over which it can occur. This research makes use of a distributed-

volume turbulence generator and long propagation ranges at the Naval Research Laboratory and the Air Force Research Laboratory in order to produce a controlled propagation environment suitable for the study of high-power beams.

Nonlinear self-channeling is found to resist the diffractive effects of turbulence, with its effectiveness decreasing significantly as the inner scale of turbulence decreases below the size of the beam.

NONLINEAR SELF-CHANNELING OF HIGH-POWER LASERS THROUGH TURBULENT ATMOSPHERES

by

Gregory P. DiComo

Dissertation submitted to the Faculty of the Graduate School of the
University of Maryland, College Park in partial fulfillment
of the requirements for the degree of
Doctor of Philosophy
2018

Advisory Committee:
Professor Thomas Antonsen, Chair/Advisor
Professor Christopher Davis
Professor Phillip Sprangle
Professor Antonio Ting
Professor Rajarshi Roy, Dean's Representative

At your disturbing power is this instrument come; whence will you go?

Four directions, then one. Alive must I be brought to Embelyon.

Jack Vance, *The Dying Earth*

Acknowledgments

I owe my gratitude to all the people who have made this thesis possible and because of whom my graduate experience has been one that I will cherish forever. It is impossible to remember all of the people who have contributed to this work. I apologize to anyone whom I have neglected to mention by name.

First I must thank my advisor, Professor Thomas Antonsen, for his keen insight, tremendous teaching skill, and great patience.

Thanks are due as well to Doctors Phillip Sprangle, Christopher Davis, Antonio Ting, and Rajarshi Roy, for agreeing to serve on my thesis committee.

I would also like to thank Doctors Richard Fischer and Antonio Ting, of the Naval Research Laboratory, for giving me the opportunity to work in the field of experimental physics. They had confidence in me when I had no confidence in myself. My career in physics, as opposed to any other field, is due to their faith in my abilities.

I would like to acknowledge the support of my other colleagues at the Naval Research Laboratory, especially Doctors Joseph Peñano and Michael Helle, who suggested the line of research which makes up this thesis. In addition, my current and past coworkers: Doctors Daniel Gordon, Theodore Jones, Dmitri Kaganovich, Yu-Hsin Chen, Melissa Hornstein, and John Palastro.

I want to thank Zachary Wilkes and Sanjay Varma, who showed me that the life of a graduate student, while hard, contained room for friendship and happiness. Paul Jaffe, Iyad Lababidi, Bipin Gyawali, Bisrat Addissie, Clayton Crocker, and all

of the many other graduate students with whom I spent so many sleepless nights solving problem sets. I would also like to thank Gregory Flynn, Richard Winters, Michael DiComo, Emily Bannister, Gramm and Sarah Richardson, Cassandra Wire, Brian Hildebrandt, and all the other good friends who have helped keep me sane.

I acknowledge the financial support of the Office of Naval Research, the High Energy Laser Joint Technology Office, and the Naval Research Laboratory Base Program, who provided the stable, ongoing project funding which made this research possible.

To my parents, Paul DiComo and Susan Putnam, I owe a lifelong love of science, engineering, and the arts.

I would like to acknowledge the motivating influence of my son, Alexander Joseph DiComo, against whose arrival I raced to finish this work.

Finally, and most importantly, I would like to acknowledge the unflagging love and support provided by my wife. Dawn, without you none of this would have been possible.

Table of Contents

List of Figures

List of Abbreviations

σ_x	The variance of any quantity x
$\bar{x}$	The average of any quantity x
$\vec{E}$	Electric field
$\vec{r}$	Arbitrary vector (x, y, z)
r	Radial coordinate
R_0	Beam radius at the transmitter
R	Beam radius at the receiver in the absence of turbulence
R_{LT}	Long-term beam radius at the receiver in the presence of turbulence
R_{ST}	Short-term beam radius at the receiver in the presence of turbulence
σ_c^2	Beam Wander
AFRL	Air Force Research Laboratory
CTA	Constant Temperature Anemometer
DEPS	Directed Energy Professional Society
GDFACT	Generator of Distributed Free Atmospheric Convective Turbulence
GVD	Group Velocity Dispersion
IREAP	Institute for Research in Electronics and Applied Physics
LED	Light-Emitting Diode
LISSD	Laser Inner Scale and Scintillation Diagnostic
NASA	National Aeronautics and Space Administration
NRL	Naval Research Laboratory
NSC	Nonlinear Self-Channeling
NSF	Nonlinear Self-Focusing
PDF	Probability Density Functions
RSI	Research Support Instruments
UMD	University of Maryland
USPL	Ultrashort Pulse Laser

Chapter 1: Introduction

1.1 Introduction

A variety of laser applications have been considered which depend on long-distance atmospheric propagation of the beam to attain practical utility. Such applications include point-to-point laser communications [1], laser power beaming [2], and directed energy [3]. In each case, the effectiveness of the application is limited to some extent by beam distortions caused by atmospheric turbulence. Extensive effort has been devoted to modeling and experimentally investigating this phenomenon for both low-power linear [4–8] and high-power nonlinear beams [9, 10].

Recently, a new paradigm for long-range propagation of high-power laser pulses has been predicted [11]. Nonlinear self-channeling (NSC) is a regime of propagation in which the laser power is comparable to the self-focusing power, and the radius of the beam is smaller than the transverse coherence radius of turbulence. Such a laser pulse is expected to remain highly collimated over many Rayleigh lengths, without experiencing either turbulence or diffraction-induced expansion. However, the NSC phenomenon has not yet been investigated experimentally. This work reports on experiments which establish the statistical behavior of nonlinear self-channeling beams.

In order to facilitate this work, an artificial turbulence generator suitable for use with high-power lasers has been built and characterized. This device allows controlled, accurate reproduction of the linear and nonlinear properties of naturally-occurring turbulence. The turbulence generated by this generator has been shown to be similar to that observed in an outdoor environment.

Using this generator as a source of turbulence, experiments have been conducted which demonstrate and characterize the statistics of NSC beams propagating through atmospheric turbulence. This work establishes that NSC is robust against increase in turbulence strength into the strong turbulence regime. It exhibits graceful degradation, with the probability of generating a small spot after propagation decreasing smoothly with increasing turbulence. Even under strong turbulence, an NSC beam is likely to produce a smaller, more intense spot at the end of propagation than a linearly propagating beam.

1.2 Organization

This work begins with an brief introduction to the theory of atmospheric turbulence in Chapter 2. For a fuller treatment of this deep and complex subject, see, for example, the books by Tatarskii or Andrews & Phillips [7, 12]. Thereafter, Chapter 3 introduces the theory of linear laser propagation through a turbulent atmosphere, insofar as it is necessary to present the equations used later in the thesis to compare theory to experiment. Chapter 4 then outlines the theory and practice of generating artificial turbulence in the laboratory, and describes the design and

characterization of the turbulence generator used throughout this work. Chapter 5 then gives a brief overview of recent work concerning nonlinear laser propagation through turbulence.

With the groundwork thus laid, Chapter 6 presents experiments performed over a moderate range at the U.S. Naval Research Laboratory (NRL), which provided the first experimental demonstration of NSC. Chapter 7 presents a detailed analysis of experiments performed over a long range at the U.S. Air Force Research Laboratory (AFRL), comparing the propagation statistics of high-power NSC beams to those of low-power beams. These experiments establish the robust resistance of NSC beams to atmospheric turbulence into the strong-turbulence regime. Finally, Chapter 8 contains concluding remarks and plans for future research in this area.

Chapter 2: Atmospheric Turbulence

2.1 Overview

Atmospheric turbulence is the fluctuation of the fluid-dynamical properties of air, over a range of scale lengths, in response to large-scale flow. An artistic rendering of turbulent motion at a variety of scale lengths is presented in Figure 2.1. Credit for this clever example of turbulent flow is due to Ball [13].

Following the foundational work of Kolmogorov, turbulent fluctuations in air properties are typically modeled as randomly-fluctuating fields, without reference to the deterministic flows which drive those fluctuations. In spite of this simplification, many statistical properties of turbulence have been calculated, with good agreement with experiment. This analysis has led to ways of experimentally characterizing the statistical properties of turbulence without being forced to measure the entire flow field.

Figure 2.1: *The Great Wave off Kanagawa*, woodcut by Hokusai. Multiple scale lengths of turbulence are visible in this image, from the outer scale at the size of the largest wave, through the inner scale at the size of the smallest eddies.

2.2 Atmospheric Turbulence

2.2.1 The Approach of Kolmogorov

Although velocity turbulence has been known as a phenomenon of fluid motion for generations, the foundational statistical treatment of such turbulence is generally held to be that of Kolmogorov [4]. Kolmogorov developed a power spectrum for homogenous, isotropic turbulence for a range of scales between the large deterministic flows (the "outer scale," denoted L_0) and the small vortices whose kinetic energy is dissipated by viscosity (the "inner scale," denoted l_0). Between these scales lies the "inertial subrange."

Kolmogorov made two major hypotheses: the first, presented as an extended footnote, was that turbulent motion in the inertial subrange consists of a succession of increasingly tiny self-similar vortices, in which energy is passed from large scale sizes to small, with the energy dissipation rate per unit mass constant over all scales. The second, originally formulated as two separate statements, was that the motion within the inertial subrange is independent of both the nature of the driving flow at the outer scale, as well as the viscous dissipation occurring at the inner scale. Under these circumstances, Kolmogorov developed an expression describing the statistical properties of turbulent velocity fluctuations.

2.2.2 Correlation and Structure of Turbulence

Kolmogorov treats turbulence quantities as random variables. Here, and throughout this work, "turbulence quantities" refers to any physical quantity which fluctuates as a function of position and time within the turbulent fluid; most often the velocity, temperature, or index of refraction. As random variables, turbulence quantities can be characterized by their statistical moments, such as mean, correlation, *et cetera*.

Consider a randomly varying scalar field $x(\vec{r}, t)$. The correlation function of random field x is defined as:

$$B_x(\vec{r}_1, \vec{r}_2, t) = \langle [x(\vec{r}_1, t) - \bar{x}(\vec{r}_1, t)][x^*(\vec{r}_2, t) - \bar{x}^*(\vec{r}_2, t)] \rangle \tag{2.1}$$

where angle brackets indicate expectation, an asterisk indicates the complex conjugate, $\bar{x}(\vec{r}_1, t)$ is the expected value of x at position $\vec{r}_1$ and time t, and all expectations are performed over probability space; that is, averaging over all possible realizations of the random field. For a statistically stationary, homogenous, and isotropic field, $\bar{x}$ is independent of space and time, and the correlation function reduces to

$$B_x(R) = \langle x(\vec{r}_1) x^*(\vec{r}_2) \rangle - \bar{x}^2 \tag{2.2}$$

where R is the separation $|\vec{r}_2 - \vec{r}_1|$ for any choice of $\vec{r}_{1,2}$. $B_x(R)$ is now a function only of the separation between the measurement points. When considering turbulent quantities, the assumption of ergodicity is often made in addition to that of stationarity; that is, that expectations over time can be substituted for expectations

over realizations. This assumption is necessary for experimental results, which are necessarily performed over time within a single realization of the universe, to be compared to theoretical results, which are free to consider multiple realizations.

The assumptions of homogeneity and isotropy drive Kolmogorov's argument; it is particularly important that the mean value of each turbulent quantity be constant over all space. This is not frequently the case; however, the *difference* between turbulent field quantities at two locations almost always behaves like a statistically homogenous random field [4, 7]. Therefore, we introduce the structure function in lieu of the correlation [14].

The structure function for a time-varying random field $x(\vec{r}, t)$ is defined as:

$$D_x(\vec{r}_1, \vec{r}_2, t) = \left\langle |x(\vec{r}_1, t) - x(\vec{r}_2, t)|^2 \right\rangle \tag{2.3}$$

If the random field is stationary, *locally* homogenous (that is, it consists of a zero-mean statistically homogenous fluctuation plus a locally-varying mean, $x(\vec{r}) = x_1(\vec{r}) + \bar{x}(\vec{r})$ with $\bar{x_1} = 0$ statistically homogenous), and isotropic, then the structure function depends only on the separation R between the two points, and not on which particular points you pick. It can then be written as

$$D_x(R) = \left\langle |x(\vec{r}_1) - x(\vec{r}_1 + \vec{R})|^2 \right\rangle \tag{2.4}$$

for any choice of $\vec{r}_1$ and $\vec{R}$.

If the field is indeed statistically homogenous, not merely locally homogenous, then we have lost nothing by choosing to use the structure function; it is related to

the correlation function by

$$D_x(R) = 2[B_x(0) - B_x(R)] \tag{2.5}$$

In the first of his 1941 papers, Kolmogorov performed a coordinate transform to a reference frame which includes subtraction of velocities at one point from those at another; in effect, every correlation function in [4] is in fact a structure function.

Another method often used to characterize turbulence quantities is the power spectrum of turbulence. This can be calculated from the Fourier transform of the structure function [15]. The one-dimensional power spectrum is given by [7, 16]

$$\Phi_x(\kappa) = \frac{1}{4\pi^2\kappa^2} \int_0^\infty \frac{\sin \kappa R}{\kappa R} \frac{\mathrm{d}}{\mathrm{d}R} \left[R^2 \frac{\mathrm{d}}{\mathrm{d}R} D_x(R) \right] dR \tag{2.6}$$

where κ is the spatial wavenumber associated with scale size l, $\kappa = 2\pi/l$ in units of radians per meter.

2.2.3 Velocity and Temperature Turbulence

Discussion now returns to Kolmogorov's approach to turbulence. Kolmogorov showed that within the inertial subrange, when the hypotheses of self-similarity and scale independence hold, the structure function for the component of fluid velocity along a path between two measurement points must be given by [4, 7, 17]

$$D_V(R) = C_V^2 R^{2/3} \tag{2.7}$$

where C_V^2 is the velocity structure parameter in units of $m^{4/3}/s^2$ and R is the

separation between the measurement points. Velocity turbulence of this form is modeled as a stationary, locally homogenous, and isotropic random field.

C_V^2 is related to the energy dissipation rate by $C_V^2 = m\epsilon^{2/3}$, where m is a dimensionless constant experimentally determined to be approximately 2, and ϵ is the rate of energy dissipation per unit mass, in units of m^2/s^3. $D_V(R)$ has units of $m^{4/3}/s^2$. Equation 2.7 describes mathematically the "Kolmogorov cascade" in which energy enters the system at the largest spatial scale and "cascades" to ever smaller scales, where it is eventually dissipated by viscosity. However, it does not describe the driving or dissipative mechanisms.

2.2.4 Optical Turbulence

Optical turbulence in the atmosphere is generated when turbulent velocity fluctuations act to mix parcels of air of different temperatures together. The resulting turbulent fluctuations in air temperature lead to turbulent fluctuations in density, and thus to fluctuations in the index of refraction. With this in mind, the method of Kolmogorov was extended to index fluctuations. An outer scale, inner scale, and inertial subrange are defined for index fluctuations, analogous to the corresponding quantities for velocity. For optical atmospheric turbulence (henceforth simply *turbulence*), the structure function in the inertial subrange is given by

$$D_n(R) = C_n^2 R^{2/3} \tag{2.8}$$

where C_n^2 is the index of refraction structure parameter in $m^{-2/3}$. Near the ground,

C_n^2 typically ranges from as little as 10^{-16} for very weak turbulence, through 10^{-12} for very strong turbulence.

Based on this form for the structure function, the spatial power spectrum of turbulence can be shown to be [7]

$$\Phi_n(\kappa) = 0.033 C_n^2 \kappa^{-11/3} \tag{2.9}$$

where κ is the spatial wavenumber in rad/m. This is the *Kolmogorov spectrum* for turbulence. It neglects inner and outer scale effects, and is therefore only valid within the inertial subrange, $l_0 \ll 1/\kappa \ll L_0$. However, it is still used for many cases in which the scale of interest is far from the inner and outer scales.

When inner and outer scale effects cannot be neglected, modifications to the Kolmogorov spectrum must be made in order to truncate the cascade at high and low wavenumbers [12, 18, 19]. Without truncation at high wavenumber, the energy dissipation into viscosity is not described; without truncation at low wavenumber, the spectrum contains infinite energy. The *modified von Kármán spectrum* is a commonly used spectrum which includes both of these effects in a simple manner; it is given by [7]

$$\Phi_n(\kappa) = 0.033 C_n^2 (\kappa^2 + \kappa_0^2)^{-11/6} \exp(-\kappa^2/\kappa_m^2) \tag{2.10}$$

$$\Phi_n(\kappa) = 0.033 C_n^2 (\kappa^2 + \kappa_0^2)^{-11/6} \exp(-\kappa^2 R(z)^2) \tag{2.11}$$

where $\kappa_0 = 2\pi/L_0$ and $\kappa_m = 5.92/l_0$ define the outer and inner scale cutoff wavenum-

bers, respectively.

The outer and inner scale sizes are determined by the geometry of the turbulence. For turbulence in the open atmosphere, in the 100 meters nearest the ground, the outer scale is equal to approximately 1/2 the distance above the ground [7, 12]. The inner scale of turbulence is related to the energy dissipation rate by [12]

$$l_0 = a\nu^{3/4}\epsilon^{-1/4} \tag{2.12}$$

where ν is the fluid viscosity, ϵ is the energy dissipation rate, and a is a medium-dependent dimensionless constant, equal to 7.4 for air [19].

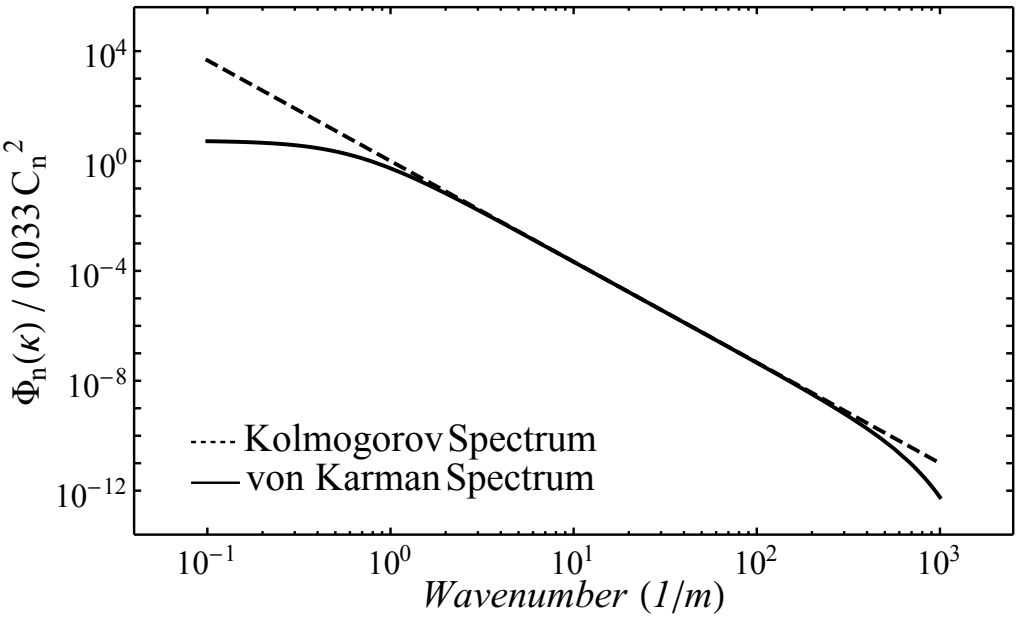

Figure 2.2: The Kolmogorov and Von Karman turbulence spectra. The Von Karman spectrum includes inner and outer scale effects.

In conditions when the average wind speed is greater than the typical eddy flow speed, the turbulence can be conceived of as a more-or-less static random

field of index variations, which is swept through a volume of interest (such as a laser propagation path) by a transverse wind [20]. This is the Taylor frozen-flow hypothesis. The required conditions often hold; typical time scales for transverse wind motion are on the order of 1 second, while the time scale for eddy movement is on the order of 10 seconds [7]. This hypothesis implies that spatial and temporal statistics of turbulence should be the same.

2.3 Turbulence Characterization

Multiple methods of experimentally characterizing atmospheric turbulence exist. Methods used in this work include hot wire anemometry, commercial scintillometer, and a combination measurement of beam intensity fluctuation and angle-of-arrival variation. Each of these methods is described below.

2.3.1 Hot Wire Anemometry

Velocity turbulence can be characterized by measuring fluctuations in the local air velocity within the turbulent volume. A hot wire anemometer is an instrument capable of measuring the wind velocity past a small probe at high speed and with great accuracy.

Hot wire anemometers operate on the principle that the resistance of a conductor is a function of its temperature. A small probe wire ($\sim 5\ \mu$ m diameter and 1 mm long) is heated to a high temperature (~ 150 deg C); since the wire has very low heat capacity, air flow past the probe rapidly cools the wire by forced convection.

Ohmic heating and convective cooling dominate the heat transfer equation; thus the wire temperature can be related to the flow velocity [15].

In a *constant current anemometer*, the current through the wire is kept constant and the resistance is measured to determine the temperature, and thereby the air flow velocity. In a *constant temperature anemometer* (CTA) the resistance of the wire (and thus its temperature) is kept constant by a feedback circuit; the voltage applied to accomplish this is then measured to determine the velocity. In either case, careful calibration is necessary in order to determine the relationship between the air velocity and measured electrical quantity. Commercial anemometers are typically calibrated at the factory. Since the thermal mass of the wire is small, fluctuations in velocity can be measured at frequencies on the order of one to ten kilohertz [15]. In this work, a CTA has been used to characterize turbulent velocity fluctuations.

2.3.1.1 Effect of Temperature Fluctuations

For a CTA, the voltage across the wire will be proportional to the rate of heat loss due to convection. The following analysis demonstrates that fluctuations in the rate of heat loss are dominated by fluctuations in the velocity of the fluid, and not significantly influenced by fluctuations in the temperature. That is, a CTA is a constant-temperature *anemometer*, and not a constant-temperature *thermometer*. Smolyakov has written that air temperature does not affect the measurements of velocity fluctuations relative to the mean; a calculation to support this assertion is

found below [15].

In the limit of forced convection, the rate of heat loss for a hot cylinder immersed in a fluid flow is given by

$$\dot{Q} = hA(T_c - T_f) \tag{2.13}$$

where A is the surface area of the cylinder, given by πDL, D and L are the diameter and length of the cylinder, T_c and T_f are the temperatures of the cylinder and the fluid respectively, and h is the geometry-dependent heat transfer coefficient. For a cylinder experiencing forced convection, the heat transfer coefficient is given by [21]

$$h = \frac{\mathrm{k}}{D}(0.24 + 0.56\mathrm{Re}_D^{0.45})(\frac{T_c}{T_f})^{-0.17} \tag{2.14}$$

where k is the thermal conductivity of the fluid, Re is the Reynolds number for the flow due to the influence of the cylinder, and the constants have been determined experimentally. The Reynolds number is a nondimensional number which quantifies the ratio of inertial to viscous forces in the fluid flow. The Reynolds number for flow at velocity v around an object of characteristic dimension x is given by

$$\mathrm{Re}_x = \frac{\rho v x}{\mu} \tag{2.15}$$

where ρ is the fluid mass density and μ is the fluid's dynamic viscosity.

The constants in equation 2.14 have been determined under the conditions that Reynolds number Re < 77. For the case of a CTA measuring atmospheric turbulence, the characteristic dimension is the wire's diameter (on the order of

microns) and the characteristic velocity is on the order of 1 m/s. The resulting Reynolds number is thus less than one.

Returning to the analysis of $\dot{Q}$ fluctuations, typical temperature fluctuations are on the order of 0.1 C, and the velocity fluctuates on the order of 0.05 m/s. In this case the temperature contribution to the heat transfer fluctuations (and thus the measured voltage) is approximately 5% of the total fluctuation.

2.3.1.2 Benchmark

In this work, a commercial CTA manufactured by TSI was used to characterize velocity turbulence. The CTA was benchmarked by measuring the turbulent velocity fluctuations one meter above a concrete parking lot. The velocity structure function was generated by using the Taylor frozen-flow hypothesis to convert time-resolved data into space-resolved data. The average wind speed past the probe during the measurement was 0.26 m/s. The one-dimensional power spectrum of the structure function demonstrates a slope of approximately $-5/3$, as expected for Kolmogorov turbulence. These results are summarized in Figure 2.3.

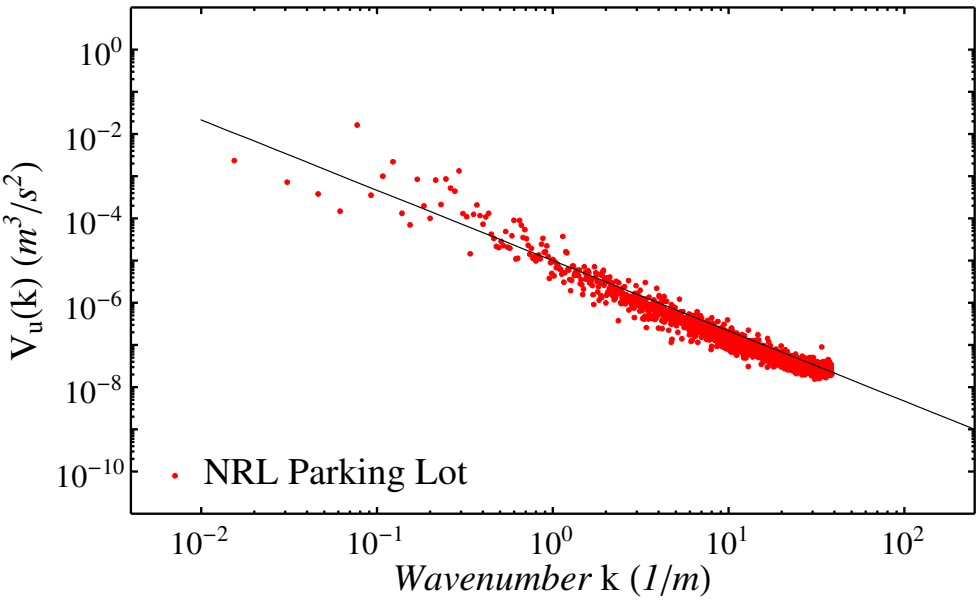

Figure 2.3: One-dimensional velocity turbulence power spectrum $V_u(k)$ for a naturally turbulent atmosphere. A $-5/3$-slope line is displayed in black.

2.3.2 Scintillometer

Optical turbulence can be characterized by passing light through a volume of uniform turbulence and observing the resulting changes in the light. Under certain assumptions, measured statistical properties of the light can be related to statistical properties of the turbulence.

A scintillometer is a diagnostic designed to measure optical turbulence by projecting a broad beam of incoherent light through the turbulent volume to a remote receiver with a large aperture. The large aperture acts to increase the effective range at which the device can determine C_n^2 [22]. The fluctuating intensity of the received light, or *scintillation*, is recorded in order to back out C_n^2 according to theoretical equations. For such a device, the structure parameter is given by

$$C_n^2 = 1.12\sigma_{lnI}^2 D^{7/3} L^{-3} \tag{2.16}$$

where σ_{lnI}^2 is the normalized variance of the log of the intensity fluctuations, and D is the diameter of the transmitter and receiver apertures [23]. Scintillometer theory and practice are well-developed, and the technique has been benchmarked against independent measurements of turbulence [22]. Scintillometers are widely available as an industry-standard method of measuring C_n^2. A Kipp & Zonen LAS MkII scintillometer was used throughout this work as an industrial standard to characterize C_n^2 and benchmark other diagnostics. However, the increased aperture size of the scintillometer also increases the minimum scintillation necessary to produce a response. The scintillometer is therefore inappropriate for short-range or very

low-turbulence environments.

2.3.3 LISSD

Another optical diagnostic for measuring turbulence parameters is the Laser Inner Scale and Scintillation Diagnostic (LISSD). The LISSD is capable of measuring the structure parameter C_n^2, as well as the inner scale of turbulence l_0. This diagnostic was first developed and implemented by Consortini *et al.* in 2003 [24].

The LISSD uses a low-power helium-neon laser ($\lambda = 632.8$ nm) which propagates through the turbulence. The laser must have a Rayleigh range much shorter than the propagation distance, or a pinhole must be placed in front of the laser, in order to ensure that the wavefront at the detector is a spherical wave. The detector is a digital video camera positioned a fixed distance behind a pinhole. Scintillation and beam wander cause the spot formed on the camera sensor to fluctuate in both intensity and position. The intensity fluctuations are used to determine the scintillation index σ_I^2, the variance of the intensity normalized to the square of the mean [7]. The position wander, coupled with the distance between the detector and the pinhole, gives the angle-of-arrival fluctuation $\langle \alpha^2 \rangle$. These two measurements give the path-averaged C_n^2 and l_0 according to

$$C_n^2 = \frac{0.5 k^{7/6} L^{11/6}}{\sigma_I^2} \tag{2.17}$$

and

$$l_0 = 1.08L \left(\frac{\langle \alpha^2 \rangle}{\sigma_I^2} \right)^{1/2} \tag{2.18}$$

The implementation of the LISSD used in this work has been benchmarked against the Kipp & Zonen commercial scintillometer over a distance of 100 meters in a typical outdoor environment at NRL. Under these conditions the C_n^2 values reported by the LISSD matched those reported by the commercial instrument. The scintillometer's operating wavelength of 850 nm is taken into account by its internal software when calculating C_n^2, so the wavelength difference between the LISSD and the scintillometer does not affect the measurement. Because of its superior ability to make measurements over short distances or under low turbulence conditions, as well as its ability to measure l_0, the LISSD is the primary turbulence diagnostic used in this work.

Chapter 3: Linear Laser Beam Propagation

3.1 Overview

When a laser beam propagates through a turbulent medium, it acquires random phase perturbations caused by the spatially-varying refractive index of the medium. As turbulent flows move, these phase perturbations fluctuate randomly. The index of refraction fluctuations can be thought of as as weak, distributed lenses throughout the turbulent volume. Those fluctuations much larger than the beam tend to steer it as a whole; those much smaller act as scattering centers; those in the intermediate range act to alter the intensity profile of the beam. Fluctuations of all sizes act on the beam simultaneously. The resulting fluctuations of the beam profile, size, and position have been extensively studied, and theoretical expressions exist to describe their statistics.

The treatment of laser beam propagation in turbulence in this chapter is due to Andrews and Phillips; for a more detailed look at the subtleties of this topic see their 2005 book on the subject [7]. The presentation here is limited to only those equations necessary to reproduce the figures in Chapters 6 and 7.

3.2 Without Turbulence

3.2.1 The Wave Equation

The propagation of light in the absence of medium-dependent effects is governed by the wave equation

$$\nabla^2 \vec{E} - \frac{1}{c^2}\frac{\partial^2 \vec{E}}{\partial t^2} = 0 \tag{3.1}$$

where ∇^2 is the Laplacian operator, $\vec{E}(x, y, z, t)$ is the complex electric field, and c is the speed of light. Under the assumption of a linearly polarized monochromatic wave (that is, $\vec{E}(x, y, z, t) = \hat{x}E_0(x, y, z)e^{-i\omega t}$), and orienting the coordinate system so that the z-axis points in the direction of propagation, the equation becomes

$$\nabla_\perp^2 E_0 + \frac{\partial^2 E_0}{\partial z^2} + k^2 E_0 = 0 \tag{3.2}$$

where k is the optical wavenumber of the laser field, given by $k = \omega/c = 2\pi/\lambda$.

Assuming radial symmetry ($E_0(x, y, z) = E_0(r, z)$) and taking the paraxial approximation $\left(\nabla_\perp^2 E_0 \gg \frac{\partial^2 E_0}{\partial z^2}\right)$, the wave equation becomes

$$\nabla_r^2 E_0 + k^2 E_0 = 0 \tag{3.3}$$

3.2.2 Gaussian Beam Propagation

The lowest order transverse mode of a laser resonator is a Gaussian beam [25]. Therefore, we look for solutions to Equation 3.3 of the form [7].

$$E_0(r,z) = A(z)\exp\left[-\frac{1}{p(z)}\left(\frac{\alpha_0 k r^2}{2}\right)\right] \tag{3.4}$$

where $\alpha_0 = \frac{2}{kR_0^2} + i\frac{1}{F_0}$, R_0 is the initial radius of the beam, and F_0 is the radius of curvature of the phase front. $A(z)$ is the propagation distance-dependent peak field, and $p(z)$ contains the phase. The exact form of Equation 3.4 has been chosen to simplify later analysis, and maintain consistency with [7]. By solving the wave equation with appropriate boundary conditions, the remaining parameters in Equation 3.4 can be shown to be

$$\begin{aligned} p(z) = 1 + i\alpha_0 z = 1 - \frac{z}{F_0} + i\frac{2z}{kR_0^2} \\ A(z) = \frac{1}{p(z)} \end{aligned} \tag{3.5}$$

These parameters in turn lend themselves to expression in terms of the following parameters [7].

$$\begin{aligned} \Theta_0 = 1 - \frac{z}{F_0} \\ \Lambda_0 = \frac{2z}{kR_0^2}, \end{aligned} \tag{3.6}$$

known as *input beam parameters* since they characterize the beam at the beginning of its propagation. The focusing parameter, Θ_0, characterizes the initial divergence of the beam: it is equal to 1 for collimated beams, less than 1 for converging beams,

and greater than 1 for diverging beams. The Fresnel ratio, Λ_0, characterizes the distance from the beam relative to its initial size.

The input beam parameters can in turn be used to define the *output beam parameters*

$$\begin{aligned} \Theta &= \frac{\Theta_0}{\Theta_0^2 + \Lambda_0^2} = 1 + \frac{z}{F} \\ \Lambda &= \frac{\Lambda_0}{\Theta_0^2 + \Lambda_0^2} = \frac{2z}{kR^2}, \end{aligned} \tag{3.7}$$

which characterize the beam after a distance of propagation z. Here R and F are the beam's radius and phase front radius of curvature after propagation. The beam size changes as a function of distance, according to

$$R(z)^2 = R_0^2 \left(\Theta_0^2 + \Lambda_0^2\right) = \frac{R_0^2}{\Theta^2 + \Lambda^2} \tag{3.8}$$

For the case of a collimated beam ($\Theta_0 = 1$), the beam propagates as

$$R(z)^2 = R_0^2 \left(1 + \left(\frac{z}{z_R}\right)^2\right) \tag{3.9}$$

where $z_R = \pi R_0^2/\lambda$ is the Rayleigh range, the distance over which the radius of the beam increases by a factor of $\sqrt{2}$.

As the beam propagates, conservation of energy requires that the peak intensity change as the radius does, decreasing as R increases. The resulting intensity profile can be shown to be

$$I(r) = \left(\frac{1}{\Theta_0^2 + \Lambda_0^2}\right) \exp\left(-\frac{2r^2}{R^2}\right) = \left(\Theta^2 + \Lambda^2\right) \exp\left(-\frac{2r^2}{R^2}\right) \tag{3.10}$$

with on-axis intensity

$$I(0) = \frac{R_0^2}{R^2} = \frac{1}{\Theta_0^2 + \Lambda_0^2} = \Theta^2 + \Lambda^2 \tag{3.11}$$

3.3 With Turbulence

When a laser beam propagates through turbulence, the intensity profile received at the target is observed to vary in time. As the beam propagates, it acquires random phase perturbations due to turbulence. The beam wanders, its profile varies, and its intensity fluctuates. An illustrative example of the effect turbulence can have on a beam profile is displayed in Figure 3.1.

3.3.1 Weak Turbulence

As a laser beam propagates through a medium with spatially varying index, different transverse locations in the beam will acquire random phase errors and decohere from one another. The transverse coherence length of such a beam, the distance in the transverse dimension over which it remains coherent, will naturally decrease with distance. The weak turbulence limit applies when this change in transverse coherence length can be neglected [26]. Under these conditions the electric field of the wave can be expressed as $E(x, y, z) = E_0 \exp[\psi(x, y, z)]$, where E_0 is the electric field without turbulence and ψ contains all complex phase perturbations due to turbulence. This analysis is known as the Rytov method [12].

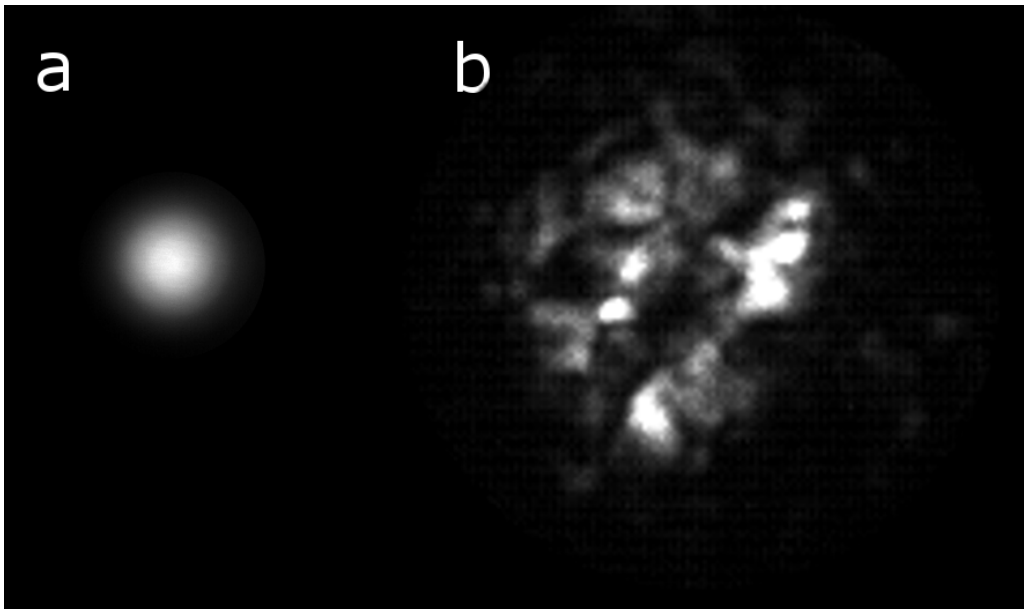

Figure 3.1: Laser beam images taken before (a) and after (b) propagation through more than 1 km of natural turbulence at Starfire Optical Range. Note the increase in the spot size, as well as the significant distortion of the intensity profile. The instantaneous $1/e^2$ beam radius is 2.1 cm before propagation, and 7.8 cm after. The propagation range is 3.2 km; $C_n^2 = 1.4{\times}10^{-14}\mathrm{m}^{-2/3}$; the Rytov parameter $\sigma_{\mathrm{R}}^2 = 3.6$. This is considered to be "strong" turbulence.

3.3.1.1 Rytov Variance and Scintillation Index

The fluctuation of the intensity of a laser beam is known as scintillation. Its strength is characterized by the scintillation index, equal to the variance of the on-axis intensity normalized to the square of the mean. For an infinite plane wave of wavenumber k, propagating a distance L through Kolmogorov turbulence, and keeping perturbations on the phase to second order, the scintillation index is predicted to be

$$\sigma_R^2 = 1.23 C_n^2 k^{7/6} L^{11/6} \tag{3.12}$$

also known as the Rytov variance, or Rytov parameter. The Rytov parameter is often used to characterize the strength of turbulence. For $\sigma_R^2 \ll 1$, the turbulence is said to be weak; for $\sigma_R^2 \gg 1$, the turbulence is said to be strong. For weak turbulence, the scintillation index of the plane wave is equal to the Rytov parameter. As turbulence becomes strong, the scintillation index increases more slowly than the Rytov parameter. The Rytov parameter continues to be used to characterize the strength of turbulence, even beyond the point where it represents the scintillation index of any real beam.

For a Gaussian beam propagating in weak turbulence with a von Karman spectrum, the scintillation index is given by

$$\sigma_I^2 = 3.93\sigma_R^2\Lambda^{5/6}\left[\left(\frac{\Lambda Q_m}{1+0.52\Lambda Q_m}\right)^{1/6} - 1.29(\Lambda Q_0)^{1/6}\right]\frac{r^2}{R^2}$$
$$+ 3.86\sigma_R^2\left\{0.40\frac{[(1+2\Theta)^2+(2\Lambda+3/Q_m)^2]^{11/12}}{[(1+2\Theta)^2+4\Lambda^2]^{1/2}}\sin\left(\varphi_0+\frac{11}{6}\varphi_m\right)\right.$$
$$\left. - \frac{6\Lambda}{Q_m^{11/6}[(1+2\Theta)^2+4\Lambda^2]} - \frac{11}{6}\left(\frac{1+0.31\Lambda Q_m}{Q_m}\right)^{5/6}\right\} \quad (3.13)$$

where $\varphi_0 = \tan^{-1}\left[\frac{2\Lambda}{1+2\Theta}\right]$, $\varphi_m = \tan^{-1}\left[\frac{(1+2\Theta)Q_m}{3+2\Lambda Q_m}\right]$, $Q_m = L\kappa_m^2/k$ represents the effect of the inner scale, $Q_0 = L\kappa_0^2/k$ represents the effect of the inner scale, and recalling that the dependence on propagation distance L is contained in parameters Λ and Θ.

3.3.1.2 Beam Wander

Beam wander is defined as the variance of the distance of the beam centroid from the long-term averaged centroid location. It is due to perturbations to the phase with scale size larger than the radius of the beam. An expression for the wander can be derived by multiplying the turbulence spectrum Φ by a longpass filter function which causes Φ to fall off exponentially at κ larger than $1/R(z)$. The result of this procedure is

$$\sigma_c^2 = 7.25C_n^2L^3R_0^{11/3}\int_0^1 \xi^2\left\{\frac{1}{|\Theta_0+\bar{\Theta}_0\xi|^{1/3}} - \left[\frac{\kappa_0^2R_0^2}{1+\kappa_0^2R_0^2(\Theta_0+\bar{\Theta}_0\xi)^2}\right]^{1/6}\right\}d\xi \quad (3.14)$$

where $\bar{\Theta}_0 = 1-\Theta_0$. The absence of an inner scale term is due to the filter function. In the absence of outer scale effects (that is, using a Kolmogorov spectrum), the

beam wander of a collimated Gaussian beam reduces to

$$\sigma_c^2 = 2.42 C_n^2 L^3 R_0^{-1/3} \tag{3.15}$$

3.3.1.3 Long-Term Beam Size

Although the instantaneous intensity profile of an initially Gaussian beam is more or less distorted after propagation through turbulence, the long-term average intensity profile nevertheless remains approximately Gaussian [7]. This long-term average profile has a characteristic spot size, which is increased relative to the vacuum case by turbulence. For a Gaussian beam propagating through weak turbulence, and assuming a von Karman turbulence spectrum (equation 2.10), it can be written

$$R_{LT}^2 = R^2 \left(1 + 3.54 \sigma_R^2 \Lambda^{5/6} \left(\frac{(1 + 0.31 \Lambda Q_m)^{5/6} - 1}{(\Lambda Q_m)^{5/6}} - 0.36 (\Lambda Q_0)^{1/6} \right) \right) \tag{3.16}$$

where R is the radius of the beam in the absence of turbulence.

In the absence of inner and outer scale effects, and assuming a collimated beam, the Kolmogorov spectrum takes the place of the von Karman spectrum and this expression simplifies to

$$R_{LT}^2 = R^2 \left(1 + \frac{z^2}{z_R^2}\right) \left(1 + 1.33 \sigma_R^2 \left(\frac{z\, z_R}{z^2 + z_R^2} \right)^{5/6} \right) \tag{3.17}$$

The long-term spot size includes independent contributions from both instantaneous spreading and breakup of the beam (detailed in the next section), as well

as the random wander of the beam centroid over time [27]. The contributions sum in quadrature, as

$$R_{LT}^2 = R_{ST}^2 + \sigma_c^2 \tag{3.18}$$

where R_{ST} is the instantaneous beam radius due to spreading and breakup, and σ_c^2 is the variance of the beam centroid.

3.3.1.4 Short-Term Beam Size

Combining equations 3.17, 3.18, and 3.15 gives an expression for the expected instantaneous spot size,

$$R_{ST}^2 = R_0^2 \left(1 + \frac{z^2}{z_R^2}\right) \left(1 + 1.33\sigma_R^2 \left(\frac{z\, z_R}{z^2 + z_R^2}\right)^{5/6} - \left(2.42 C_n^2 L^3 R_0^{-1/3}\right)\right) \tag{3.19}$$

The instantaneous spot size is expected to match this formula on average, not for each individual realization of turbulence. An analogous expression for the more general case of a non-collimated Gaussian beam in von Karman turbulence can be calculated by subtracting Equations 3.16 and 3.14 in accordance with Equation 3.18. However, it has no algebraic closed form and will not be presented here. This expression will be evaluated numerically in Chapters 6 and 7 to compare theory to experiment.

3.3.2 Strong Turbulence

As a beam propagates through turbulence, its transverse coherence length is decreased as turbulence introduces random phase errors into the beam. In weak turbulence theory, we neglect this turbulence-induced decrease in coherence length, and treat the coherence length as always infinite. This is a reasonable approximation because weak turbulence is not capable of altering the coherence length much. However, in strong turbulence, the beam's coherence length decreases significantly with propagation distance. This decreases the effect of turbulence relative to what would be expected from weak turbulence theory. Turbulent fluctuations larger than the coherence length of the beam no longer have any power to spoil the wavefront of the beam, as the wavefront is already fully randomized at those length scales. In order to account for this effect, strong turbulence theory introduces filter functions, which act to kill the contribution of turbulence at scales larger than the coherence length.

Equations comparable to those for weak turbulence exist for the case of strong turbulence. Some involve integrals which do not easily simplify to algebraic expressions; those integrals are presented unevaluated here. For the portions of this work which took place under conditions of strong turbulence, the appropriate equations were evaluated numerically in order to compare theory to experiment.

3.3.2.1 Coherence Length

Assuming the beam is much smaller than the outer scale of turbulence, as is the case for this work, the coherence length of a Gaussian beam propagating through strong turbulence with a Von Karman spectrum is given by

$$\rho_0 = \begin{cases} \left(\frac{3}{1+\Theta_e+\Theta_e^2+\Lambda_e^2}\right)^{1/2} \left(1.64 C_n^2 k^2 L l_0^{-1/3}\right)^{-1/2} & \rho_0 \ll l_0 \\ \left[\frac{8}{3(a_e+0.62\Lambda_e^{11/6})}\right]^{3/5} (1.46 C_n^2 k^2 L)^{3/5} & l_0 \ll \rho_0 \ll L_0 \end{cases} \tag{3.20}$$

where the effective strong-turbulence receiver beam parameters are given by

$$\begin{aligned} \Theta_e &= \frac{\Theta - 0.81(\sigma_R^2)^{6/5}\Lambda}{1 + 1.63(\sigma_R^2)^{6/5}\Lambda} \\ \Lambda_e &= \frac{\Lambda}{1 + 1.63(\sigma_R^2)^{6/5}\Lambda} \end{aligned} \tag{3.21}$$

and the parameter a_e is given by

$$a_e = \begin{cases} \frac{1-\Theta^{8/3}}{1-\Theta} & \Theta \geq 0 \\ \frac{1+|\Theta|^{8/3}}{1-\Theta} & \Theta < 0 \end{cases} \tag{3.22}$$

3.3.2.2 Scintillation Index

For a Gaussian beam propagating in strong turbulence with a Modified Atmospheric spectrum, the scintillation index is given by

$$\sigma_I^2 = \exp\left[\sigma_{\ln X}^2(l_0) - \sigma_{\ln X}^2(L_0) + \frac{0.51\sigma_G^2}{\left(1 + 0.69\sigma_G^{12/5}\right)^{5/6}}\right] - 1 \tag{3.23}$$

where the Gaussian-beam Rytov variance with nonzero inner scale is given by

$$\begin{aligned}\sigma_G^2 = 3.86\sigma_R^2\Bigg\{ & 0.40\frac{[(1+2\Theta)^2+(2\Lambda+3/Q_l)^2]^{11/12}}{[(1+2\Theta)^2+4\Lambda^2]^{1/2}}\Bigg[\sin\left(\varphi_0+\frac{11}{6}\varphi_l\right) \\ & + \frac{2.61}{[(1+2\Theta)^2Q_l^2+(3+2\Lambda Q_l)^2]^{1/4}}\sin\left(\varphi_0+\frac{4}{3}\varphi_l\right) \\ & - \frac{0.52}{[(1+2\Theta)^2Q_l^2+(3+2\Lambda Q_l)^2]^{7/24}}\sin\left(\varphi_0+\frac{5}{4}\varphi_l\right)\Bigg] \\ & - \frac{13.40\Lambda}{Q_l^{11/6}[(1+2\Theta)^2+4\Lambda^2]} - \frac{11}{6}\Bigg[\left(\frac{1+0.31\Lambda Q_l}{Q_l}\right)^{5/6} \\ & + \frac{1.10(1+0.27\Lambda Q_l)^{1/3}}{Q_l^{5/6}} - \frac{0.19(1+0.24\Lambda Q_l)^{1/4}}{Q_l^{5/6}}\Bigg]\Bigg\} \end{aligned} \tag{3.24}$$

and the large-scale log-irradiance variance is

$$\begin{aligned}\sigma_{\ln X}(l_0) &= 0.49\sigma_R^2\left(\frac{1}{3}-\frac{1}{2}\bar{\Theta}+\frac{1}{5}\bar{\Theta}^2\right)\left(\frac{\eta_X Q_l}{\eta_X+Q_l}\right)^{7/6} \\ &\qquad \left[1+1.75(\frac{\eta_X}{\eta_X+Q_l})^{1/2}-0.25(\frac{\eta_X}{\eta_X+Q_l})^7/12\right] \\ \sigma_{\ln X}(L_0) &= 0.49\sigma_R^2\left(\frac{1}{3}-\frac{1}{2}\bar{\Theta}+\frac{1}{5}\bar{\Theta}^2\right)\left(\frac{\eta_{X0} Q_l}{\eta_{X0}+Q_l}\right)^{7/6} \\ &\qquad \left[1+1.75(\frac{\eta_{X0}}{\eta_{X0}+Q_l})^{1/2}-0.25(\frac{\eta_{X0}}{\eta_{X0}+Q_l})^7/12\right] \end{aligned} \tag{3.25}$$

and the nondimensional cutoff frequencies for the inner and outer scales are given by

$$\begin{aligned}\eta_X &= \left[\frac{0.38}{1-3.21\bar{\Theta}+5.29\bar{\Theta}^2}+0.47\sigma_R^2 Q_l^{1/6}(\frac{\frac{1}{3}-\frac{1}{2}\bar{\Theta}+\frac{1}{5}\bar{\Theta}^2}{1+2.20\bar{\Theta}})^{6/7}\right]^{-1} \\ \eta_{X0} &= \frac{\eta_X Q_0}{\eta_X+Q_0}\end{aligned} \tag{3.26}$$

where the outer scale parameter $Q_0 = L\kappa_0^2/k$, inner scale parameter $Q_l = L\kappa_l^2/k$, $\varphi_0 = \tan^{-1}(\frac{2\Lambda}{1+2\Theta})$, and $\varphi_l = \tan^{-1}(\frac{(1+2\Theta)Q_l}{3+2\Lambda Q_l})$.

3.3.2.3 Long-Term Beam Size

The details of the long-term spot size depend on the relationship between the propagation distance L and the distance at which the transverse coherence length of the beam is equal to the inner scale.

The distance at which the transverse coherence radius of the Gaussian beam becomes equal to the inner scale is given by:

$$z_i = 1/(C_n^2 k^2 l_0^{5/3}) \tag{3.27}$$

Under the limiting cases of propagation over a distance much greater than, or much less than z_i, and in the absence of outer-scale effects, the long-term spot size for a Gaussian beam is given by:

$$\begin{aligned} R_{LT}^2 &= R^2 \left(1 + 0.982\sigma_R^2 \Lambda Q_m^{1/6}\right), \text{ for } L \gg z_i \\ &= R^2 \left(1 + 1.630(\sigma_R^2)^{6/5}\Lambda\right), \text{ for } L \ll z_i \end{aligned} \tag{3.28}$$

where R is the radius of the beam in the absence of turbulence. The long-term spot size includes independent contributions from both instantaneous spreading and breakup of the beam, as well as the random wander of the beam centroid over time [27]. The contributions sum in quadrature, as before:

$$W_{LT}^2 = W_{ST}^2 + \sigma_{cen}^2 \tag{3.29}$$

3.3.2.4 Beam Wander

Under strong fluctuation conditions, the beam wander is given by

$$\sigma_c^2 = 7.25 C_n^2 L^3 R_0^{-1/3} \int_0^1 \xi^2 \left[\frac{1}{(\Theta_0 + \bar{\Theta}_0 \xi)^2 + 1.63 \sigma_R^{12/5} \Lambda_0 (1-\xi)^{16/5}} - \frac{(\kappa_0 R_0)^{1/3}}{\left\{ 1 + \kappa_0^2 R_0^2 \left[(\Theta_0 + \bar{\Theta}_0 \xi)^2 + 1.63 \sigma_R^{12/5} \Lambda_0 (1-\xi)^{16/5} \right] \right\}^{1/6}} \right] d\xi \quad (3.30)$$

This expression has no closed-form analytic solution. It is the general expression for beam wander under all conditions. For $\sigma_R^2 \ll 1$ it reduces to Equation 3.14; therefore, it will be evaluated numerically to model beam wander under both weak and strong turbulence.

3.3.2.5 Short-Term Beam Size

As is the case for weak turbulence, the short-term beam size under strong turbulence conditions can be constructed by combining Equations 3.30 and 3.28 in accordance with Equation 3.29. Combining these equations yields no algebraic simplification or additional insight; therefore, the full expression is not presented explicitly here.

Chapter 4: Artificial Turbulence Generation

4.1 Overview

Outdoor field experiments to study the effects of turbulence in a natural setting are complicated by natural uncontrollable variation in turbulence strength. Laboratory turbulence simulators using spatial light modulators or phase plates do not correctly capture the nonlinear dynamics of atmospheric propagation, and are not robust against interaction with high-power laser pulses. Fluid-based artificial turbulence generators offer a way to study turbulence under controlled laboratory conditions, without being subject to the limitations of turbulence simulators. The turbulence generator used in this work operates by heating a long, narrow volume of air and allowing free convection to create turbulence similar to that observed in nature. This turbulence generator has been demonstrated to generate turbulence with statistical properties similar to those seen in a natural outdoor environment.

4.2 Turbulence Experiments Outdoors

Experimental turbulence research can often be performed in the field, simply by allowing the laser to propagate across a long distance. The strength of optical

turbulence is characterized by C_n^2, the coefficient of the structure function for the index of refraction. In the surface layer of the atmosphere, less than ∼100 meters above the ground, C_n^2 experiences natural daily variation over several orders of magnitude as the ground heats and cools with the rising and setting of the sun. A typical example of daily C_n^2 variation is presented in Figure 4.1. This data was collected via differential image motion monitor (DIMM) [28], operating at a wavelength of 632.8 nm, on a clear day in early September 2008. This record includes a pronounced "null event," a rapid decrease in C_n^2 associated with sunrise and sunset. A large range of turbulence conditions can be sampled by observing the laser propagation throughout the day.

Many outdoor ranges suitable for long-distance laser propagation exist, including at Starfire Optical Range [29], the U.S. Naval Academy [30], across the Chesapeake Bay [31] and at the former Space Shuttle runway [32], among others. However, long-range outdoor experiments have the disadvantage of relying on uncontrollable natural variations, and the desired turbulence conditions may not occur during the experimental window. Many hours of experiment are required in order to secure a reasonable volume of data, which in any case will necessarily be under conditions which are not entirely known. In addition, laser safety considerations preclude the propagation of high-power beams at many outdoor ranges.

For these reasons, many techniques have been developed in order to generate or simulate turbulence in a more compact, more controllable manner in a laboratory setting [33]. These include a variety of fixed and variable phase screen methods, as well as turbulent fluid methods.

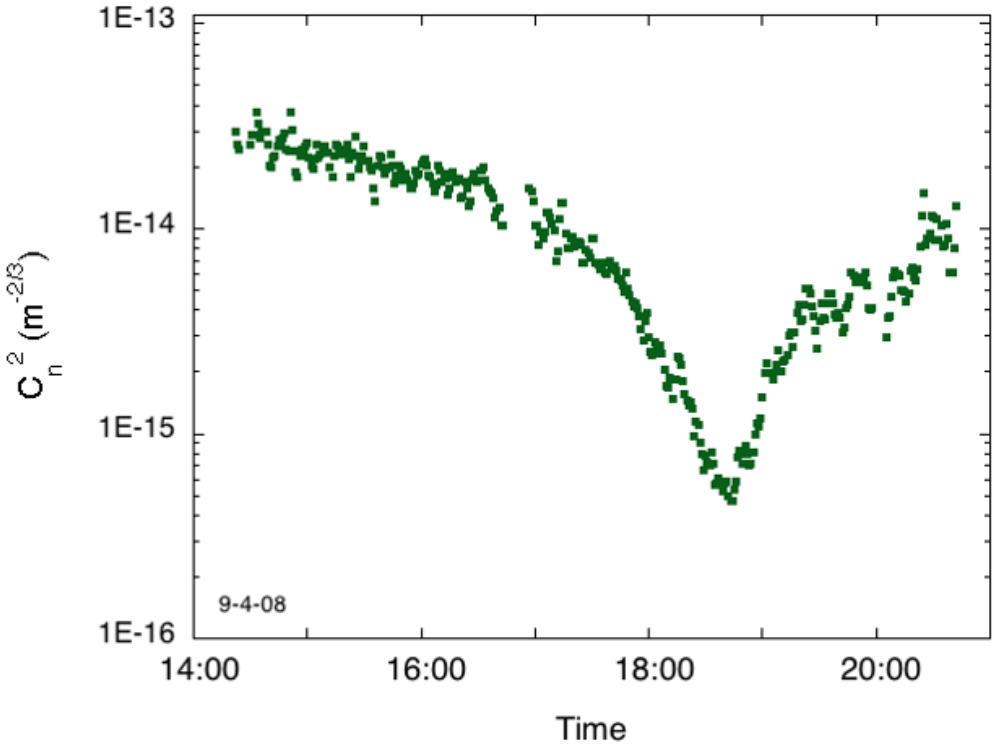

Figure 4.1: A typical day of C_n^2 variation taken at Kirtland AFB, Albuquerque, NM. Note the pronounced evening null event, and the accompanying rapid variation of turbulence across several orders of magnitude.

Fluid-based turbulence generators adopt perhaps the most direct approach to generating turbulence short of performing field experiments. A volume of air, water, or some other fluid is stirred via some combination of mechanical action (pumps, fans, or jets) and thermal action (heat guns, hot plates, heater wires). Gradients in temperature result in turbulent fluctuations of the index of refraction. This method has several advantages: realistic Kolmogorov turbulence is naturally obtained; the strength of the turbulence is easily tuned by varying the strength of the heating; rare events such as intense scintillations naturally occur with the appropriate frequency; the turbulence is distributed along the path rather than being tightly concentrated at one or a few longitudinal positions; appropriate construction materials are typically far cheaper than custom phase screens or deformable optics. The disadvantages are as follows: the inner and outer scales cannot be varied independently of C_n^2; the turbulence is truly random and cannot be reproduced except in a statistical sense; the generator occupies a large volume relative to phase screens; the heat used to generate the turbulence must be dissipated in some manner [33]. Turbulent fluid methods are well-suited for the study of high-power propagation because there are no physical optics, such as phase screens or spatial light modulators, which could be damaged by the high-power beam. Additionally, if the fluid used is air, it correctly captures the nonlinear properties of actual atmospheric laser propagation.

4.3 Previous Turbulence Generators

Davis has developed a hot-liquid turbulence generator for creating turbulence on laboratory scales [34]. A diagram of the experimental apparatus is shown in Figure 4.2. This device uses a heating wire at the bottom of a liquid-filled acrylic tube to generate a temperature differential. The tube is generally filled with water, although other liquids can be used. The liquid can be allowed to convect naturally, or a pump can be used to provide additional stirring. The pump must be run from time to time, or the liquid will reach a uniform temperature and cease to exhibit turbulence. This method allows a large phase difference to be produced in a short distance. However, the turbulence evolves much more slowly than in air, and the inner scale is substantially larger than in air, owing to water's higher viscosity.

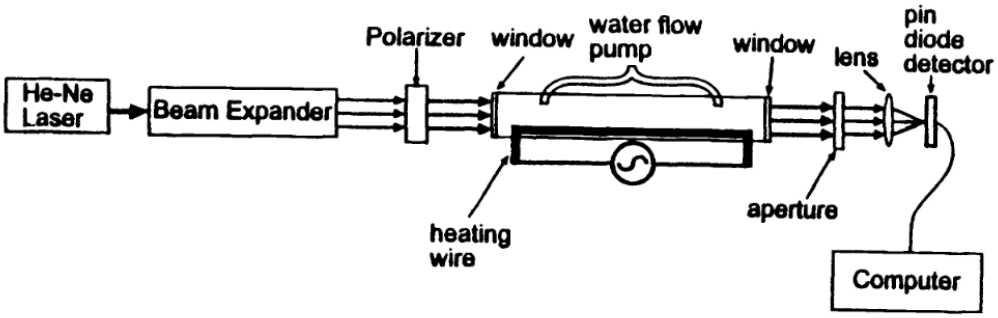

Figure 4.2: Schematic arrangement of Davis' 1998 experiment incorporating the hot-liquid turbulence tube.

Majumdar, C. Nelson, and Keskin have all developed flow-driven hot-air turbulence generators [30, 35, 36]. These similar devices all operate by directing one

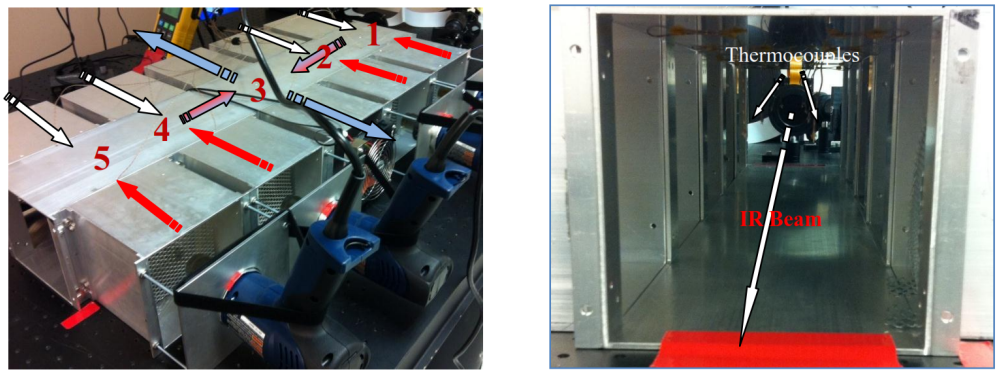

(a) (b)

Figure 4.3: C. Nelson's flow-driven hot air turbulence generator. Panel a: exterior view with the directions and relative temperatures of flow marked, as well as the positions of the five turbulence sections. Figure b: interior view with the direction of laser propagation marked.

or more pairs of hot and cold air flows into a semi-enclosed chamber. Photographs of C. Nelson's device are displayed in Figure 4.3 as an example of the type. The air flows enter the chamber perpendicular to the beam propagation path, with each hot nozzle more or less opposed by a cold nozzle. The air leaves the chamber via the laser entrance and exit ports, as well as additional exhausts. The strength of turbulence is adjusted by varying the temperature difference between the air jets, as well as the speed of the flow. This method produces a more rapidly evolving turbulence. However, no obvious relationship exists between temperature / flow speed and turbulence strength. The energy dissipation rate, useful for estimating the inner scale of turbulence (Equation 2.12), is unclear.

Finally, convection-driven turbulence generators have been used by Salamé and W. Nelson [37,38]. Salamé used a series of candles placed below his beam path

rather than an evenly distributed turbulent volume, in effect producing a series of randomly varying gaseous phase screens. W. Nelson has used a series of hot plates to generate distributed turbulence over a short distance, approximately 3 meters. A diagram of W. Nelson's experimental setup is displayed in Figure 4.4. By arranging the beam path over the hot plates, W. Nelson could produce a situation in which the turbulence experienced by the light returning from the target to the imaging camera experienced turbulence which was either identical to, or different from, the turbulence experienced by the outgoing laser beam.

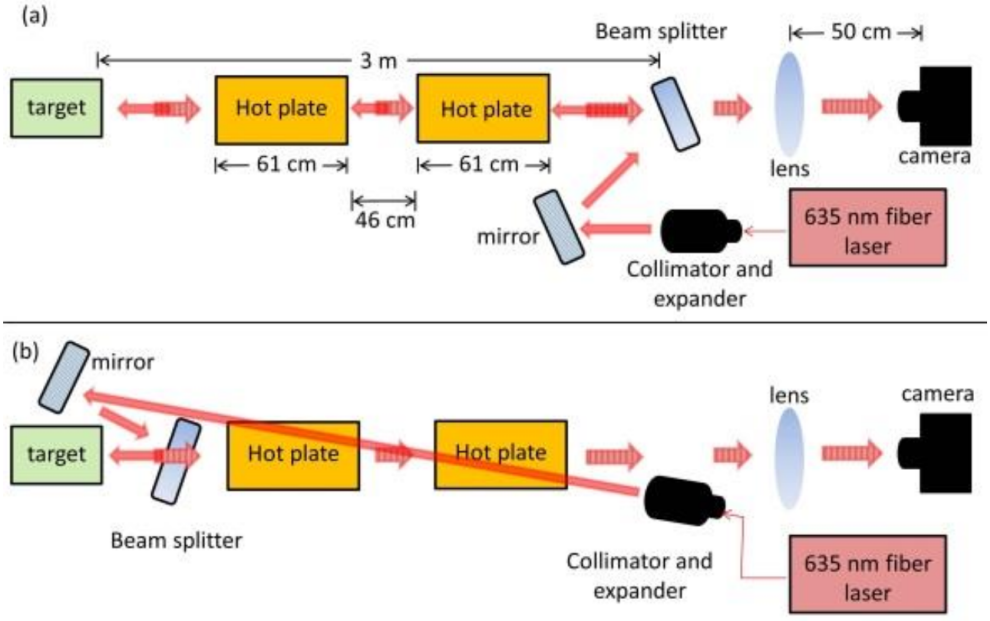

Figure 4.4: Schematic of W. Nelson's convection-driven turbulence generator. Panel a: monostatic beam propagation path with outgoing and incoming beams experiencing identical turbulence. Panel b: bistatic path with outgoing and incoming beams experiencing different turbulence.

4.4 This Work's Approach

4.4.1 Theoretical Background

In the lowest layers of the atmosphere near the surface, atmospheric turbulence is driven primarily by natural convection of hot air rising from the sun-warmed ground. A natural approach to generating artificial turbulence is therefore to heat some object placed below the propagation range and allow convection to drive turbulence. A long cylindrical heating element, such as a heating wire, allows the generation of turbulence along the beam's entire propagation path while consuming only a modest amount of power - on the order of 10 watts per meter.

The behavior of flow due to natural convection is characterized by the nondimensional local Nusselt number Nu, the ratio of convective to conductive heat transfer rates (q_{conv} and q_{cond}, respectively). For large values of Nu convection dominates over conduction; for small values the reverse is true. Consider a layer of air of thickness x above a heated surface; the Nusselt number at the top of that layer is given by

$$\mathrm{Nu}_x = \frac{q_{conv}}{q_{cond}} = \frac{h\Delta T}{\mathrm{k}\frac{\Delta T}{x}} = \frac{hx}{\kappa} \tag{4.1}$$

where h is the geometry-dependent convective heat transfer coefficient in $W/m^2 \cdot K$, ΔT is the temperature difference between the heated surface and the ambient fluid, and k is the thermal conductivity of the fluid in $W/m \cdot K$. The local Nusselt number increases with height above the source, as the air layer becomes thicker and

conduction becomes less important compared to convection. Below a critical Nusselt number, between 100 and 1000, the flow remains laminar. Beyond this point, heat transfer is dominated by fluid motion and the flow is considered to be turbulent. For fully developed turbulence with infinite Nusselt number, no deterministic behavior resulting from large-scale laminar flows remains.

Some difficulty lies in determining the convective heat transfer coefficient h, which is influenced by the geometry of the problem and the ability of air to flow around the heated surface. Experimentally determined correlating equations, relating the Nusselt number for the flow around a horizontal cylinder to other fluid mechanical parameters, have been developed by Churchill et al [39]. From their analysis, the convective heat transfer coefficient is given by

$$h_{cyl} = \frac{\mathrm{k}}{D}\left(0.6 + \frac{0.387\mathrm{Ra}_D^{1/6}}{(1+(0.559/\mathrm{Pr})^{9/16})^{8/27}}\right)^2 \tag{4.2}$$

where Pr is the Prandtl number for air (0.713 at 20 °C), Ra_D is the Rayleigh number for scale size D, and D is the diameter of the cylinder. The numerical factors have been determined experimentally through curve fitting over a wide range of Rayleigh numbers, $10^{-5} < Ra_D < 10^{12}$.

The nondimensional Rayleigh number, Ra, characterizes whether the flow around a heated object will be predominantly convective or conductive. The Rayleigh number for scale size x is given by

$$\mathrm{Ra}_x = \frac{\rho g \beta \Delta T x^3}{\alpha \mu} \tag{4.3}$$

where ρ is the density, g is the acceleration due to gravity, β is the coefficient of thermal expansion, α is the thermal diffusivity, and μ is the fluid's dynamic viscosity.

4.4.2 Implementation

This section reports on the construction and characterization of a hot-air continuously variable distributed turbulence generator. Two copies of this generator were constructed: one, over a distance of 30 meters, at NRL; and one, over a propagation range of 180 meters, at an indoor laser propagation range at AFRL. At the time, the latter device constituted to the author's knowledge the world's longest continuously variable optical turbulence generator.

The generator, depicted symbolically in Figure 4.5, consists of a cluster of industrial heating wires strung on steel cables running below the beam propagation path. Each wire is 73 meters long. Tension on the steel cables and a series of quadrupods positioned periodically along the path support the wires at a fixed distance below the beam. As the wires are heated, buoyant hot air from the wire convects upwards to mix with the ambient air of the lab. Laboratory HVAC systems remove the excess heat and prevent the average temperature of the lab from increasing. Since the turbulence is driven by natural convective mixing, this method is more akin to a hot water chamber or a series of hot plates than it is to typical flow-driven hot-air tubulence generators. The strength of turbulence can be varied by adjusting the amount of power applied to the heater wires. The power consumed by the wires gives the rate of energy dissipation ϵ; this will enable comparison between

the turbulence spectrum produced by the generator and theoretical predictions (for instance, equations 2.7 and 2.12). Because it generates a continuously-distributed turbulent volume in air by the process of free convection, this hot-wire turbulence generation method will henceforth be referred to as the Generator of Distributed Free Atmospheric Convective Turbulence (GDFACT).

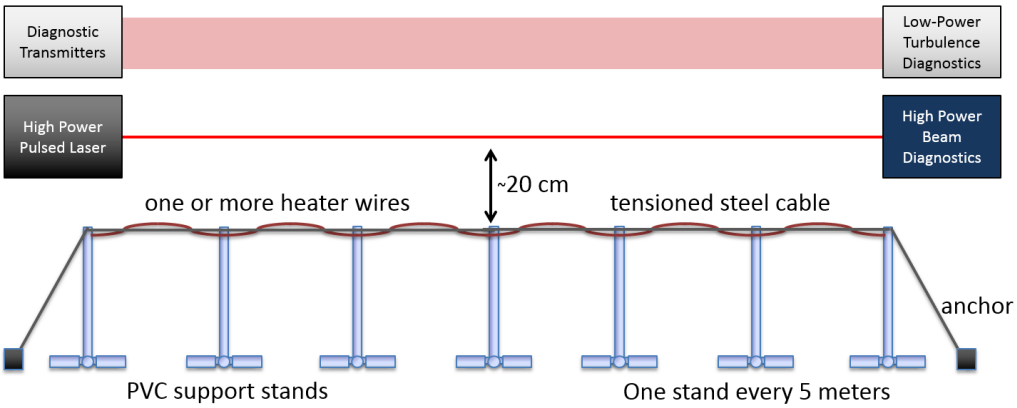

Figure 4.5: A symbolic diagram of the GDFACT. Heater wires strung on an extended framework running below the beam propagation path impart thermal and kinetic energy into the air, which naturally produces realistic Kolmogorov turbulence. Turbulence diagnostics co-propagate with the laser beam, characterizing the turbulence as the experiment takes place.

GDFACT shares the advantages of all turbulent fluid-based generators. It naturally produces tunable, continuously-distributed Kolmogorov turbulence at a low cost. More importantly, it is compatible with high-power laser propagation, in that it contains no physical optics to be damaged by the beam. It also produces natural variation in both the linear and nonlinear indices of refraction.

There are two downsides to this method. First, it is based on a line source of turbulence, rather than a plane source as in propagation over land. As the beam

propagates, care must be taken that the beam not wander or spread beyond the narrow corridor of turbulent air. This disadvantage can be alleviated by stringing several heater wires side-by-side, creating a broader propagation path. This work was performed using a line source turbulence generator; future work in this field would benefit from the use of a broad multiple-wire device capable of accommodating a larger beam with more wander. Second, since the strength of the turbulence is comparable to that found in nature, a long indoor propagation range is necessary in order to reach deep turbulence ($\sigma_{\mathrm{R}}^2 \geq 1$). This can be alleviated by placing high-power dielectric mirrors at the ends of the propagation range and performing multiple passes over the turbulence generator. The use of such mirrors, however, is limited by their optical damage threshold, and care must be taken to ensure that filamentation does not occur.

For the first set of experiments, the wires were strung 20 cm below the beam propagation path; this separation can be adjusted from an arbitrarily small distance up to as much as 1 meter. The 20 cm separation was chosen to provide a scintillation index of 1 for a helium-neon laser (He-Ne, $\lambda = 632.8$ nm) at the highest heater setting, 22.3 W/m per wire. Under these conditions, buoyancy carries the air flow up across the beam; this is like having a weak transverse wind, in which case the Taylor Frozen Flow hypothesis is expected to apply [7].

The heater wires were measured to reach a temperature of 65 C above ambient. The corresponding Nusselt number 20 cm above the wires is approximately 100. This is marginally within the range of Nusselt numbers considered to be characteristic of turbulent flow; therefore, the turbulence thus generated may not exhibit fully

Kolmogorov statistics.

4.5 Characterization of the Turbulence Generator

4.5.1 Overview

A constant temperature anemometer was used to characterize the spectrum of velocity fluctuations produced by the GDFACT. The turbulence spectrum was found to be Kolmogorov within the inertial subrange, with an inner scale of approximately 1 cm at full power. In addition, the optical turbulence was characterized at a variety of power settings, using the scintillometer and LISSD diagnostics described in Chapter 2. The scintillometer and LISSD were found to agree with one another except for the lowest power settings. The inner scale determined by LISSD was found to agree with that determined by CTA.

4.5.2 Anemometer

At NRL, the turbulence produced by GDFACT was measured with the CTA to verify that its statistics match those of natural atmospheric turbulence. These spectra were compared to naturally-occurring turbulent velocity fluctuations one meter above a concrete parking lot. In each case, the structure function was generated by using the Taylor frozen-flow hypothesis to convert time-resolved data into space-resolved data [6]. The structure function takes a long time to compute (a naive calculation requires a number of comparisons $\mathcal{O}(n^2)$), so instead it is calculated from the correlation, using equation 2.5 and the Wiener-Khintchine Fourier

transform relation [7], as follows:

Analysis begins with $V(t)$, the voltage as a function of time. This can be converted to $v(t)$, the velocity as a function of time, via the CTA manufacturer-supplied calibration formula

$$v(t) = c_0 + c_1 V(t) + c_2 V(t)^2 + c_3 V(t)^3 \tag{4.4}$$

where $c_0 = 0.546\ m/s$, $c_1 = 3.29202\ m/s$ per V, $c_2 = 3.03385\ m/s$ per V^2, and $c_3 = 34.1096\ m/s$ per V^3.

The Taylor frozen-flow hypothesis is used to convert the time-series to a space-series according to $R = t\bar{v}$, where $\bar{v}$ is the average velocity in the velocity-time series.

Next the Fourier transform of velocity is calculated, and squared to get the power spectral density of velocity,

$$S_v(\kappa) = \left| 2 \int_0^\infty v(R) \cos(\kappa R) dR \right|^2 \tag{4.5}$$

From the power spectral density, the correlation function is calculated according to:

$$B_x(R) = 2 \int_0^\infty S_x(\kappa) \cos(\kappa R) d\kappa \tag{4.6}$$

Given the correlation function $B_x(R)$, the structure function $D_x(R)$ can be calculated from equation 2.5. This approach is less straightforward than calculating the structure function directly from the velocity fluctuations, but is significantly more computationally efficient, executing in $\mathcal{O}(n \log n)$ rather than $\mathcal{O}(n^2)$.

The one-dimensional power spectrum of the structure function is then calcu-

lated according to 2.6, in order to facilitate comparison between theory and experiment.

This spectrum demonstrates a slope of approximately $-5/3$, as expected for Kolmogorov turbulence. These results are presented in Figure 4.6. The $-5/3$ slope predicted by Kolmogorov and observed in the natural outdoor environment is reproduced in the experiment.

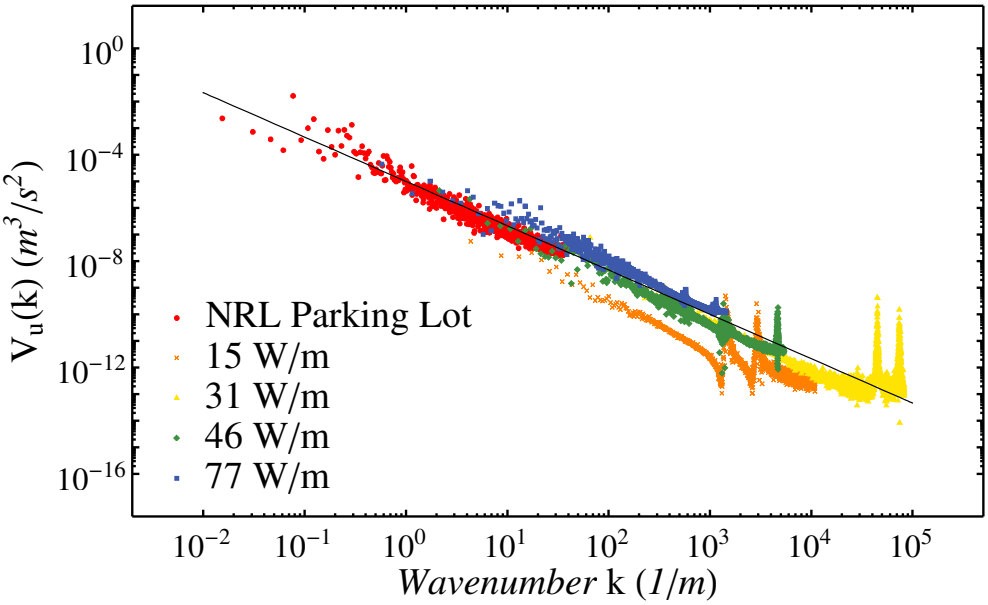

Figure 4.6: One-dimensional velocity turbulence power spectra $V_u(k)$ for a naturally turbulent atmosphere (NRL parking lot, red), and four power density settings on the GDFACT (orange through blue). A $-5/3$-slope line is displayed in black. High-wavenumber peaks on each data set represent high-frequency instrumental noise related to the oscilloscope sampling frequency.

Fiorino *et al* have shown that the coefficient of the velocity power spectrum, C_v^2, can be related to C_n^2, the gradient of the index of refraction, and the vertical gradient of the wind velocity [40]. Unfortunately, an insufficient number of

anemometers were available to collect wind velocity gradient information in order to apply this technique. In addition, the inner scale of turbulence cannot be resolved. However, these results provide evidence that within the inertial subrange, the GDFACT is creating Kolmogorov turbulence similar to that encountered in a natural environment.

A separate experiment was recently performed in order to measure the inner and outer scales. This experiment was performed on a second-generation GDFACT, consisting of four heater wires in parallel with one inch spacing between them. Velocity fluctuations were measured via CTA, as before. Following the method of Champagne [41], the power spectrum of the derivative of the velocity was calculated. This quantity, the square of the Fourier transform of the derivative of the velocity, is presented in Figure 4.7. Each point is the average over a wavenumber bin with equal width on a log scale. The plotted data is the average of ten such binned measurements, with error bars representing the standard deviation for each point. The expected slope of 1/3 is observed within the inertial subrange. The inner scale, the high-wavenumber point at which the inertial subrange ends, is observed to be approximately 1 cm; the outer scale, the equivalent low-wavenumber point, is observed to be approximately 30 cm. This corresponds to the CTA's height above the GDFACT when this data was taken.

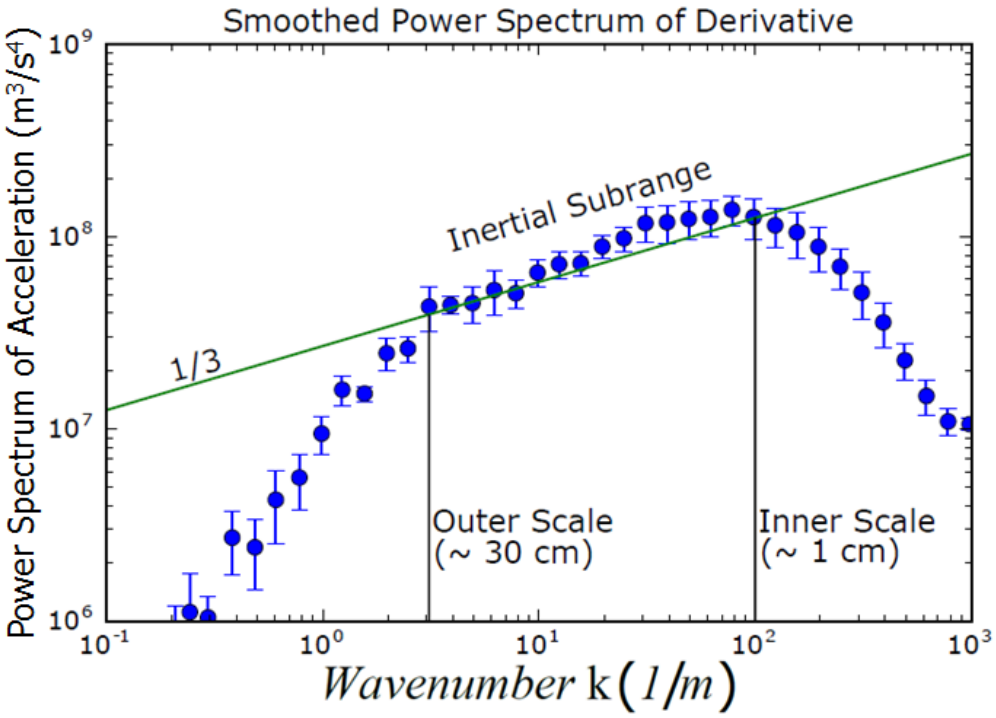

Figure 4.7: One-dimensional acceleration turbulence power spectra $V_u(k)$ for the GDFACT. The effects of the inner and outer scales are plainly visible.

4.5.3 Optical Techniques

Optical characterization of the GDFACT was first performed at the NRL experimental site. At NRL, the propagation path runs between a short-pulse laser and the wall of the lab; it is too narrow for the scintillometer to fit. Therefore, only LISSD data was collected.

The turbulence produced by GDFACT at the NRL range was measured via LISSD, as a function of electrical power applied to the wires; these results are presented in Figure 4.8. The baseline value of $\sim 10^{-14}$ is somewhat higher than might be preferred; this is likely due to the presence of fans and chillers necessary for the operation of the short-pulse laser. Nevertheless, GDFACT is able to produce an increase of two orders of magnitude in C_n^2.

At AFRL, concurrent measurements of the structure function were made concurrently by scintillometer and LISSD, as a function of electrical power applied to the wires. However, the baseline turbulence at AFRL is so low that it was sometimes below the minimum detection threshold of the scintillometer. Therefore, in the low-turbulence regime the results of the LISSD are considered to take precedence.

Measurements of the optical turbulence produced by GDFACT were performed at a variety of power levels, as well as with the facility HVAC system turned both on and off. The results are displayed in Figures 4.10 and 4.9. At the maximum power level of 45 W/m, the intensity fluctuations caused dynamic range saturation in the LISSD detector; therefore, this data has been omitted. This dynamic range saturation is a result of the 8-bit color camera used for the LISSD; this limited the

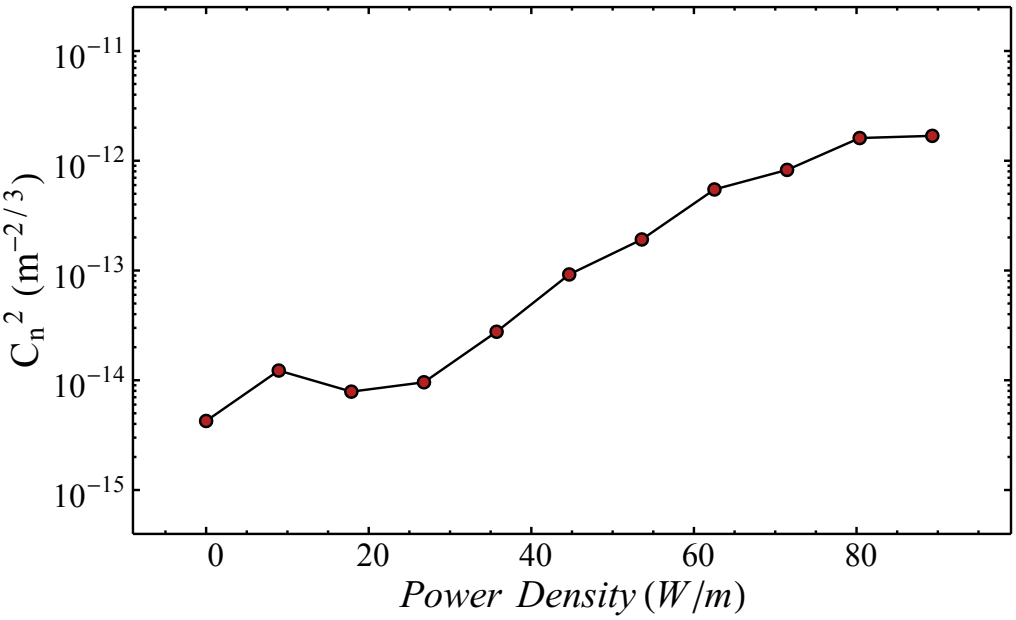

Figure 4.8: Optical characterization of the NRL installation of GDFACT via LISSD. The laboratory HVAC system remained on for this test.

size of the intensity fluctuations to a factor of 255. This deficiency was corrected in the laser propagation experiments which were later performed at AFRL (presented in Chapter 7).

With the HVAC system turned off the turbulence in the propagation range is extremely weak, with C_n^2 as low as $10^{-16}\mathrm{m}^{-2/3}$ leading to a scintillation index as low as 10^{-4}. Activating the HVAC system increases this baseline level of turbulence by approximately an order of magnitude. At heater settings above 5 W/m, the turbulence produced by GDFACT dominates the natural turbulence of the facility, and the effect of the HVAC system becomes insignificant.

The C_n^2 values displayed in Figure 4.9 are calculated under the assumption of weak Kolmogorov turbulence, and are therefore subject to the same conditions.

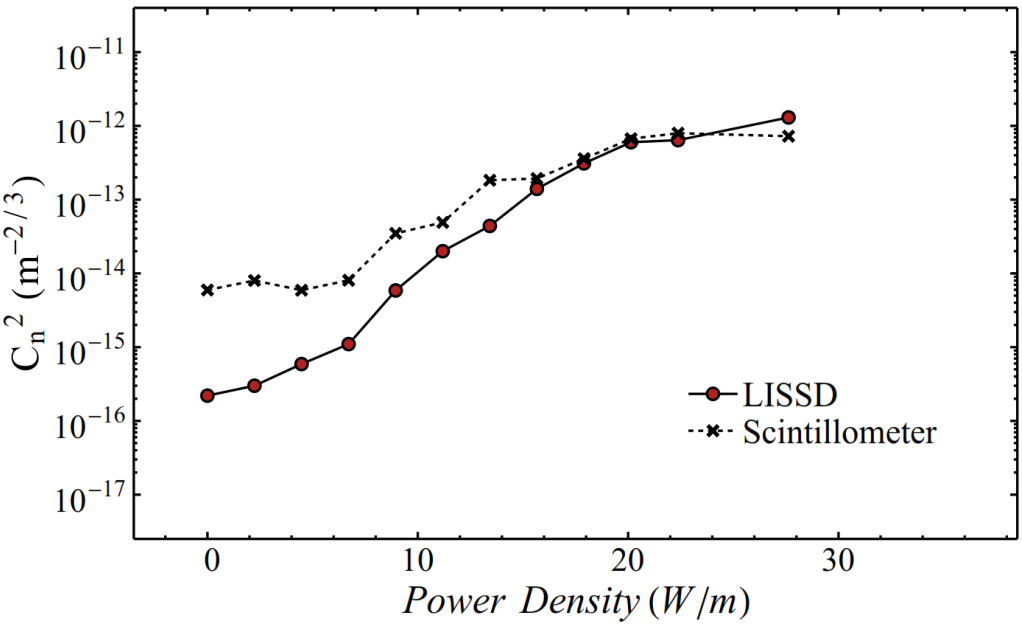

Figure 4.9: Optical characterization of the GDFACT via LISSD. The solid line represents the structure parameter C_n^2, as determined from LISSD scintillation data under the weak turbulence approximation, equation (2.17). The dotted line represents the C_n^2 output from the commercial scintillometer. The laboratory HVAC system remained off for this test.

The agreement between the LISSD-derived values and those obtained from the commercial scintillometer is observed to be excellent, except at the lowest turbulence intensities. The scintillometer performs a significant amount of space averaging by focusing a large collection aperture (10 cm diameter) onto its internal detector; this renders the device resistant to large-amplitude scintillation saturation [22], but also averages out small fluctuations. This places an effective lower limit on the strength of the scintillations which the scintillometer can observe. The LISSD, which uses a small sampling aperture, does not have this limitation.

The scintillation index and angle-of-arrival fluctuations displayed in Figure 4.10 are based directly on observation. The inner scale plotted in Figure 4.10b has been calculated using equation 2.18, and hold under the conditions given by [24]; namely, that $L \ll l_0^2/\lambda$, and that the turbulence is Kolmogorov. Of these conditions, the first holds for all but the highest power settings. For a He-Ne laser and an inner scale of 1 cm, the limiting length is 158 meters. This is on the order of our propagation distance; therefore, for the highest powers the actual inner scale may be somewhat smaller than depicted. The calculation of the Nusselt number ($\sim$100 at full power) gives us reason to believe that the second condition may not hold for lower power levels. However, anemometer measurements indicate that GDFACT produces a power spectrum similar to that of natural turbulence; see Figure 2.3.

The angle-of-arrival fluctuations and inner scales reported in Figure 4.10 are averages of the x- and y-components determined by Consortini's method. A slight anisotropy exists: the y-component is more often larger than the x-component (23 out of 31 runs). On average, the y-component of the angle-of-arrival fluctuations,

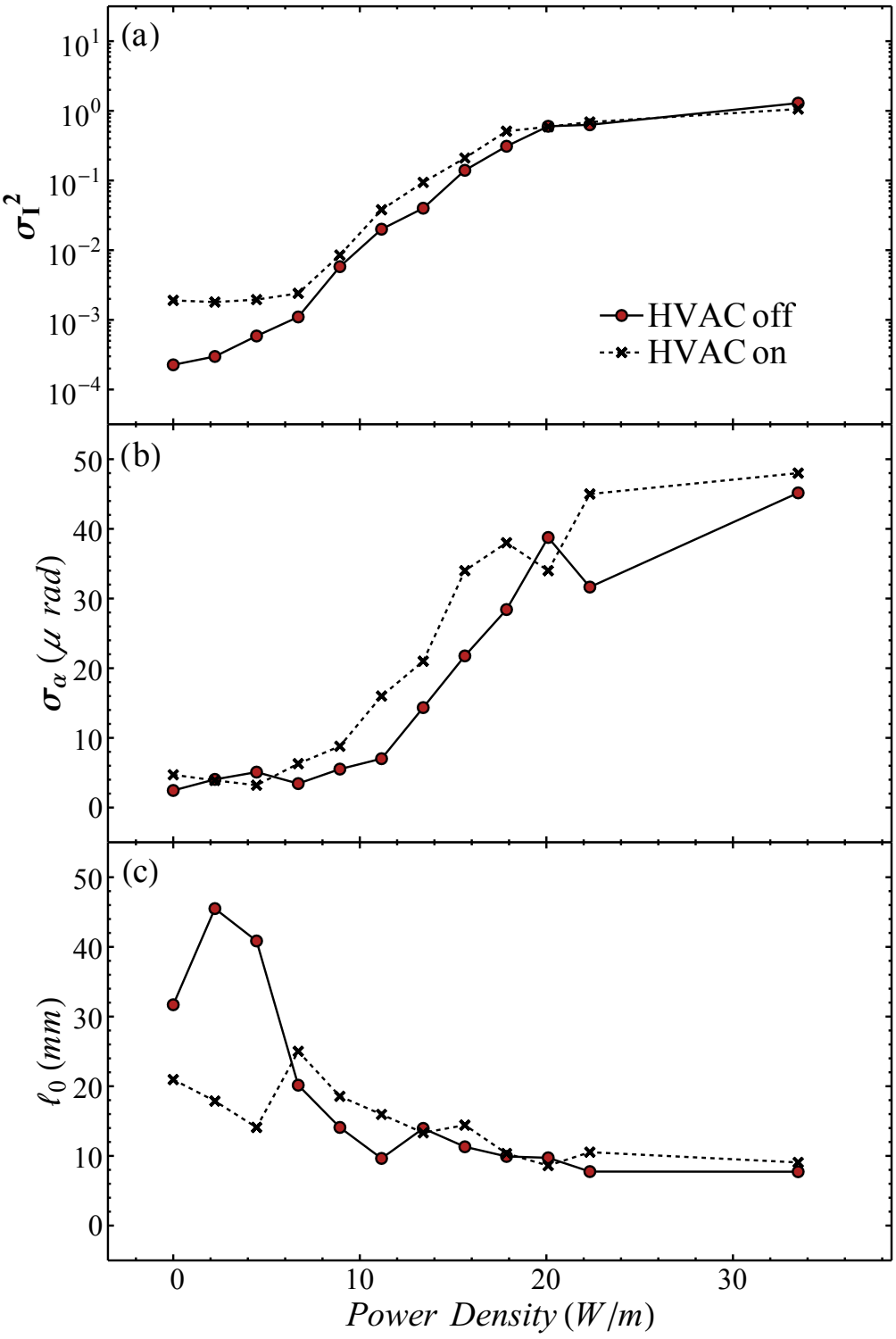

Figure 4.10: Optical characterization of the GDFACT via LISSD. a) Scintillation index. b) Standard deviation of the angle of arrival. c) Inner scale, determined according to the method of Consortini, equation (2.18).

and thus the inner scale in the y-dimension, is 9.75% larger than the x-component. This difference is too small to be visible in Figure 4.10; therefore, only the average has been presented. The anisotropy may result from the average flow of air upward from the hot wires of the turbulence generator.

4.6 Modeling and Simulation

To benchmark propagation models, simulations were performed of the propagation of a low-power He-Ne laser beam through the turbulence generated at the AFRL range. Simulations were performed using the High Energy Laser Code for Atmospheric Propagation (HELCAP), a 4D (3D space + time) computer simulation code developed at NRL [42,43]. With the turbulence generator turned off, the initial divergence of the He-Ne laser beam was determined by measuring the laser spot size in the transmitter and receiver planes. The ambient turbulence was not sufficient to affect the beam divergence angle.

With the initial divergence angle and spot size of the He-Ne beam established, C_n^2 and the inner scale were varied in the simulations according to the measured values. The simulated beam was propagated 180 meters through the turbulence (assumed to be homogenous). HELCAP does not natively include buoyant convection; to mimic the effect of heat convection from the wires, a vertical wind was used in the simulation with speed equal to the buoyancy speed associated with the temperature of the wires.

Simulated beam images were compared with observed beam images in the re-

ceiver plane for various turbulence conditions (Figure 4.11). Over the majority of the experiments, which produced a wide range of turbulence intensities (including both weak and strong turbulence regimes), it was observed that turbulence did not significantly increase the spot size of the beam in the receiver plane. Weak turbulence was observed to produce large-scale structures that convect across the beam, while strong turbulence produced smaller-scale convecting filamentary structures. The same behavior was observed in the simulations, which were in good qualitative agreement with the experiments over the entire range of turbulence measured. This behavior is to be expected in the parameter regime for "case 3" of Fante's seminal paper [5], in which there is very little beam spreading but high incoherence can occur. A example comparison of beam intensity in the receiver plane between experiments and simulations is shown in Figure 4.11 for weak turbulence ($C_n^2 = 6 * 10^{-14} m^{-2/3}$, $\sigma_I^2 = 0.15$, frames a and c) and strong turbulence ($C_n^2 = 5 * 10^{-13} m^{-2/3}$, $\sigma_I^2 = 1.2$, frames b and d) cases.

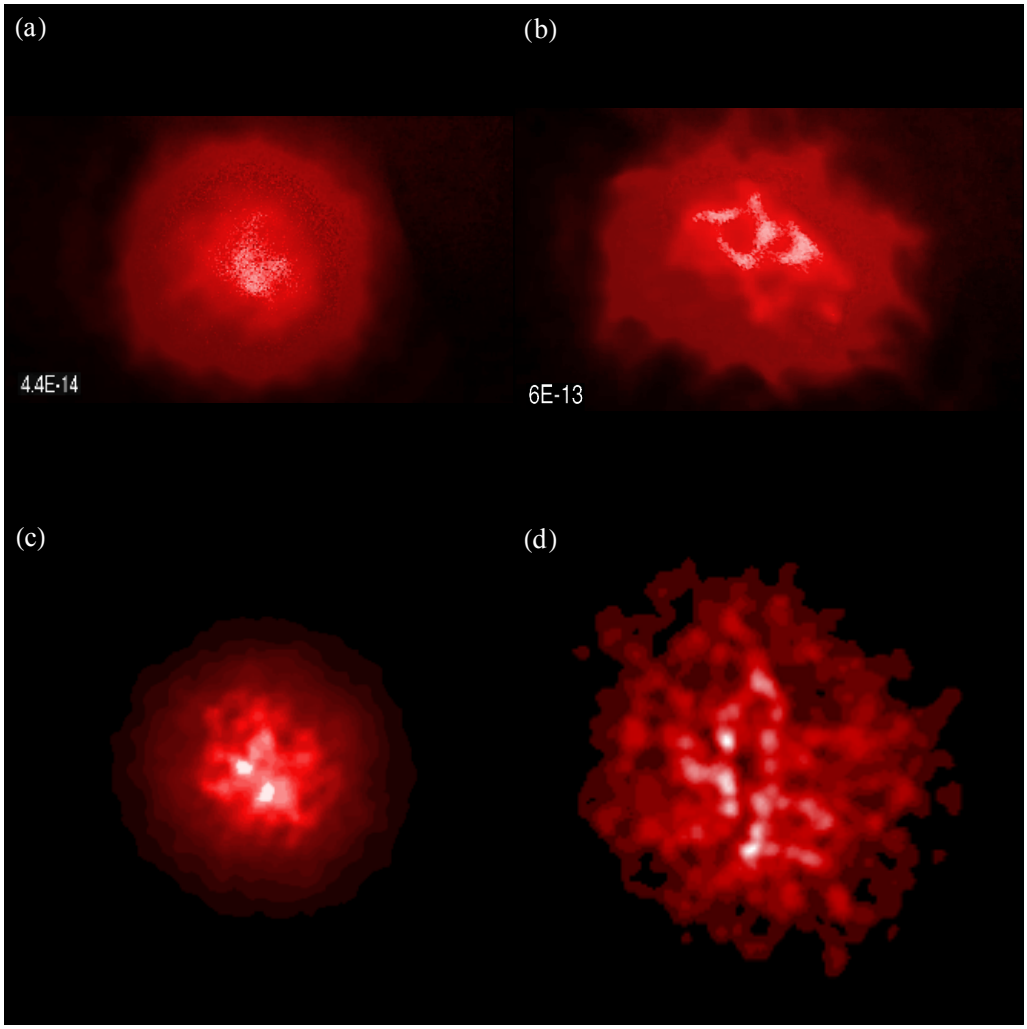

Figure 4.11: Qualitative comparison between experimental and simulation results. a) and b) Still frames from video of laser beam scattered off target board in front of LISSD. c) and d) Still frames of animation produced in HELCAP. The spot size and fine beam structure observed in experiment are qualitatively reproduced in simulation. Low dynamic range of the camera prevents quantitative comparison of these images.

Chapter 5: Nonlinear Beam Propagation

5.1 Overview

The propagation of a laser beam is changed fundamentally once the intensity of the beam becomes great enough to alter the optical properties of the medium through which is propagates. A variety of nonlinear processes are capable of taking place. For the purposes of the present work, the most important is nonlinear self-focusing, in which the index of refraction of air increases with increasing laser intensity, resulting in transverse focusing of a Gaussian beam proportional to the laser power. The nonlinear self-focusing effect allows high-power beams to propagate many Rayleigh lengths while remaining below the inner scale of turbulence, thus enabling the nonlinear self-channeling which is the focus of this work.

5.2 Without Turbulence

Even in the absence of turbulence, a high peak power laser pulse propagates through the atmosphere in a manner both quantitatively and qualitatively different from that of an ordinary low power laser. This is due to nonlinear interaction with the matter of the atmosphere through which the pulse propagates [44, 45].

In addition to the usual linear atmospheric effects of diffraction, dispersion, absorption, and scattering, high power laser pulses are susceptible to a variety of nonlinear effects. These include nonlinear self-focusing and self-phase modulation. Numerical simulation codes exist to model these complex effects [43].

For the nonlinear case, equation 3.1 is modified by the inclusion of a source term:

$$\nabla^2 \vec{E} - \frac{1}{c^2} \frac{\partial^2 \vec{E}}{\partial t^2} = \vec{S} \tag{5.1}$$

where $\vec{S}$ is a source term, or terms, which are nonlinear in the laser electric field [42]. As before, we look for solutions of the form

$$\vec{E}(x, y, z, t) = A(x, y, z, t) \exp\left[i\psi(z, t)\right] \hat{x}/2 + c.c. \tag{5.2}$$

5.2.1 Nonlinear Self-Focusing

In nonlinear self-focusing, the index of refraction of the atmosphere is influenced by the intense electric field of the laser pulse. The index of refraction in any physical medium derives from the polarization of the medium in response to the optical electric field. For small optical fields, the polarization can be modeled by electrons moving in a harmonic potential. The polarization is linearly proportional to the applied field. This results in the ordinary, linear index of refraction.

However, for sufficiently intense optical fields the electrons are transported beyond the harmonic portion of the atomic potential. For centrosymmetric media

such as air, the lowest-order correction to the potential is quartic, which leads to a third-order nonlinearity in the polarization. That is, $P = \epsilon_0\left[\chi^{(1)}E + \chi^{(3)}E^3\right]$, where ϵ_0 is the permittivity of free space, and $\chi^{(1)}$ and $\chi^{(3)}$ are the first and third-order susceptibilities. This manifests as a local change in the index of refraction proportionate to the intensity of the laser beam:

$$n = n_0 + 2n_2 I \tag{5.3}$$

where n_0 is the linear index of refraction, I is the beam intensity, and $n_2 = \frac{3\chi^{(3)}}{4n_0}$ is the nonlinear index of refraction. The majority of materials, including air, have positive n_2 at optical wavelengths; that is, they exhibit increased index with increasing optical intensity. Therefore, beams with on-axis intensity maxima effectively create a traveling positive lens, which leads the beam to converge on itself. This process is known as nonlinear self-focusing [44]. For the laser pulses used in this work, a typical n_2 value for air is on the order of 5×10^{-19} cm^2/W.

The effect of nonlinear self-focusing can be included in the nonlinear wave equation by the use of the source term

$$S_{NSF} = \frac{\omega_0^2 n_0^2 n_2}{4\pi c} \left|A(x,y,z,t)\right|^2 A(x,y,z,t) \tag{5.4}$$

A "critical power" at which nonlinear self-focusing becomes experimentally significant can be defined by comparing the strength of nonlinear self-focusing to the defocusing strength of diffraction. Since the diffractive spreading angle θ_{diff} and the nonlinear self-focusing angle θ_{sf} both scale as R^2, the ratio depends not on the

intensity, but on the total beam power. The critical power, P_{crit}, is the power at which the ratio of diffraction to nonlinear self-focusing is 1. For a Gaussian beam, the critical power is given by [44]

$$P_{\text{crit}} = \frac{\pi(0.61)^2}{8}\frac{\lambda^2}{n_0 n_2} \tag{5.5}$$

Beams containing much less than one critical power experience diffraction and linear propagation. Beams which contain much greater than one critical power experience rapid self-focusing. Using $n_2 = 5 \times 10^{-19}$ cm^2/W and a wavelength of 800 nm, the theoretical critical power in air is found to be approximately 1.9 GW.

In practice, the power required to induce nonlinear self-focusing is often higher than the estimate provided by Equation 5.5. For instance, Braun *et al.* required 10 GW of power to initiate self-focusing, rather than the 1.8 GW predicted for their wavelength [46]. Similarly, Liu and Chin found the critical power for 800 nm laser pulses to vary from 10 GW for a 42 fs pulse, to 5 GW for pulses 200 fs and longer. [47] This is due to time-dependent contributions to the nonlinear refractive index resulting from the difference between atomic and molecular polarization times [44].

5.2.2 Filamentation and Self-Guiding

Laser pulses with very high intensities, on the order of 10^{13} W/cm^2, can ionize the air to form plasma filaments, in which nonlinear self-focusing is balanced by the combination of diffractive spreading and plasma defocusing [48]. These filaments can propagate many Rayleigh lengths in air at a spot size on the order of 100

microns, without appreciable change in the size of the beam [49,50]. Much research on the propagation of high power laser pulses has concentrated on the filamentation regime [51–53].

Even below the ionization threshold, the action of nonlinear self-focusing can overcome beam spreading due to diffraction [54]. For laser pulses with power equal to P_{crit}, self-focusing and diffraction balance one another. This persists for many Rayleigh lengths, until the delicate balance is upset, devolving into either eventual beam collapse or diffraction. In this self-guiding regime, the beam undergoes long-distance propagation without filamentation [44].

Although both plasma filaments and self-guiding laser beams can propagate many Rayleigh lengths, because the diameter of a filament is so much smaller than that of a self-guiding beam, the filament's Rayleigh length is correspondingly shorter. Thus, the absolute propagation distance which can be attained with self-guiding is longer than that of a filament [11]. Long distance propagation is necessary to reach the strong turbulence regime. For this reason, catastrophic beam collapse and plasma filamentation are to be avoided in order to explore the interplay of nonlinear self-focusing and strong turbulence. Plasma filamentation is often accompanied by the conversion of laser photons to supercontinuum light, spanning from the UV to the infrared [55]; the presence of this light can be used to diagnose and avoid the presence of plasma filaments during self-guiding propagation experiments.

5.2.3 Group Velocity Dispersion

Light propagating through a medium is subject to group velocity dispersion (GVD). Since the index of refraction of a physical medium in general varies with the frequency of light, different wavelengths of light propagate at different velocities. Consider a laser pulse with significant bandwidth; the duration of such a pulse changes as it propagates, as different frequency components lag behind others. This effect is GVD. The effects of GVD is especially significant for short laser pulses, such as those produced by CPA laser systems. The broad bandwidth of such pulses increases the absolute magnitude of the change in pulse length, while the short pulse length increases the relative significance of that change.

The change in pulse length due to group velocity dispersion is given by

$$\Delta T_{GVD} = d \times D(\lambda_0) \times \Delta\Lambda_0 \tag{5.6}$$

where d is the propagation distance, D is the group velocity dispersion coefficient (proportional to $\frac{\partial n}{\partial \lambda_0}$), and $\Delta\Lambda_0$ is the bandwidth of the laser. The value of D in air at 800 nm is $-0.062493 ps/(\text{nm} \times \text{km})$ [56].

In order to estimate the effect of GVD on the experiments presented in this work, the expected change in pulse length due to GVD has been calculated for each case. The two experiments discussed in this work were performed at propagation ranges at NRL (Chapter 6) and AFRL (Chapter 7).

For the NRL facility, the maximum propagation distance is 90 m and the bandwidth is 27 nm, based on a 35 fs transform-limited short pulse. The change in

pulse length ΔT is therefore $\sim$ 151 fs. Since the shortest pulse length used in that experiment is 1 ps, the fractional change due to GVD is at most 15%.

For the AFRL facility, the maximum propagation distance is 540 meters and the bandwidth is still 27 nm, based on a 35 fs transform-limited short pulse. The resulting value of ΔT is about 906 fs. Since the shortest pulse used at AFRL is about 900 fs long, the fractional change in pulse length is on the order of 100%. This amount of GVD could cause the short pulse to compress to its transform-limited pulse length of 35 fs as it propagates through the atmosphere, thereby greatly exceeding the critical power near the target. This effect is likely to be significant; however, at the time that experiments were performed, the diagnostics necessary to characterize the size of this effect were not in place. Future simulations of these or similar future experiments should include the effects of GVD in order to accurately model the propagation.

5.3 With Turbulence

As with low-power linear laser beams, the propagation of high-power laser pulses is complicated by the presence of turbulence. The generation and wander of plasma filaments in turbulence have been studied extensively [49, 57–59]. However, there has been relatively little study of nonlinear propagation through turbulence in the sub-filamentation regime ($P \sim P_{\mathrm{crit}}$). In a series of simulations, Hafizi *et al* found the effect of turbulence to be similar to reducing the beam quality of the laser pulse [60].

It is plausible to imagine that nonlinear self-focusing might be employed to resist turbulent spreading, just as it resists diffraction. In the case of weak turbulence an effective turbulent spreading angle θ_{turb} can be defined [27]. When $|\theta_{\text{sf}}| = |\theta_{\text{turb}}| + |\theta_{\text{diff}}|$, the strength of nonlinear self-focusing should balance the combined effects of turbulence and diffraction. Indeed, self-focusing has been observed in simulation to overcome turbulent spreading for sufficiently weak turbulence [59].

In strong turbulence the formation of self-reinforcing hot spots, seeded by turbulence-induced phase distortions and driven by nonlinear self-focusing, can lead to beam breakup. Turbulent fluctuations smaller than the size of the beam leads to the random formation of hot spots. These hot spots become self-reinforcing through nonlinear self-focusing and eventually lead to filamentation. The beam breaks up into a number of filaments approximately equal to the number of critical powers within the beam. The propagation of sub-ionization high power laser pulses in strong turbulence has been studied using Monte Carlo simulation to predict the probability of beam collapse as a function of turbulence strength and laser propagation distance [9].

Under certain conditions, however, beam breakup might be averted. Turbulent eddies smaller than the inner scale of turbulence are strongly dissipated by viscosity, leading index of refraction variations to experience fast falloff at sizes below the inner scale. For beams much smaller than the smallest turbulent eddy, index-induced phase errors should remain first-order across the beam. The effect of turbulence for such a scenario would be restricted to pointing fluctuations. In the case of linear laser propagation, any beam with initial spot size smaller than the inner scale will

rapidly diffract to a larger size, allowing turbulence to introduce higher-order phase errors. However, this may not be true in the case of a nonlinear self-channeling beam, which can maintain its size over long distances.

In fact, recent simulations performed at NRL have indicated that a high power laser pulse operating in the self-guiding regime might be capable of propagating through turbulence without undergoing turbulent spreading, so long as the beam size remains smaller than the inner scale of the turbulence [10, 11, 61, 62]. Beam images demonstrating several realizations of the simulated propagation of nonlinear self-channeling beams are presented in Figure 5.1. All beams begin the simulation at a radius smaller than the inner scale; those beams on the bottom row undergo nonlinear self-focusing, maintaining a small spot size even after propagation over a long distance.

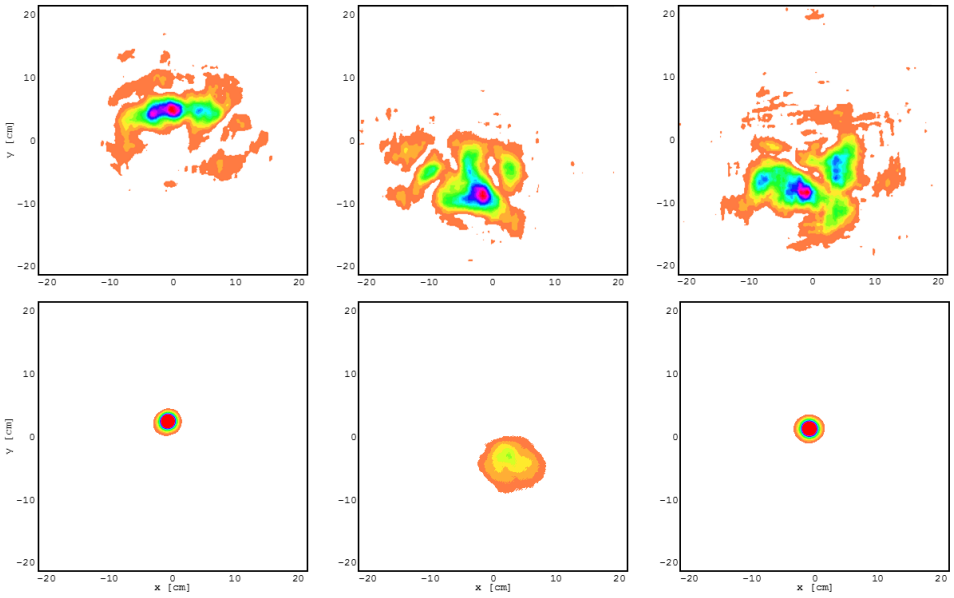

Figure 5.1: Computer simulations of sub-inner-scale low-power and high-power beam profiles after propagating through deep turbulence. Three realizations of turbulence are presented for both high and low power cases. Top row: low-power propagation with linear focusing to target. Bottom row: high-power propagation with nonlinear self-focusing. Simulation parameters: 7 km propagation distance, $C_n^2 = 10^{-15}\mathrm{m}^{-2/3}$, $\sigma_R^2 = 2$

Chapter 6: Experiments at NRL

6.1 Overview

Moderate-range nonlinear propagation experiments were performed at the U.S. Naval Research Laboratory (NRL), Plasma Physics Division (PPD). These experiments demonstrated NSC for the first time, over moderate range (> 10 m) and in moderate turbulence (Rytov ~ 0.3).

6.2 Outline of Methodology

6.2.1 Propagation Range

The Plasma Physics division at NRL is home to a moderate-distance indoor propagation range. This 30-meter range runs alongside a short-pulse laser system (described below) and through three labs, to a target table at the end of the building. High-power dielectric optics are available to reflect the beam across this range multiple times, reaching a total maximum propagation range of approximately 90 meters. Only the 30-meter path was used in these experiments. A schematic and photograph of the laboratory space are presented in Figure 6.1.

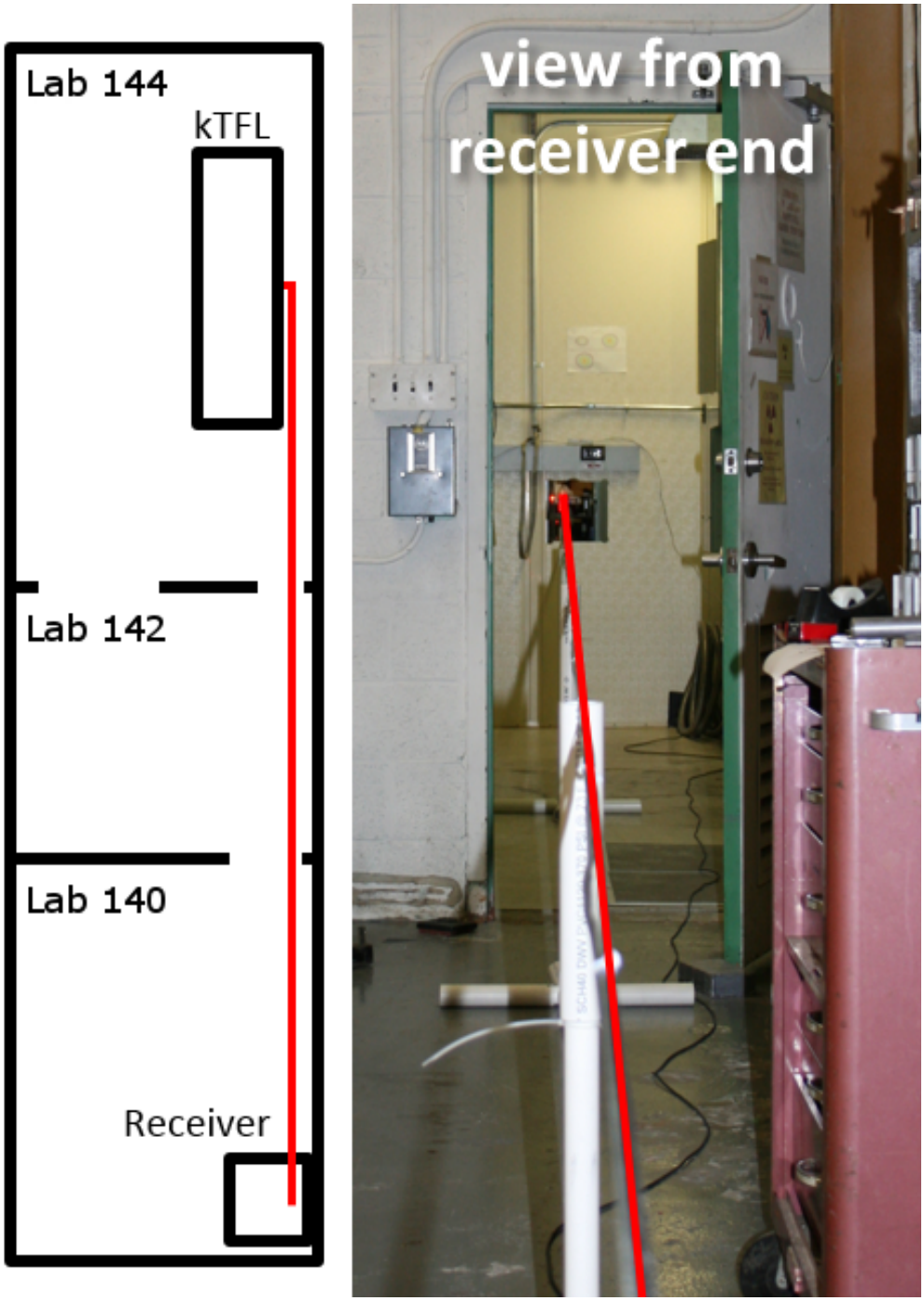

Figure 6.1: The moderate distance indoor laser propagation range at the NRL Plasma Physics Division.

6.2.2 Laser System

The laser used for this portion of the work is the kilohertz Titanium Femtosecond Laser (kTFL) at NRL PPD. kTFL is a cryogenically cooled 800 nm Titanium-doped sapphire laser (Ti:sapphire), delivering 20 mJ of energy per pulse at a pulse rate of 1 kHz. It uses chirped pulse amplification to reach a minimum pulse length of 35 fs, and thus a maximum peak power of 570 GW.

Chirped pulse amplification (CPA) is a technology for amplifying ultrashort, high peak power laser pulses [63, 64]. This technique has enabled the development of lasers with peak powers on the order of petawatts [65]. In this technique, the high bandwidth (10s of nm), low energy (hundreds of μJ), transform limited short pulse (as short as tens of fs) output of a mode-locked laser oscillator is used as a seed. If this pulse were amplified directly, nonlinear self-focusing of the resulting high power pulse would destroy the amplifier gain medium. Instead, the seed pulse is stretched temporally. This is done by introducing a frequency chirp which disperses the spectral content of the pulse in time, creating a long (100s of ps) chirped pulse. This chirped pulse is amplified, and then the chirp is removed, typically with a pair of diffraction gratings, to recompress the pulse. Because the final intense pulse is formed on the surface of a diffraction grating rather than within the bulk material of the gain medium, two main advantages are realized. First, the beam can be increased in size, reducing the peak laser intensity without the expense or pumping and cooling challenges of a large gain medium; second, the path-integrated $n_2 L$ is much reduced. Thus the risk of catastrophic self-focusing is reduced relative to

simply amplifying the original short pulse directly.

In addition to providing an ultrashort, high-power beam, CPA allows the pulse length of the beam to be varied. By adjusting the separation of the diffraction gratings which compress the pulse, the amplified beam can be recompressed incompletely, leading to a chirped high-power pulse with increased pulse length. By increasing the pulse length, the peak power of the beam is reduced.

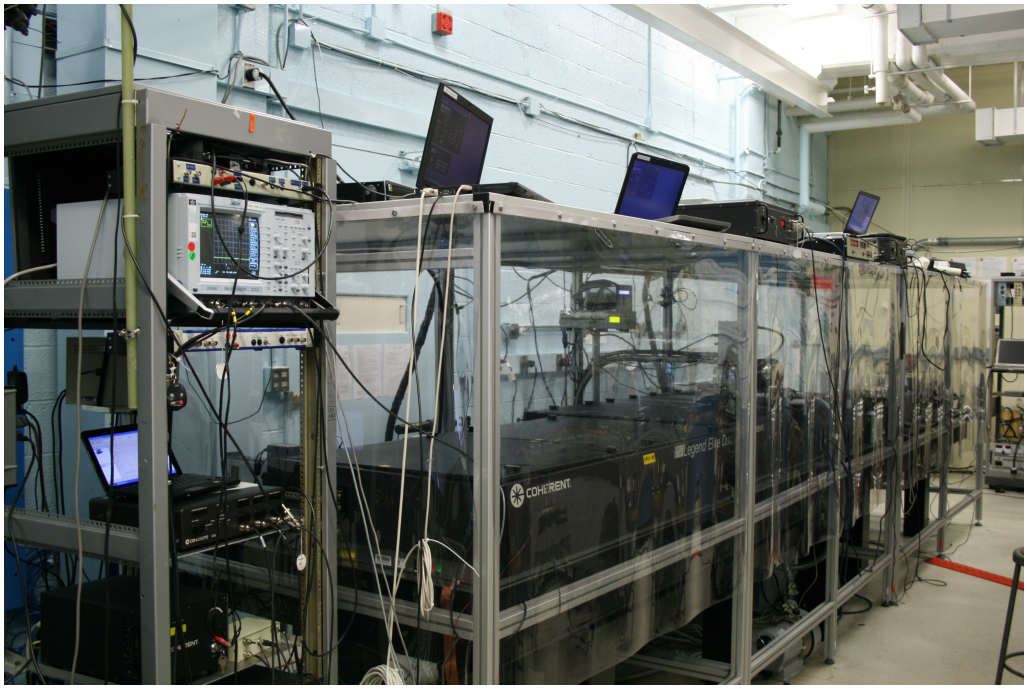

Figure 6.2: The kilohertz Titanium Femtosecond Laser at the NRL Plasma Physics Division.

The peak power output of CPA lasers such as kTFL is far in excess of what is needed for this research, since P/P_{crit} need only be on the order of 1. The CPA system allows kTFL's peak power to be tuned down from as much as 570 GW in order to access the range of interest ($\sim$2 GW).

6.2.3 Turbulence Generation

The GDFACT turbulence generator has been implemented over the 30 meter propagation range at NRL. The generator can be seen in the right-hand panel of Figure 6.1. The turbulence generated at NRL is similar to that produced at the AFRL site, with the exception of a higher baseline when the turbulence generator is turned off. This difference can be seen by comparing the lowest turbulence points of Figures 4.8 and 4.9; the baseline is approximately 10^{-14} at NRL, two orders of magnitude higher than the baseline of 10^{-16} measured at AFRL. This elevated turbulence background is due to the NRL propagation range's location along one side of an active laser lab, rather than in a dedicated hallway as at AFRL. The laser cooling systems and laboratory HVAC produce a good deal of air flow, which must remain running in order to keep the lasers in working order.

6.3 Results

6.3.1 First Observation of Nonlinear Self-Channeling

Preliminary high-power propagation experiments have been performed at the NRL Plasma Physics Division experimental site. These experiments consisted of a single pass over the 30 meter long turbulence generator. Both a high-power beam and a low-power beam were propagated through the same turbulence in order to compare the wander and spreading of the linear and nonlinear propagation.

For the nonlinear beam, the compressor was detuned to produce a high-power

pulse with $P \sim P_{\text{crit}}$. This was determined by slowly adjusting the compressor, decreasing the pulse length until the beam at the receiver was the same size as the beam at the transmitter. This indicated that nonlinear self-focusing was balancing diffraction. The linear beam was produced by blocking the seed beam before it enters kTFL's regenerative amplifier. The amplifier's self-lasing output has the same energy as the seeded beam; however, it is a much longer pulse.

At each turbulence generator setting, data was taken with both the high-power and the low-power beam. A sampling of pulses was captured by a Blackfly camera, and the resulting beam images were analyzed to yield spot size and beam wander statistics. Simultaneously, another Blackfly camera recorded data for a LISSD diagnostic based on a HeNe laser beam co-propagating with the infrared beam from kTFL.

Figure 6.3 plots the cumulative distribution functions (CDFs) for beam radius for both high- and low-power beams. The CDF for the low-power beam at the lowest turbulence setting is a nearly vertical line. This indicates that each pulse undergoes essentially the same propagation and produces essentially the same spot every time. As the turbulence increases, the random process of turbulence causes the beam to fluctuate. The low-power CDF becomes more sloped.

In contrast, the high-power beam has significant fluctuation in spot size even at the lowest values of turbulence. Nonlinear processes are sensitive to small fluctuations in initial conditions, so small changes in pulse energy or the small natural amount of turbulence are enough to cause the nonlinear beam to vary in spot size. However, this behavior is insensitive to the increase in turbulence. The CDF traces

remain essentially the same, even as turbulence increases to the maximum extent reached in these experiments.

Figure 6.4 summarizes the properties of the CDFs in Figure 6.3. For each CDF, the mean and standard deviation in spot size is plotted. The linear beam spot size fluctuations increase, while the statistics of the nonlinear beam remain constant.

This preliminary set of experiments also investigated beam wander. Figure 6.5 shows that the nonlinear and linear beams undergo essentially the same increase in wander as a function of turbulence. The nonlinear beam begins with a larger amount of wander than the linear beam does, once again due to the sensitivity of nonlinear propagation to small variations in initial conditions. However, both beams respond to turbulence by experiencing the same increase in wander.

These experiments act as a proof of concept for nonlinear guiding in turbulence, and motivated the work described in Chapter 7.

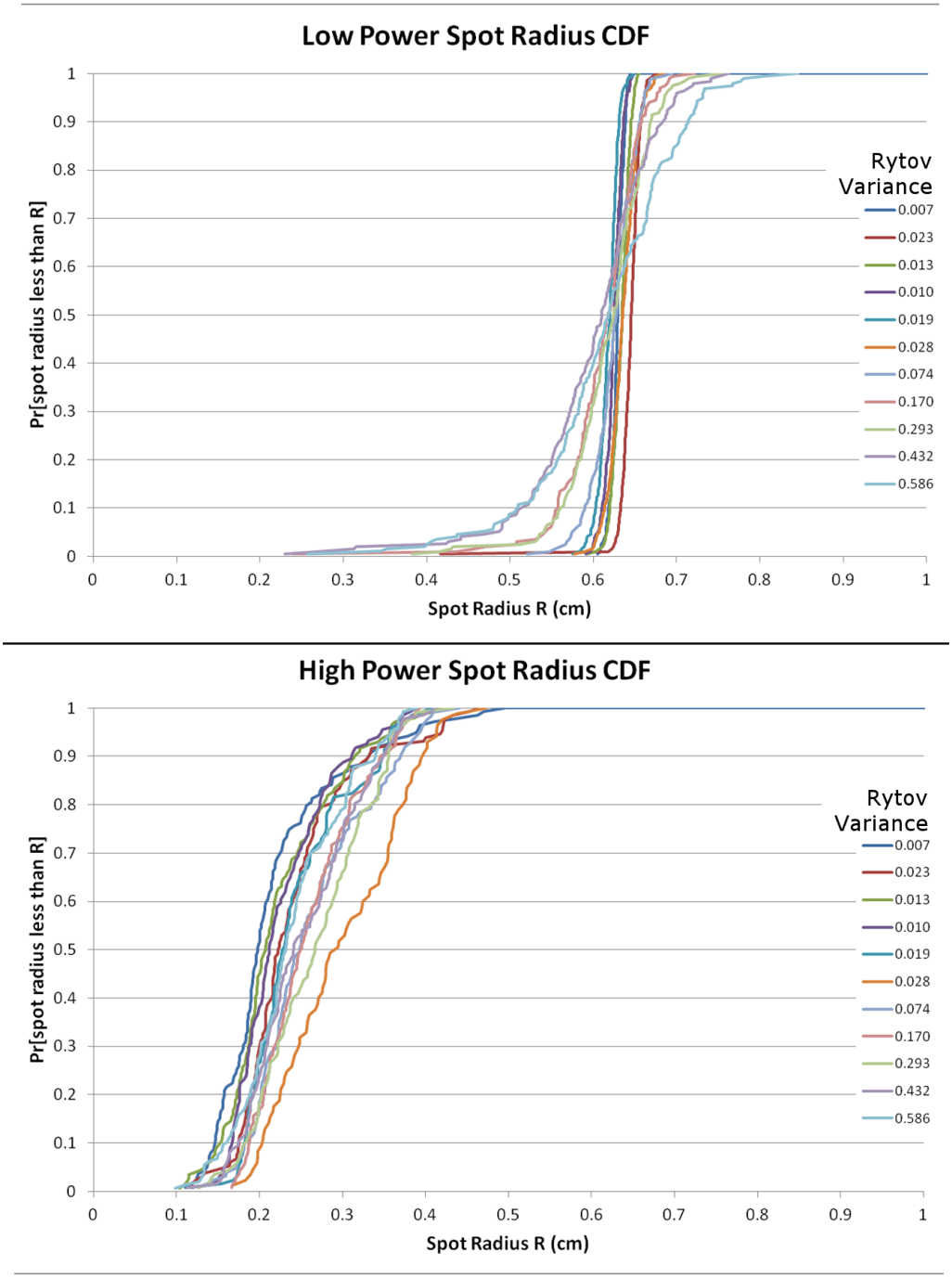

Figure 6.3: Cumulative distribution functions for the spot size of low-power and high-power beams propagating through turbulence at the NRL propagation range.

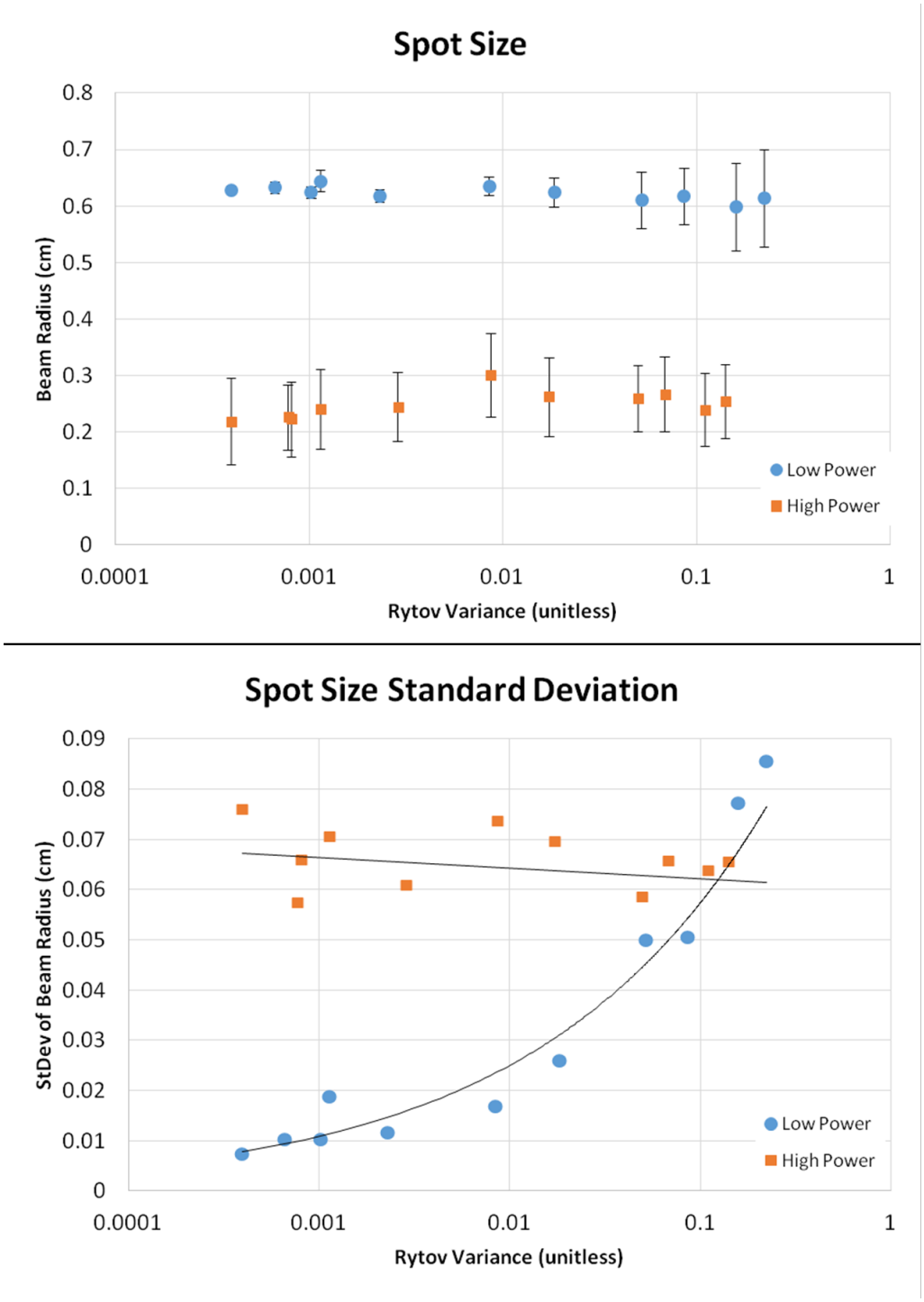

Figure 6.4: The standard deviation of the low-power beam size increases as a function of turbulence intensity. However, the high-power beam's statistics remain nearly unchanged as turbulence increases.

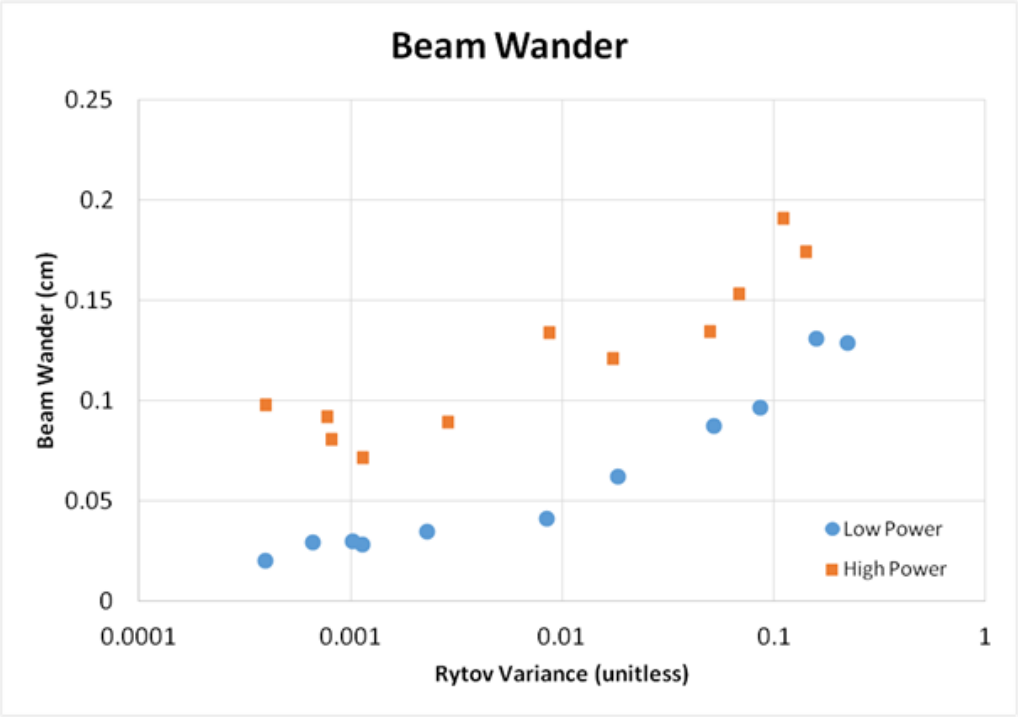

Figure 6.5: Increase of beam wander as a function of turbulence intensity. Both the low-power and high-power beam exhibit identical increases in beam wander, with the exception of a constant offset.

Chapter 7: Experiments at AFRL

7.1 Overview

Following the initial proof-of-concept work at NRL, long-range nonlinear propagation experiments were performed at the U.S. Air Force Research Laboratory (AFRL) in Albuquerque, New Mexico. These experiments demonstrated NSC over long range (> 100 m) and in deep turbulence (Rytov > 10).

7.2 Outline of Methodology

7.2.1 Propagation Range

AFRL is home to a long-distance indoor laser propagation range. This facility offers an uninterrupted indoor propagation length of up to 180 meters, with the option to perform multiple passes through the turbulent volume using dielectric mirrors. In these experiments, data was taken using either one or three passes down the range. The AFRL indoor range has excellent temperature stability, low humidity, and tightly controlled access for laser safety.

7.2.2 Laser System

Experiments were performed using the AFRL PHEENIX laser system. PHEENIX is a chirped-pulse amplification laser system operating at 800 nm, capable of producing up to 1.6 Joules per pulse at 10 Hz. The minimum pulse length is as short as 35 fs, for a peak power output of approximately 45 TW. This is far in excess of the power necessary for this experiment. Therefore, the final amplifiers were left turned off, reducing the output energy to approximately 20 mJ.

7.2.3 Turbulence Generation and Characterization

Artificial turbulence was generated using the convective flow artificial turbulence generator described in Chapter 3. A LISSD, as described in Chapter 2, was used to characterize the structure parameter C_n^2 and inner scale l_0 of turbulence produced by the generator. The Helium-Neon laser for the LISSD was aligned in order to provide the maximum overlap between the LISSD sample volume and the USPL propagation path without permitting cross-contamination between the two systems. A photograph of the HeNe beam propagating down the AFRL range is depicted in Figure 7.1. Implementation of the LISSD was improved relative to our prior efforts [66] by the use of a 12-bit monochrome camera as the imaging device.

Figure 7.1: Photograph of indoor turbulence range located at AFRL. The range is 180 meters long, and its ambient turbulence conditions have been characterized by LISSD and scintillometer. This view is looking backwards over the turbulence generator, from the receiver towards the transmitter. Forward-scattering light from the HeNe beam used for the LISSD can be seen due to aerosol scattering over the long path length.

7.2.4 Optical Setup

The PHEENIX laser system is located in a separate room, offset from the main propagation range. In order to produce a well-characterized and well-controlled beam at the entrance to the propagation range, the ~20 mJ uncompressed pulse from the PHEENIX laser was transmitted through a series of beam tubes to a "transmitter end" optical table immediately prior to the turbulence generator. This prevented undesired nonlinear self-focusing from occurring outside the region of controlled turbulence. The transmitter end table contained a spatial filter, pulse compressor, beam imaging system, spectrometer, LISSD laser, and alignment optics. The beam quality of the PHEENIX laser is imperfect, with Strehl ratio on the order

of 0.6. Therefore, a spatial filter on the transmitter table was used to clean the beam prior to compression. After the compressor, a variable aperture was placed to allow the higher-order modes at the perimeter of the beam to be clipped off, improving the beam quality at the cost of some energy.

The total amount of energy available after the spatial filter and compressor was as much as 13 mJ. For the single-pass runs, the amount of energy allowed through the aperture was 5 mJ. For the triple-pass runs, the aperture was opened to allow 11 mJ through.

The receiver table contained the LISSD diagnostic pinhole and camera, a Macor ceramic target board for the USPL beam, a USPL imaging camera directed at the Macor, and a photodiode to allow synchronization of the camera triggering with the laser pulse. The LISSD receiver and the USPL receiver were offset from one another by approximately 30 cm on center, with their placement reversed relative to the transmitter end; in this way the beams crossed midway down the propagation path to maximize the overlap. A dielectric mirror, transparent at 632.8 nm and highly reflective at 800 nm, was placed in front of the LISSD detector to prevent the nonlinear beam from affecting the statistics of the LISSD. A schematic diagram of the setup is presented in Figure 7.2.

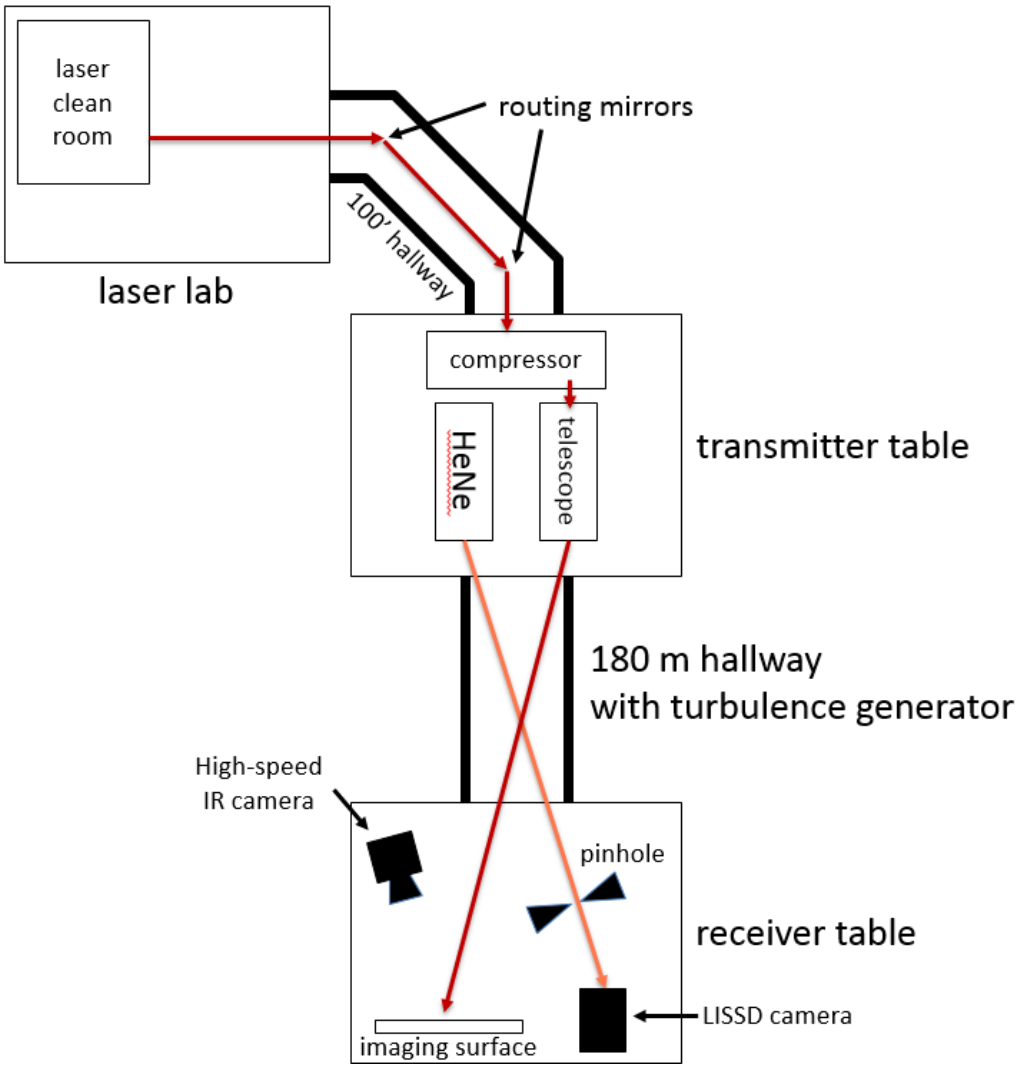

Figure 7.2: Diagram of experimental setup

7.2.5 Pulse Length and Power

Unlike at NRL, the PHEENIX laser cannot produce a longer pulse by relying on amplifier self-lasing. Therefore, two settings for the compressor grating separation were used, corresponding to a "high power" self-guiding case and a "low power" linear propagation case. The compressor spacing for the high power case was chosen by aligning the beam to the receiver table and adjusting the spacing until the smallest spot size was reached at the receiver. This corresponds to the desired self-channeling mode. For some compressor settings, catastrophic self-focusing and generation of plasma or supercontinuum light was visible at the target as a "hollow" beam profile or a pattern of rainbow light; these cases were intentionally avoided. For the low power case, the compressor was detuned to the limit of its travel.

Laser pulse length measurements were made with an autocorrelator at nominal grating positions of 0.408, 0.418, and 0.443 inches as measured on a translation stage. The autocorrelation traces, a typical example of which is displayed in Figure 7.3, indicate the presence of a short pulse containing very little energy, overlaid on a much longer pulse. The full-width-half-maximum pulse duration of the primary, higher energy pulse was measured to be 929 fs at a setting of 0.418 inches. However, the condition which resulted in the best self-channeling propagation was a nominal position of 0.429 inches. The pulse length at this grating position was not measured. However, it can be estimated.

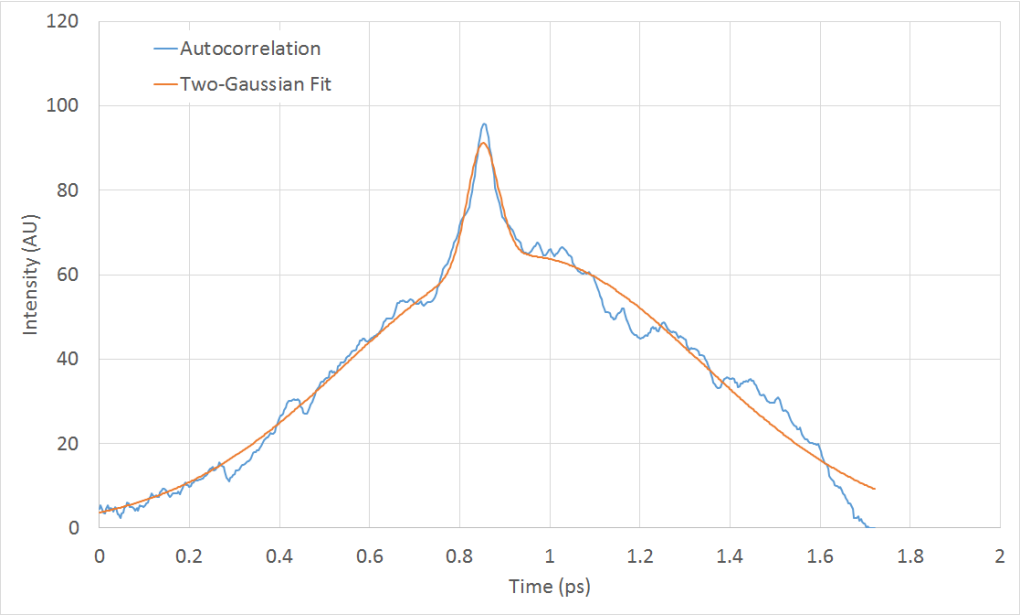

Figure 7.3: Autocorrelation trace of the short-pulse PHEENIX laser beam immediately prior to propagation down range. The nominal grating position is 0.418 inches.

For a first-order grating pair compressor detuned by a distance x from its ideal spacing, the pulse length is given by [45]

$$\tau_G = \tau_{G0}\sqrt{1+\left(\frac{x}{L_d}\right)^2} \tag{7.1}$$

where τ_{G0} is the minimum pulse length, L_d is the effective dispersion length $L_d = \frac{\pi c^2 d^2 \cos^2\beta}{\lambda^3}\tau_{G0}^2$, c is the speed of light, d is the grating line spacing, β is the central wavelength first-order diffraction angle, and λ is the laser central wavelength.

The PHEENIX compressor had a grating line density of 1500 lines per mm and a central wavelength first-order diffraction angle of 54 degrees. The minimum pulse length which can be produced by the PHEENIX laser is 35 fs. Solving Equation 7.1 with these parameters, the expected compressor position corresponding to a 35-fs pulse would be 0.526 inches.

The expected pulse length for the self-channeling condition is then found to be 835 fs. The low-power case was performed at a nominal grating position of 0 inches, for an expected pulse length of 4.51 ps. This pulse is too long to be measured on the autocorrelator.

A simple estimate of the peak power for the high power case (5 mJ / 835 fs) yields approximately 6 GW, approximately three times the nominal value of 1.9 GW cited in Chapter 5, and somewhat in excess of the typical experimental value of 5 GW [46, 47]. One possible explanation for the increased energy necessary to obtain self-focusing is the presence of some energy outside the self-channeling mode, in the shorter pulse visible in Figure 7.3.

Additionally, the critical power for self-focusing is calculated under the assumption of a Gaussian beam profile; any deviation from that profile will result in a greater diffractive spreading angle, and therefore a greater amount of power necessary to maintain self-focusing in balance with diffraction. The beam quality of the PHEENIX laser is non-ideal, as can be seen in Figure 7.4. For the single-pass data, the best beam at the receiver was produced by a beam whose wings had been significantly clipped by a final iris at the transmitter, resulting in a beam with a profile more similar to a top-hat profile than a Gaussian. For the triple-pass data, this iris was opened to increase the energy at the cost of allowing the asymmetric, nonuniform wings of the beam to propagate. Laser burns of these profiles are presented in Figure 7.4.

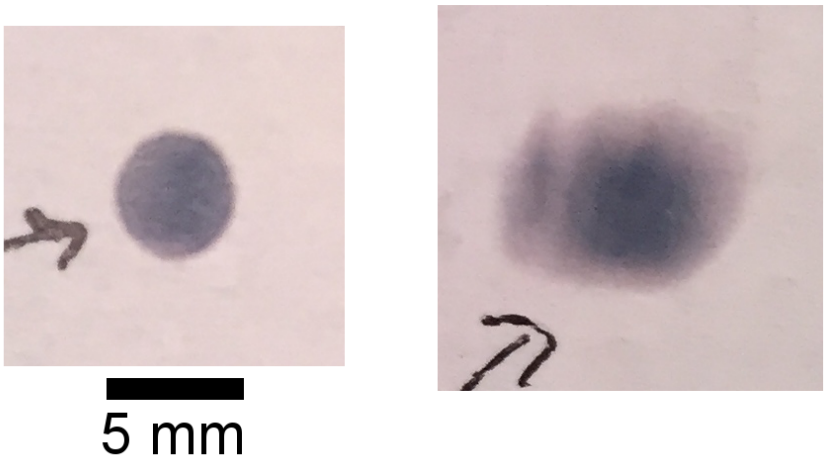

Figure 7.4: Laser burns taken after the final iris on the transmitter table. Left: beam used for single-pass experiments. Right: beam used for triple-pass experiments. The scale is the same for both images.

7.2.6 Data Organization

In order to capture the statistical fluctuations of turbulence, many images must be taken under each set of experimental conditions. For this experiment, a single "data shot" consists of a sequence of five hundred images of the USPL pulse on the Macor imaging surface, coupled with five hundred LISSD images of light from the HeNe, at a single setting of the turbulence generator. Although the number of images is the same for both beams and both diagnostics, the LISSD and USPL cameras are not synchronized. The LISSD camera runs at 30 fps, while the PHEENIX laser repetition rate is only 10 Hz. The LISSD images were taken while the USPL camera was running, so both sets of images should represent, statistically speaking, the same turbulence conditions.

The LISSD images were analyzed in order to yield statistics representative of the turbulence strength and inner scale. Since only the centroid location and total energy falling on the camera is necessary for this diagnostic, image analysis was simple. The background level of the image was determined by averaging over a region of the image far from the beam center, and this level was subtracted from the entire image. After that, the beam centroid and total pixel value integrated over the camera aperture were recorded. The fluctuations in these quantities were used to determine turbulence parameters according to the method laid out by Consortini [24].

Images taken by the USPL imaging camera were analyzed to yield statistics representative of the IR beam's behavior. In order to determine beam radius ac-

curately, significant image processing must be performed in order to minimize the effect of noise. Image analysis was carried out according to the procedure laid out in Appendix A. This procedure yields two ways of looking at the beam: whole-beam analysis, and hotspot analysis.

As outlined in the previous section, for each notional output pulse the PHEENIX laser actually produces a train of at least two pulses, only one of which is properly chirped in order to be compressed by the compressor gratings. Therefore, beam images taken at the target typically look like Figures 7.5 and 7.6, containing a central high-intensity spot from the pulse which undergoes nonlinear self-channeling, surrounded by lower-intensity light from the pulse or pulses which do not. For this reason, the hotspot data more accurately captures the effect of ideal nonlinear self-channeling than the whole-beam data does. However, the whole-beam analysis still represents the actual achieved results with this laser system. Therefore, results of applying both metrics to the image data have been retained, and are presented in the following sections.

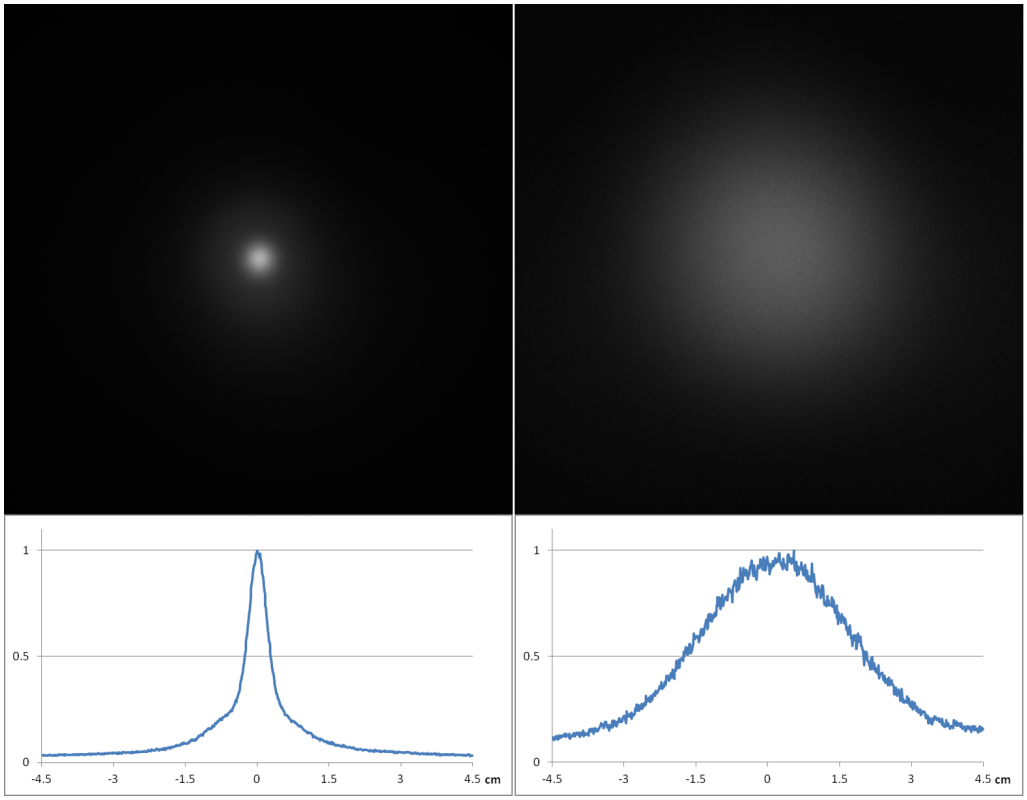

Figure 7.5: Instantaneous beam images taken at the receiver after one pass over the propagation range. Left side: high power propagation with nonlinear self focusing. Right side: low power linear propagation. Top panel: typical beam fluence profile at the receiver. Bottom panel: horizontal lineout across beam center. The presence of lower-power pre- and post-pulses can be seen in the "skirt" surrounding the self-channeling high power beam.

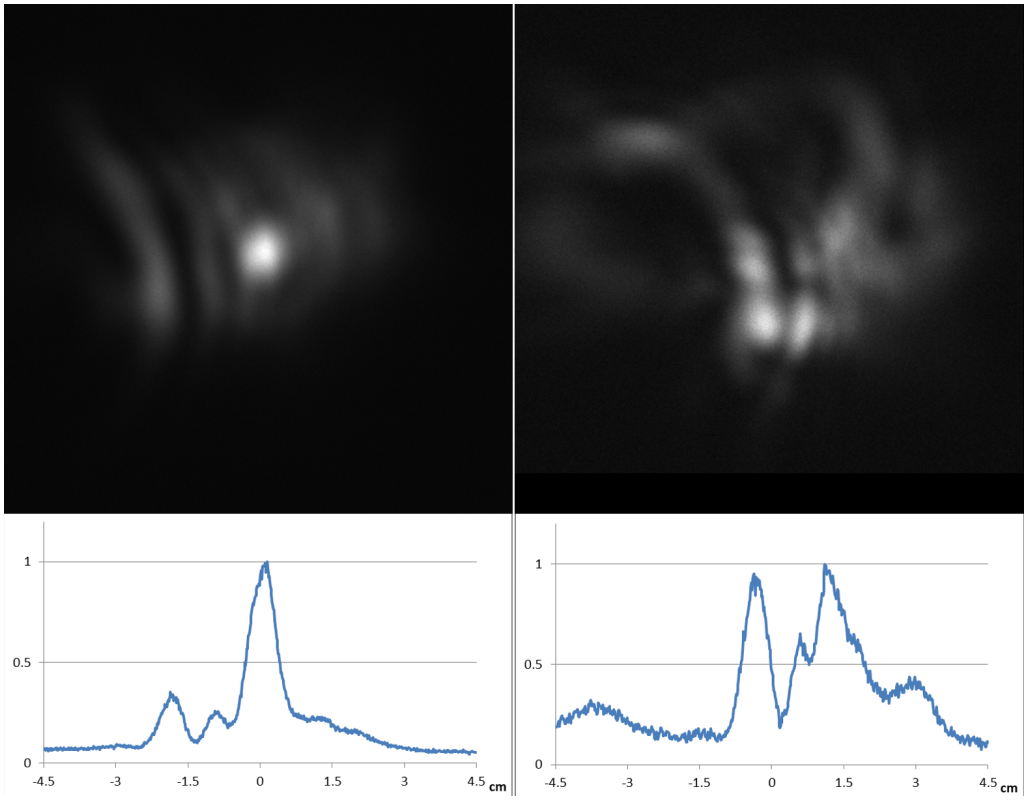

Figure 7.6: Instantaneous beam images taken at the receiver after three passes over the propagation range. Left side: high power propagation with nonlinear self focusing. Right side: low power linear propagation. Top panel: typical beam fluence profile at the receiver. Bottom panel: horizontal lineout across beam center. The distinction between the self-channeling portion of the beam and the lower-power pre- and post-pulses is even clearer.

Turbulence statistics collected for each shot included the structure parameter C_n^2 and inner scale length l_0. IR beam statistics included the beam centroid wander, the radius (given by $\sqrt{2}$ times the RMS radius), and the peak fluence. For each data shot, these statistics were compiled into a probability density function (PDF) describing the likelihood of any given outcome for a single laser shot under the given experimental conditions. Parameters varied included the laser power, turbulence intensity, and propagation distance.

7.2.7 Plotting and Theory Methodology

For each shot, the LISSD measures scintillation and angle-of-arrival fluctuations for the HeNe beam. The scintillation index is used to calculate C_n^2 according to Equation 3.23. The scintillation index and angle-of-arrival variation are combined according to Equation 2.18 to yield the inner scale. Next, the C_n^2 measured with the HeNe is used to calculate the Rytov variance for the IR beam according to Equation 3.12. Although this equation was developed under the assumption of weak turbulence, it remains the definition of the Rytov variance under all conditions, even though it no longer represents the scintillation index of any real beam. All other beam statistics are plotted as a function of the Rytov variance.

7.3 Results

7.3.1 Turbulence Generation

Turbulence was generated with the GDFACT, as outlined in previous sections. C_n^2 varied from 5×10^{-16} to 5×10^{-12}. LISSD measurements indicate that the inner scale of turbulence varied as a function of C_n^2, from a maximum of 2 cm with the GDFACT turned off, to a minimum of 5 mm at full power. The relationship between inner scale and C_n^2 is observed to be nearly linear on a log scale.

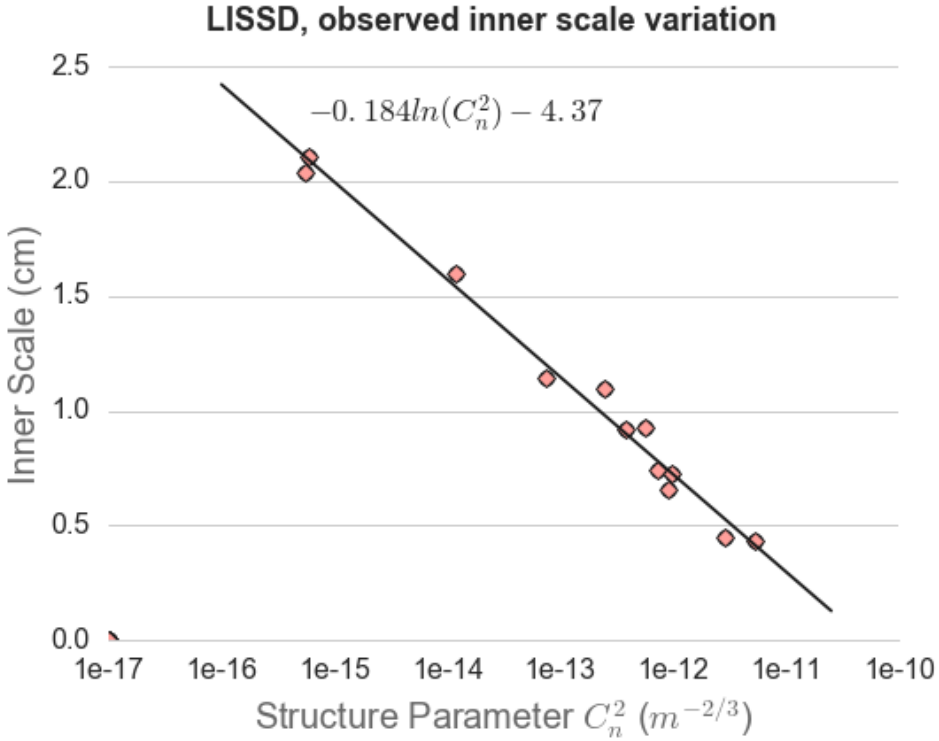

Figure 7.7: Inner scale of turbulence as a function of structure parameter C_n^2. A line of best fit and its generating equation are shown.

This relationship between C_n^2 and the inner scale is carried through the following analysis. Whenever the inner scale is called for in an equation, it is determined by reference to the line of best fit displayed in Figure 7.7.

7.3.2 Single-Pass Experiments

The results of the image processing are presented below. Figure 7.8 presents the beam wander as a function of turbulence. Wander is calculated as the standard deviation of the distance of the instantaneous beam centroid from its time-averaged location. This statistic is relatively insensitive to the method used to process the raw beam images: both hotspot and whole-beam processing result in the same centroid behavior. As expected, the beam wander is insensitive to changes in pulse length, and increases with increasing turbulence.

The black curve is the expected beam wander based on the expression for beam wander under conditions of strong turbulence, Equation 3.30. Nearly identical results are produced when using the weak-turbulence expression, Equation 3.14; this is represented by the dashed line. The free parameter for this curve was the intrinsic wander of the beam due to laser and platform fluctuations; it was set at 2.5 milliradians. The beam wander terms due to intrinsic wander and turbulence are statistically independent, and thus sum in quadrature. The resulting agreement between theory and experiment is observed to be excellent.

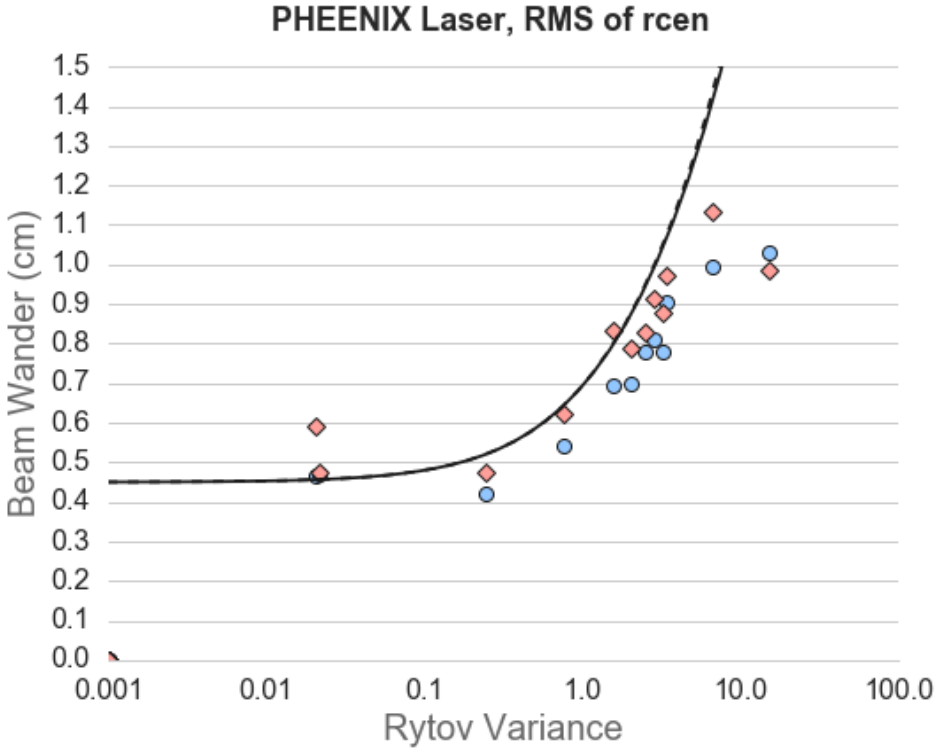

Figure 7.8: Beam wander (standard deviation of distance from time-averaged center) as a function of turbulence. Single-pass experiment (180 m).

From here on, analysis is presented in the following order: whole beam, hotspot, peak fluence. These represent successively increasing amounts of abstraction from what is actually observed in the experiment. Different readers of this thesis may prioritize different metrics. Those who are interested in the most direct report of what I observed with this laser in this experiment will wish to direct their attention to the whole beam data. Those readers who want to know how a more ideal beam (single short pulse) would behave, and those who are interested in creating a small spot after propagating a long distance, should look at the hotspot analysis. Those readers whose priority is the maximum fluence or intensity created on target should take note of the maximum fluence plots.

Figure 7.9 presents PDFs for the radius of the beam as a function of Rytov variance, in the form of a violin plot. A violin plot is similar to a box-and-whisker plot. However, instead of plotting summary statistics, such as the mean and interquartile range, the violin plot shows the entire PDF, oriented vertically, in a violin-like shape. There is one violin for each data shot, with the violin's horizontal position within the overall graph representing the turbulence conditions when the data was taken. Each violin is split into two halves: one for low-power, long-pulse data (blue), and one for high-power, short-pulse data (red). The width of the violin is proportional to the probability density, with each pair of violins (red and blue) in scale to one another, so that the integrated area under each violin is normalized to one. Each pair of violins is *not* in scale to the other pairs; all of them are set so that the violins have, as nearly as possible, the same width. This maintains the mutual legibility of all the violins, even if some PDFs are narrowly distributed and

others are very broad.

The solid black theory curve is based on the expression for the short-term beam radius under strong fluctuation conditions, Equation 3.29. The dashed curve is based on the equivalent weak-turbulence expression, Equation 3.19. There is one free parameter, set to the same value for both equations: the initial divergence of the laser beam, represented by quantity $F0$. For Figure 7.9, $F0$ was set to -17 meters. This likely represents a combination of imperfect adjustment of the collimating lens and imperfect laser beam quality.

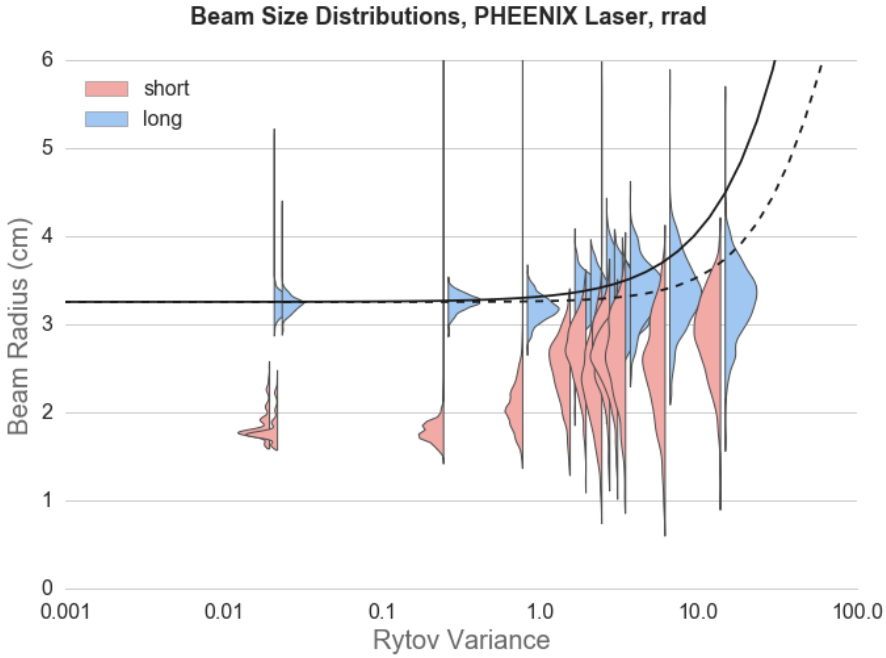

Figure 7.9: Violin plot for the short-term radius of the whole beam as a function of Rytov variance. Solid and dashed curves represent theoretical values for strong and weak turbulence, respectively.

For low turbulence, the low power beam is narrowly distributed about the ana-

lytical result for the expected beam size in the absence of turbulence. As turbulence increases, the variance of both the low-power and high-power distributions begins to increase. The mean radius for the low-power beam remains relatively constant, while the mean radius for the high-power beam begins to increase as self-channeling begins to fail. However, the high-power beam never grows as large as the low-power beam, even for Rytov over 10. As turbulence increases, the self-guiding beam statistics begin to resemble the low-power statistics more and more. However, under all conditions, the high-power beam remains more likely to produce a smaller spot than the low-power beam.

Analysis of the hotspot radius is presented in Figure 7.10. For low turbulence, the low power beam is narrowly distributed about the analytical result for its expected beam size in the absence of turbulence. As turbulence increases, the variance of both distributions begins to increase, while the mean remains relatively constant. As its variance increases, the low-power beam begins to have some probability of generating a small hotspot on target due to "lucky shots," in which turbulence sometimes acts as a positive lens over a sub-region of the beam [67]. However, the high power beam maintains a significant lump of probability mass at low radius which the low-power beam never matches.

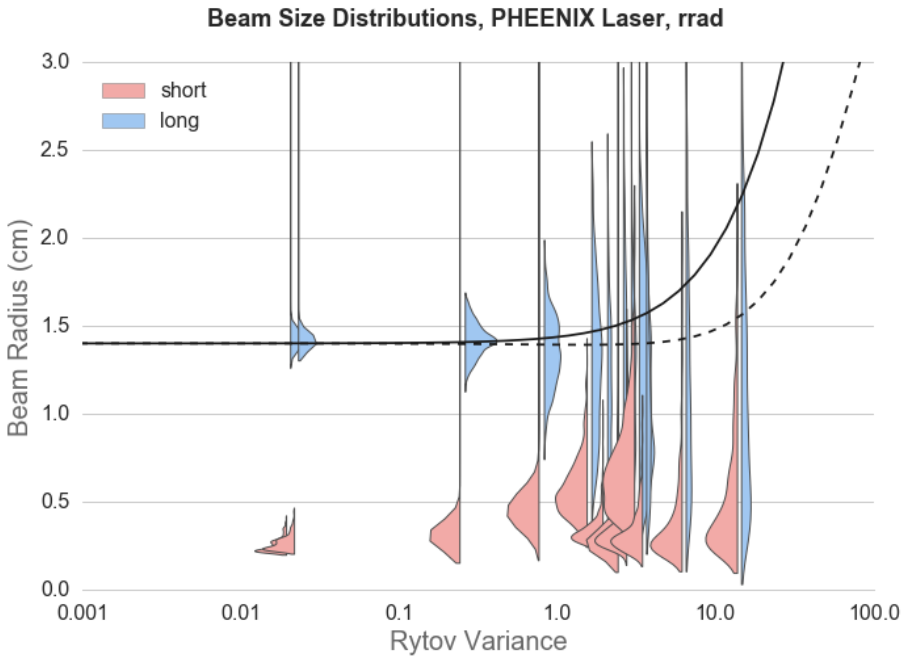

Figure 7.10: Violin plot for the short-term radius of the hotspot of the beam as a function of Rytov variance. Solid and dashed curves represent theoretical values for strong and weak turbulence, respectively.

The theory curves are once again based on Equations 3.29 (solid, strong) and 3.18 (dashed, weak). However, this time the free parameter $F0$ was set to -80 meters. Since the hot spot represents the propagation of a distinct mode of the beam, it comes as no surprise that it should have a different divergence from the low-quality beam as a whole. Additionally, the spot size predicted by theory has been reduced by a factor of $\sqrt{\frac{\log 2}{2}}$. This is the difference between the $\frac{1}{e^2}$ radius of a Gaussian beam and its radius at half maximum fluence. Since the hotspot size is calculated after performing a 50% threshold, this measure of beam size more accurately represents the quantity being measured.

Theory fails to predict the decrease in the mean radius of the hotspot of the low-power beam. This is likely a result of our definition of a "hot spot" and resulting image processing techniques. As turbulence increases, the scintillation index of the beam increases, leading to some pulses with increasingly intense hotspots. As the hotspot grows more intense, more of the wings of the beam fall below the fluence threshold necessary to count as part of the hotspot, and are therefore eliminated. This reduces the apparent radius.

The peak fluence on target was determined in arbitrary units by taking the maximum pixel value in the image, adjusted for background noise, camera gain, and the presence of attenuating filters in front of the camera. This statistic does not vary based on whether the whole beam or the hotspot is considered, since the entire difference between those two methods lies in the low-value pixels.

Under this metric, increasing turbulence actually increases the likelihood that the beam will produce high fluence. As turbulence increases, lucky shots focus part

of the beam and allow it to produce fluences that would not otherwise be possible. At the highest turbulence levels, the low-power and high-power beams exhibit nearly identical peak fluence statistics. Nevertheless, for any given peak fluence (in units of J/m^2), the peak intensity (in W/cm^2) is still far higher for the high-power beam, since its pulse length is much shorter than for the low-power beam.

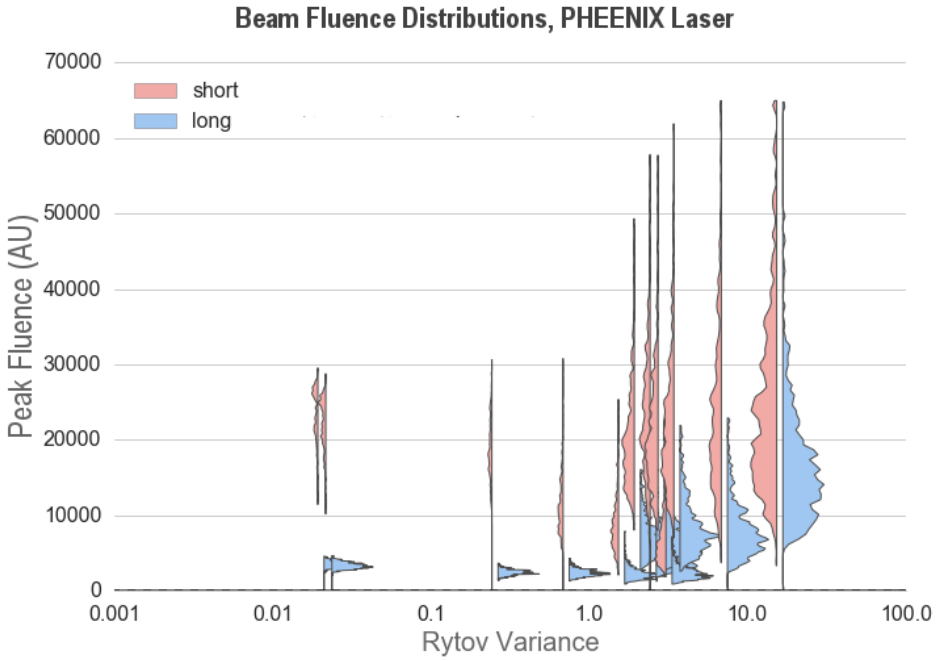

Figure 7.11: Violin plot for the maximum fluence on target as a function of turbulence intensity.

For each of these metrics, a convenient way to summarize the data is to ask the question: how much statistical benefit does the high power beam provide? If we were to randomly select one realization from both the high-power and low-power probability distributions, what is the probability that the high-power beam would

outperform the low-power beam? This probability can be computed by

$$\Pr[R(h) < R(l)] = \frac{\sum_{n=0}^{N} \sum_{m=0}^{M} H\left(R_m(h) - R_n(l)\right)}{M \times N} \tag{7.2}$$

where $R(h)$ and $R(l)$ are the radii of beams randomly selected from the samples of high-power and low-power data sets, $R_m(h)$ and $R_n(l)$ are the n^{th} and m^{th} samples in the high-power and low-power beam radius data sets, M and N are the total number of samples in the high-power and low-power data sets, and H is the Heaviside step function, equal to zero when its argument is negative and one when its argument is positive.

If both distributions were the same, the probability of improvement would be 50%. A similar statistic can be calculated for the probability that the high power beam will produce a higher peak fluence than the low-power beam, by replacing the radius with the peak fluence and interchanging h and l. These probabilities have been calculated for all three metrics; they are plotted in Figure 7.12.

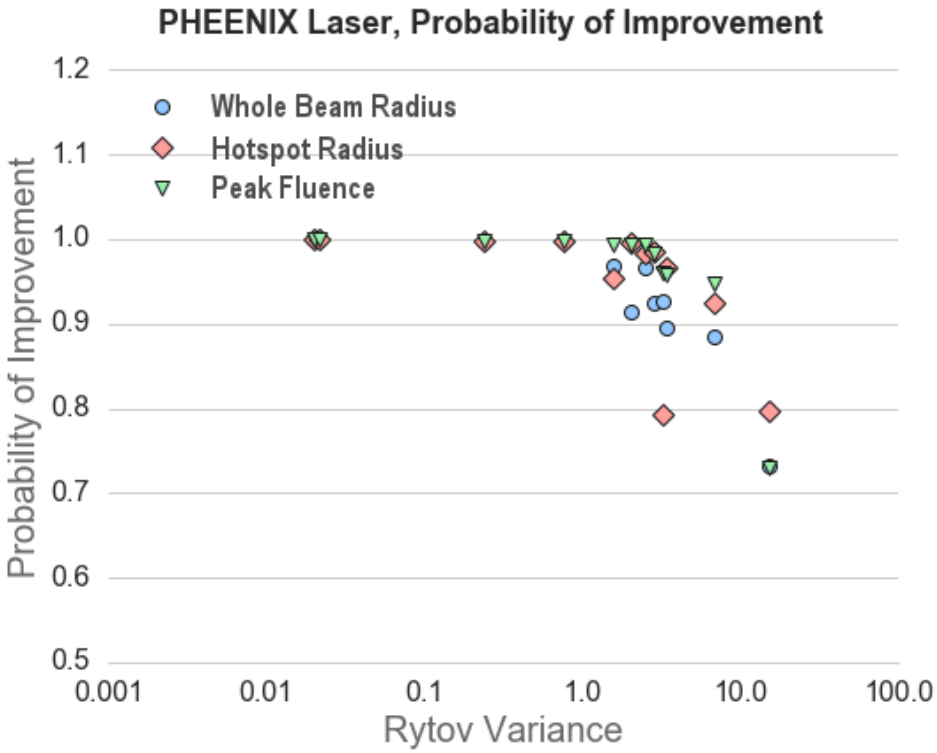

Figure 7.12: Probability of improvement as a function of Rytov variance.

Interestingly, the behavior of all three metrics is very similar. With the exception of a few outliers, each data set exhibits a gradual decrease in the benefit of nonlinear self-channeling as the Rytov variance increases. The roll-off begins at $\sigma_R^2 \sim 1$. For the strongest turbulence tested, $\sigma_R^2 \sim 10$, the probability of improvement due to nonlinear self-channeling is reduced to approximately 75%.

Another interesting way to look at this is in light of the inner scale. The data points in Figure 7.13 have the same y-coordinates as Figure 7.12, but the x-axis has been replaced with the ratio of the beam diameter to the inner scale. The qualitative behavior remains the same: all of the metrics exhibit similar roll-off as turbulence increases. However, now the decrease in improvement is very modest until the ratio of beam diameter to inner scale approaches one, at which point it drops precipitously. This validates the expectation that nonlinear self-channeling would cease to be effective for beams larger than the inner scale of turbulence.

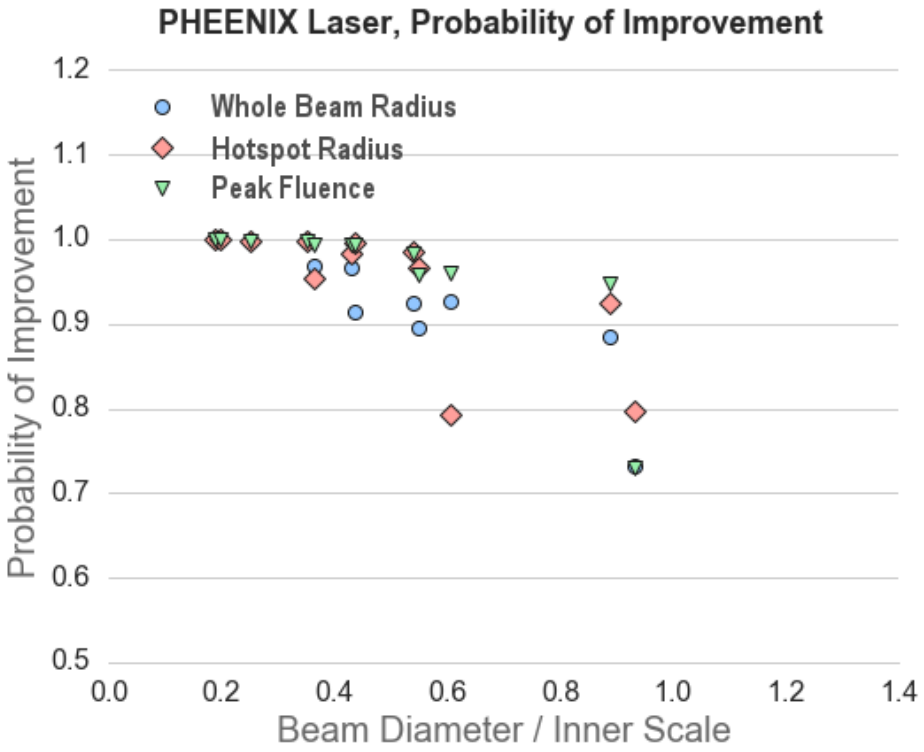

Figure 7.13: Probability of improvement as a function of the ratio of the initial beam radius to the inner scale.

7.3.3 Triple Pass Data

The experiments reported in the previous section were repeated, this time with three passes over the experimental range. High-reflectance mirrors were set up at both ends of the range, so that the IR beam could bounce back and forth. This enabled a total range of 540 meters. In order to reduce the risk of saturating the LISSD detector, the LISSD was left set up over only one pass. Although the optical turbulence (in terms of σ_R^2) is much stronger over a longer distance, the atmospheric turbulence (in terms of C_n^2) is the same. Therefore, measurements taken with the LISSD over one pass can be used to determine the Rytov variance over three passes, by scaling according to Equation 3.12.

Figure 7.14 presents the beam wander as a function of turbulence, as in Figure 7.8. Again, the beam wander is observed to be insensitive to pulse length. The theory curve is once again calculated from Equation 3.30, with intrinsic wander set at 2.5 milliradians. However, over this distance the agreement between theory and experiment is very poor.

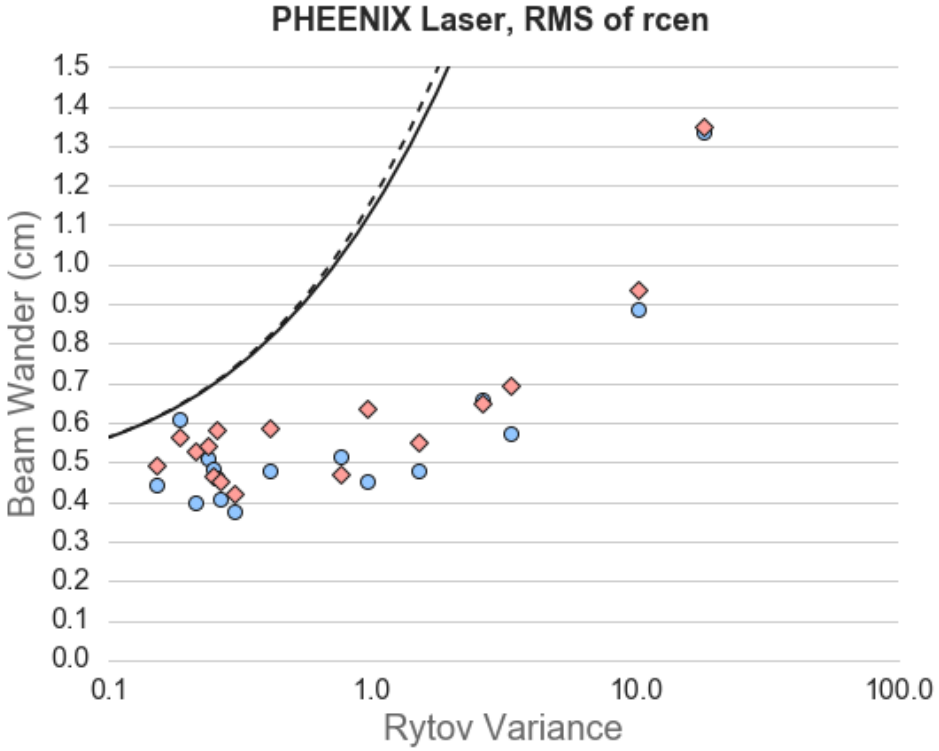

Figure 7.14: Beam wander (standard deviation of distance from time-averaged center) as a function of turbulence. Triple-pass experiment (540 m).

Even allowing the intrinsic wander to vary from the value used over 180 meters, the theory still reliably predicts an amount of wander far greater than observed. A possible explanation for this is that the IR beam, in being reflected down the propagation path multiple times, may have strayed outside the bounds of the turbulent region created by the GDFACT. In this case, the increased wander (and, as we shall see, beam size) would result almost entirely from the additional diffractive propagation through non-turbulent air. This would explain a persistent overestimate of wander and beam size by theory.

In this section analysis is presented in the same order as last time: whole beam, hotspot, peak fluence.

Figure 7.15 presents PDFs for the radius of the beam as a function of Rytov variance. The violin plots in this section represent a subset of the data actually collected: the full data set is too dense to read at low Rytov variance and has therefore been downsampled for clarity. As in Figure 7.9, the solid and dashed curves represent theoretical calculations for the expected short-term beam radius based on strong and weak turbulence theory, respectively. The free focusing parameter F_0 was set to 540 m to produce these curves. The low-turbulence curve temporarily decreases below the vacuum result; this behavior illustrates the danger of using low-turbulence theory outside its regime of applicability.

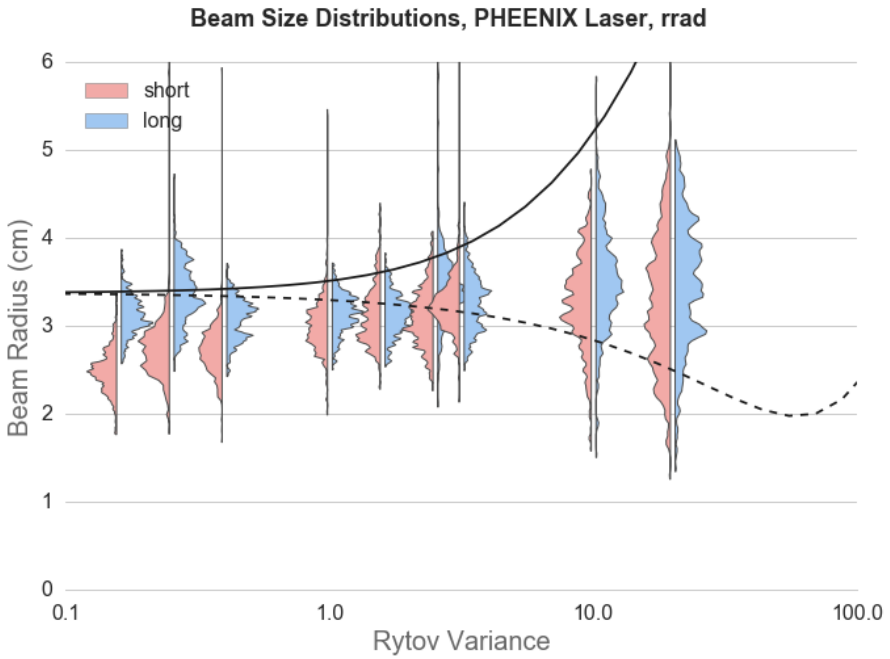

Figure 7.15: Violin plot for the radius of the whole beam as a function of Rytov variance. The dashed curve represents the weak-turbulence theory result; the solid curve the strong-turbulence result.

At low turbulence, the low power beam is distributed about the analytical result for its expected beam size. As turbulence increases, both distributions broaden and the mean spot size of both distributions increases. However, the mean spot size of the high-power beam increases faster, until by $\sigma_R^2 \sim 1$ the distributions are very similar.

The behavior of the hotspot radius is given in Figure 7.16. As before, the beam radii for the theory curves are reduced by a factor of $\sqrt{\frac{\log 2}{2}}$ to represent the effect of thresholding. The focal length for this case was again 540 meters.

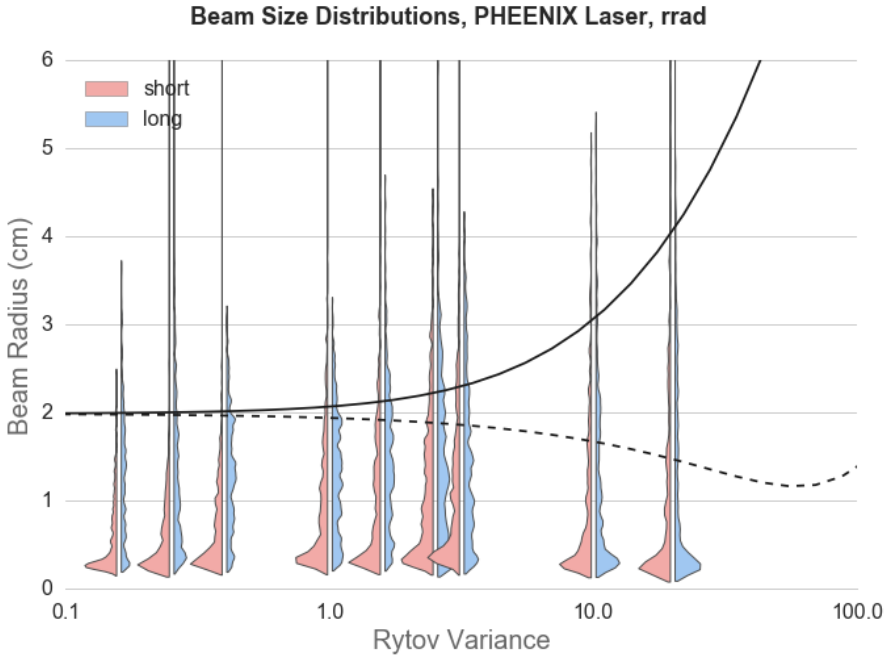

Figure 7.16: Violin plot for the radius of the instantaneous beam hotspot as a function of Rytov variance. For low turbulence, the high power beam has a lump of probability mass at low radius which the low-power beam does not possess. However, as turbulence increases, the chances that a lucky shot will form a small region of high fluence on the target increase, and the low-power beam begins to develop a similar feature. By $\sigma_R^2 \sim 3$ the distributions are very similar.

Examining Figure 7.16, the statistics of the high-power beam are seen to be insensitive to the effects of turbulence. However, high turbulence increasingly produces lucky shots which allow the low-power beam to produce statistics similar to that of the high-power beam. By a Rytov variance of approximately 10, the distributions appear nearly identical.

Examining the maximum fluence, rather than the spot size, the results look somewhat more favorable for the high-power beam. Although the low-power beam experiences lucky shots which increase its maximum possible fluence, the high-power beam nevertheless continues to produce fluences which the low-power beam cannot achieve. When the increased peak intensity due to the high-power beam's shorter pulse length is taken into account, this gap increases further. These results are presented in Figure 7.17

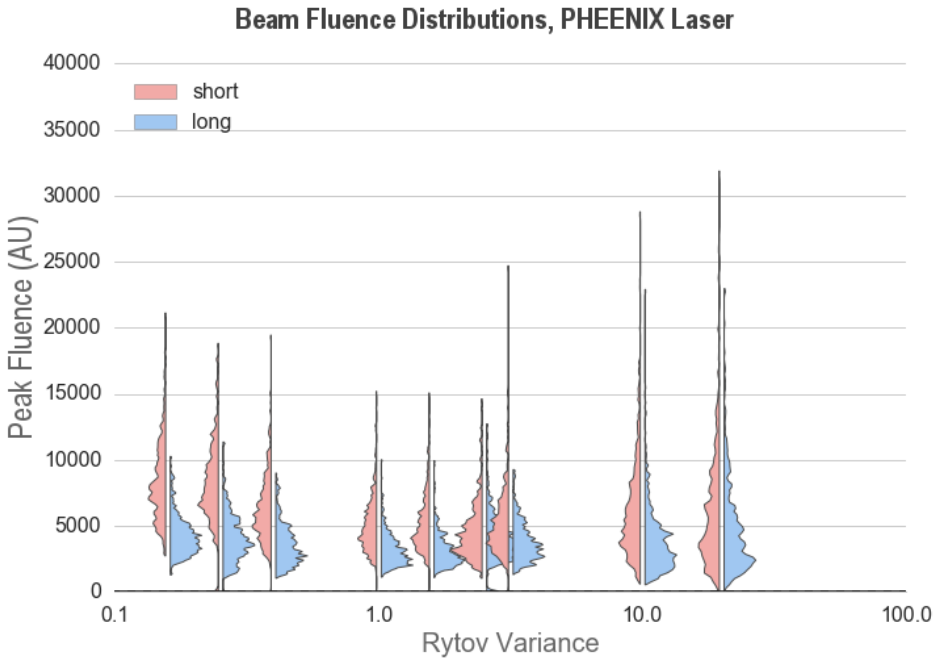

Figure 7.17: Violin plot for the maximum fluence on target as a function of Rytov variance. At all turbulence intensities, the high-power beam is capable of producing higher fluence on target than the low-power beam. The strength of this effect is diminished somewhat as turbulence increases, but never goes away.

Once again, it is instructive to examine the probability of improvement in each of these metrics realized by moving from the linear propagation regime of a low-power beam to the NSC regime. If both statistical distributions were the same, the probability of improvement would be 50%. A probability less than 50% indicates that the high-power beam underperformed the low-power beam. The results for the triple-pass experiment are summarized in Figure 7.18.

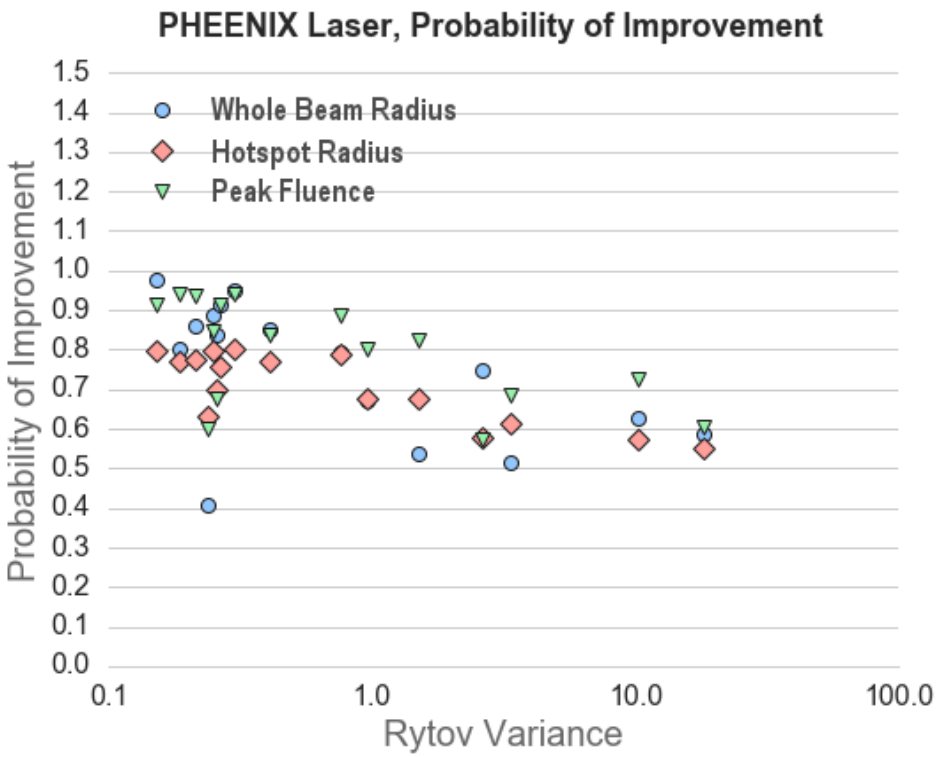

Figure 7.18: Probability of improvement for the triple-pass experiment. For Rytov variances near 10, all three metrics are found to approach parity with the low-power case.

The probability of improvement for all three metrics decreases approximately linearly with increasing log Rytov variance. Unlike the case for the single-pass, there

is a quantitative difference between the metrics: the probability of improvement for the hotspot radius is lower than that for the whole beam or the peak fluence for all values of turbulence. Additionally, nearly the entire benefit of the high-power beam is eroded by the highest turbulence values.

7.3.4 Both Single and Triple Pass

In applications which require a small spot on target, the baseline competition to a nonlinear self-channeling beam is a linear beam which begins with a very large radius and focuses linearly to the target. The nonlinear beam starts small, and uses nonlinear self-focusing to fight diffraction and stay small. It might be argued that a sufficiently large linear beam would not need to fight diffraction, and might outperform NSC so long as turbulence is not too intense. That argument is addressed in Figure 7.19. The short-term spot size statistics for the whole beam, in both single- and triple-pass experiments, are compared to the theoretical result from Equation 3.29 for the case of an infinitely large beam with focal length equal to the propagation distance.

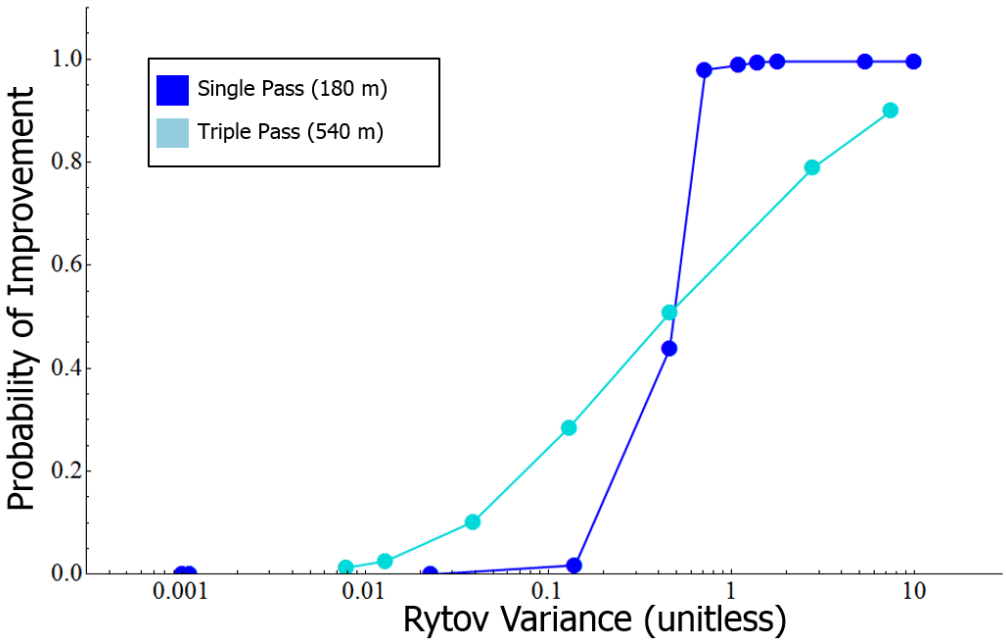

Figure 7.19: The probability that the NSC beam will produce a spot with radius smaller than the average radius of a low-power beam focused to the target from an infinitely large beam director. The performance of the infinite-radius linear beam was estimated using Equation 3.29. Nonlinear self-channeling starts to outperform the ideal linear case around $\sigma_R^2 \approx 0.5$.

7.3.5 Effects of Power and Beam Clipping

Additionally, experiments were performed to examine the statistics of the high-power beam at the target (single pass) as the initial beam power is allowed to vary. By fixing the turbulence at its highest strength and varying the compressor grating separation, the beam behavior as a function of power can be investigated with greater fidelity than simply comparing the low-power and high-power cases. The results of this experiment are plotted in 7.20

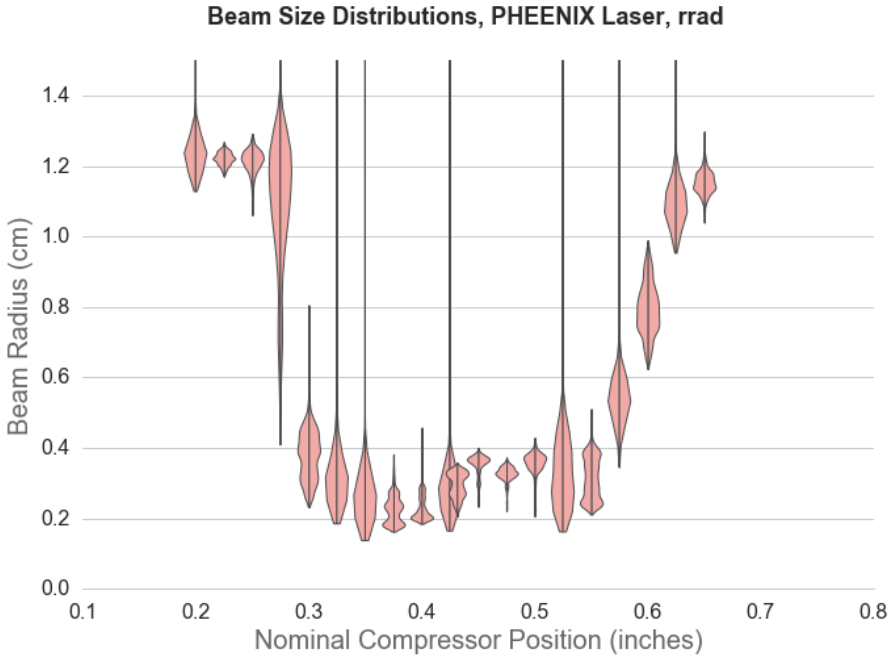

Figure 7.20: Average beam size as a function of power.

Chapter 8: Conclusion

8.1 Future Work

The present work provides experimental confirmation of the ability of NSC to produce small laser spots at long ranges, even in deep turbulence. Additional work to model and simulate the experiments performed at AFRL would enhance understanding of these processes. Special attention should be paid to the effect of GVD, since it has been shown to have an effect on the order of 100% of the pulse length over a range of 580 meters.

Future experimental work should be performed at longer range, in order to allow atmospheric scattering and absorption to come into play. These are expected to be important effects which will have to be balanced in order to maintain NSC over long distances. For instance, Peñano *et al* use a chirped pulse which compresses due to GVD to balance the loss of energy due to attenuation and maintain NSC [11].

Future experiments should use a new, improved version of the GDFACT, which was developed after the AFRL experiments took place. The "Lemmy" design is effectively multiple GDFACT devices in parallel with one another, suspended side-by-side with small ($\sim$ 1 inch) gaps between the wires. This design provides a wider zone of turbulence in which the beam can propagate, potentially allowing multiple

passes over the same range without the beam exiting the turbulent volume, as it may have done at AFRL. Additionally, as the linear beam propagates longer distances it will naturally diffract to larger size; the turbulent volume needs to remain at least as wide as the beam in order to correctly emulate natural atmospheric turbulence.

8.2 Conclusion

Nonlinear self-channeling, a novel mode of propagation for high power laser pulses, has been experimentally demonstrated in the presence of artificially generated atmospheric turbulence. In nonlinear self-channeling, the laser spot size remains approximately constant as a function of propagation distance, at a size somewhat smaller than the inner scale of turbulence. Beams propagating in this regime are resistant to the beam-spreading effects of turbulence, although their wander still increases in accord with linear theory. Examining Figures 7.12 and 7.13, the benefits of nonlinear self-channeling begin to decline as turbulence enters the strong turbulence regime ($\sigma_R^2 > 1$), and are largely eliminated once the inner scale becomes smaller than the beam radius. Under these extreme conditions, the high-power beam still has some likelihood of producing a small beam on target, but it is no more likely to do so than a linear beam of the same diameter. Nevertheless, it is still expected to out-perform an extremely large beam which is focused to the target (Figure 7.19). With these caveats, nonlinear self-channeling beams have potential value in any application which demands the propagation of laser light through the atmosphere to produce a high fluence or high intensity at long range.

Appendix A: Image Analysis

A.1 Approach to Analysis of Beam Profile Images

Images taken during the experimental portion of this work were analyzed in order to extract statistical quantities such as laser spot size, position, and peak intensity. A custom script written in Python was used for this purpose. Python was chosen for its execution speed, array of applicable pre-programmed modules, and extensive online tutorials.

Analysis begins with one of the roughly 500 images of the IR beam taken for each set of experimental conditions. These images range from 512x512 to 2560x2048 pixels in size, with 12-bit grayscale depth padded to a 16-bit image. The total volume of data is approximately 2.5 TB. Each image shows the beam profile of a single laser pulse at the end of propagation. Depending on experimental conditions, the signal-to-noise ratio of the image could be as high as several thousand, or as low as two. The beam could be large or small, tightly localized or diffuse, or spread out into multiple sub-beams. A single image analysis routine is needed which can convert all of these images into summary statistics, such as beam size and position, for comparison to theory and simulation.

An example of a typical beam image is shown in Figure A.1. The results of

applying successive steps of the analysis routine to this same example image will be presented in successive figures.

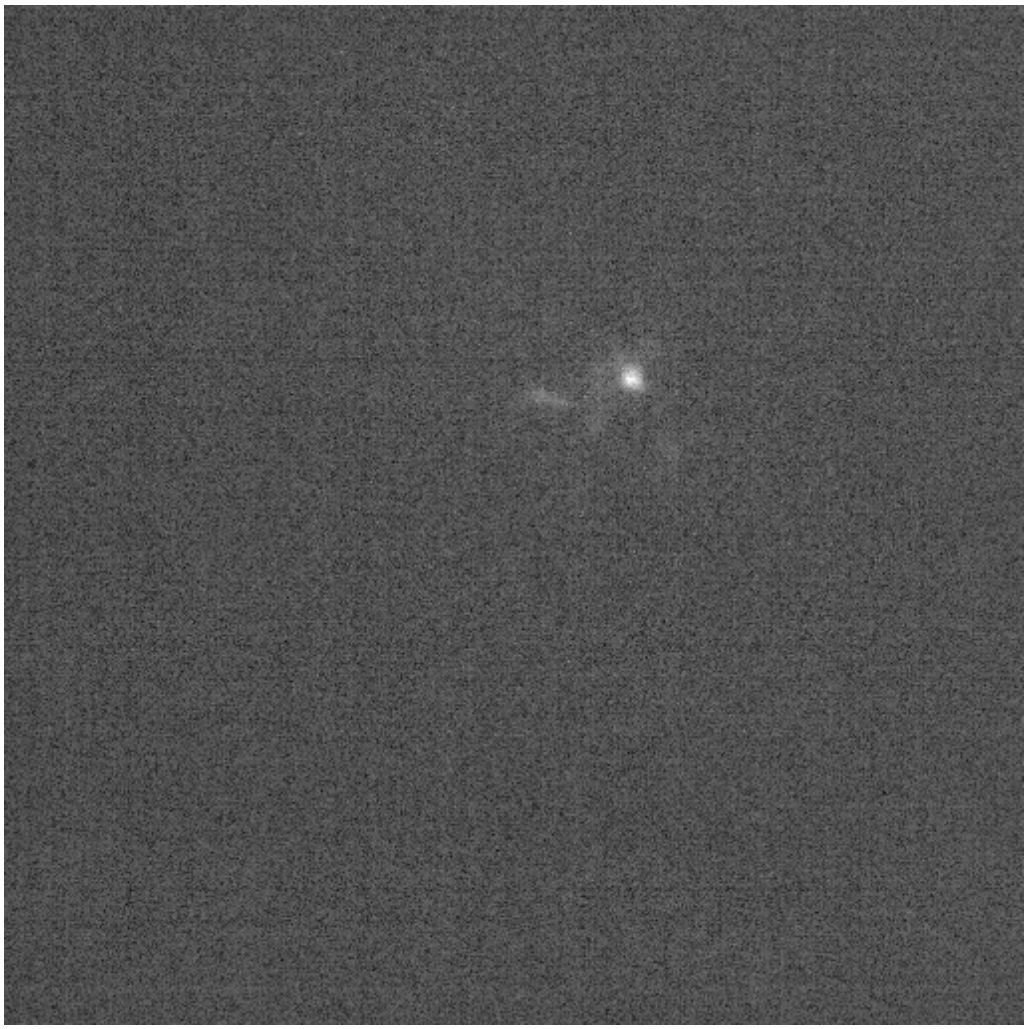

Figure A.1: An example unmodified image. Note the presence of significant "static-like" background noise.

The perspective of the image is corrected by means of a perspective transformation. During data collection, the camera is offset from the surface normal of the imaging plane in order to allow the laser beam to pass by, causing the flat rectangle of the imaging surface to appear as a trapezium. Collection of a wide-angle "setup"

image establishes the coordinates of the four corners of the imaging surface in both real space and image space. A perspective transform uses these known points to map every point in image space to the appropriate point in real space, producing a rectangular image showing the imaging surface as it would have appeared were the camera centered. The results of this procedure are shown in Figure A.2.

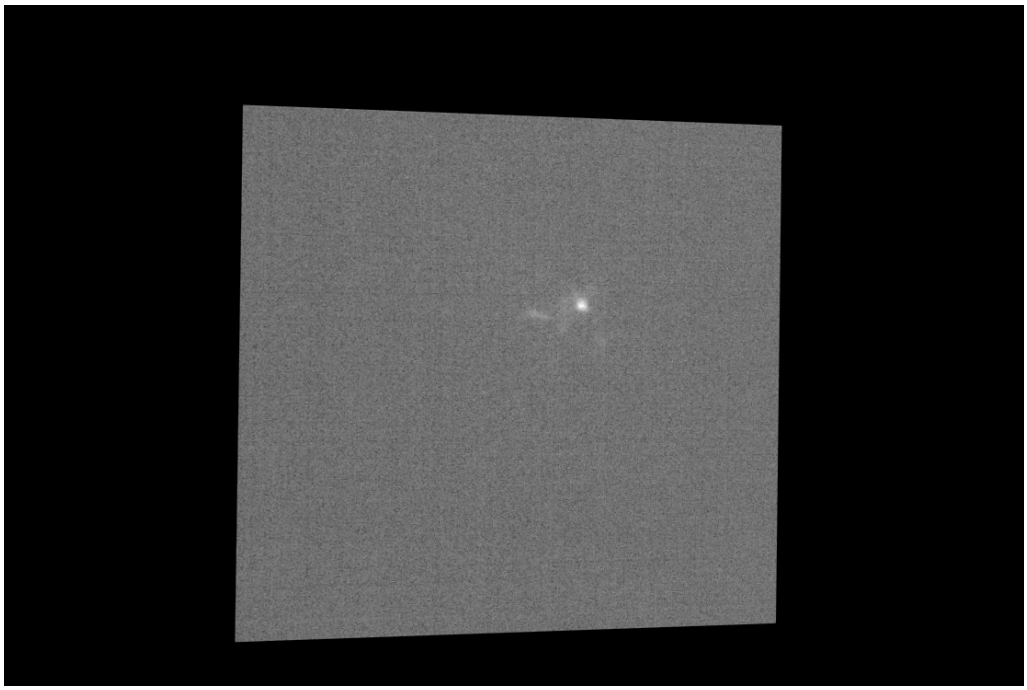

Figure A.2: The image modified by perspective transformation. The 512x512 image has been projected onto a larger canvas which matches the dimensions of the entire imaging surface. This allows images of any size to be adjusted correctly with the same perspective transformation.

The image is cropped to a region of interest which corresponds to an area on the target surrounding the beam. This region of interest remains constant for all images within a single day's data. The resulting reduction in image size speeds processing of all following steps. A "background" region of the image far from the beam is also defined. The pixel values in this region are averaged to yield an estimate of the average background level of the image. This value is subtracted from every pixel in the image. Typical results of cropping and background subtraction can be seen in Figure A.3.

A Fourier transform is now applied to the entire image. A Gaussian filter in Fourier space rejects the highest frequencies in the image. The filter radius is ¼ the radius of the entire image; this value was chosen empirically to reduce high-frequency noise while leaving beam features largely intact. Additionally, a second Gaussian filter, typically of radius 0.5, rejects the lowest frequencies in the image. This eliminates vignetting and reduces the noise level near the beam. The resulting Fourier image is inverse transformed, and the real part is returned as the cleaned image (Figure A.4).

A thresholding step now takes place in order to reduce noise further. There are two typical operational modes: thresholding to a multiple of the noise standard deviation in order to reduce noise while leaving the beam largely intact, and thresholding to 50% of the image maximum in order to examine the behavior of the beam hot-spot. In either case, pixels with value below the threshold are not simply set to zero: to do so would yield a background of value zero, containing intermittent intense noise pixels of value slightly greater than the threshold value. This type of

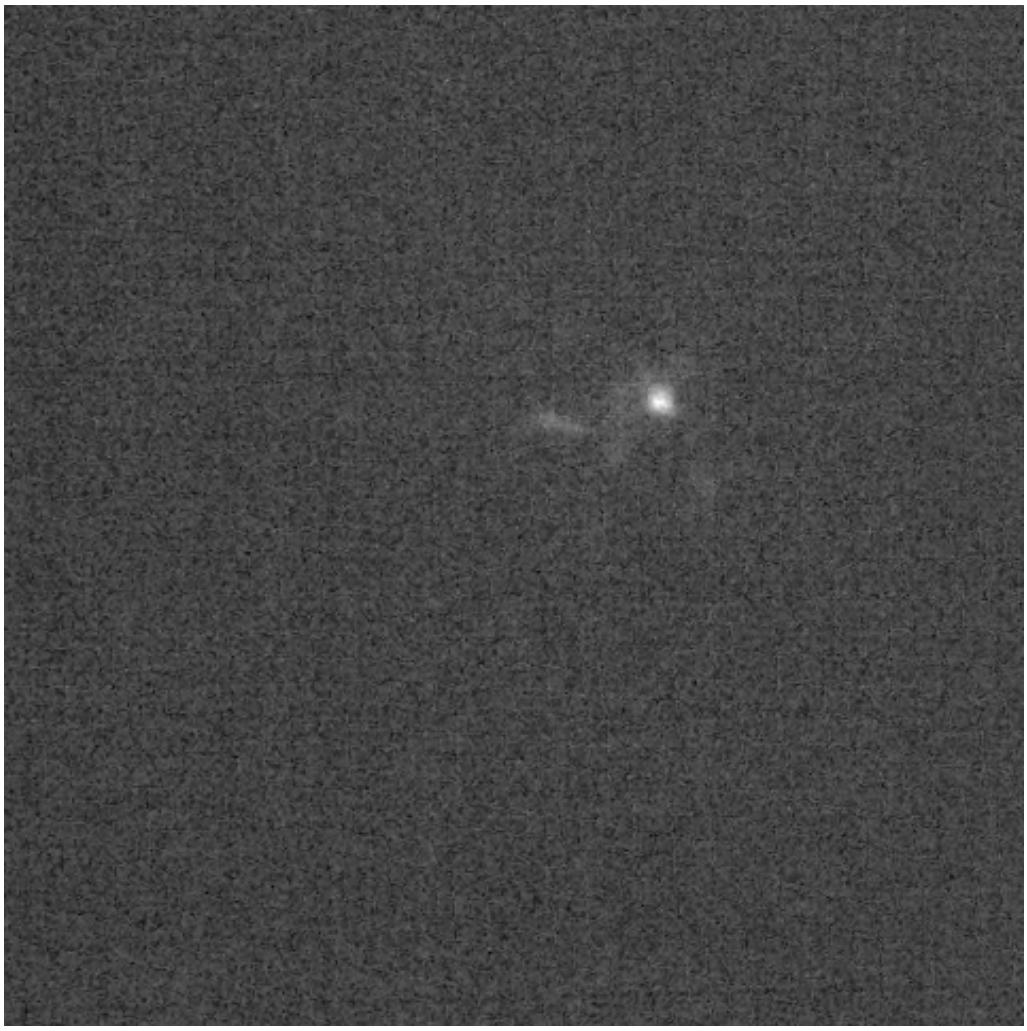

Figure A.3: The image after cropping and background subtraction.

Figure A.4: The image after the bandpass filter. Notice the significantly reduced level of background noise.

noise is extremely disruptive to beam size algorithms. Instead, the threshold value is subtracted from the entire image, and then any pixels with negative value are set to zero. In this case the remaining noise pixels have low values and do not contribute disproportionately to apparent beam size. Typical results of this procedure are displayed in Figure A.5.

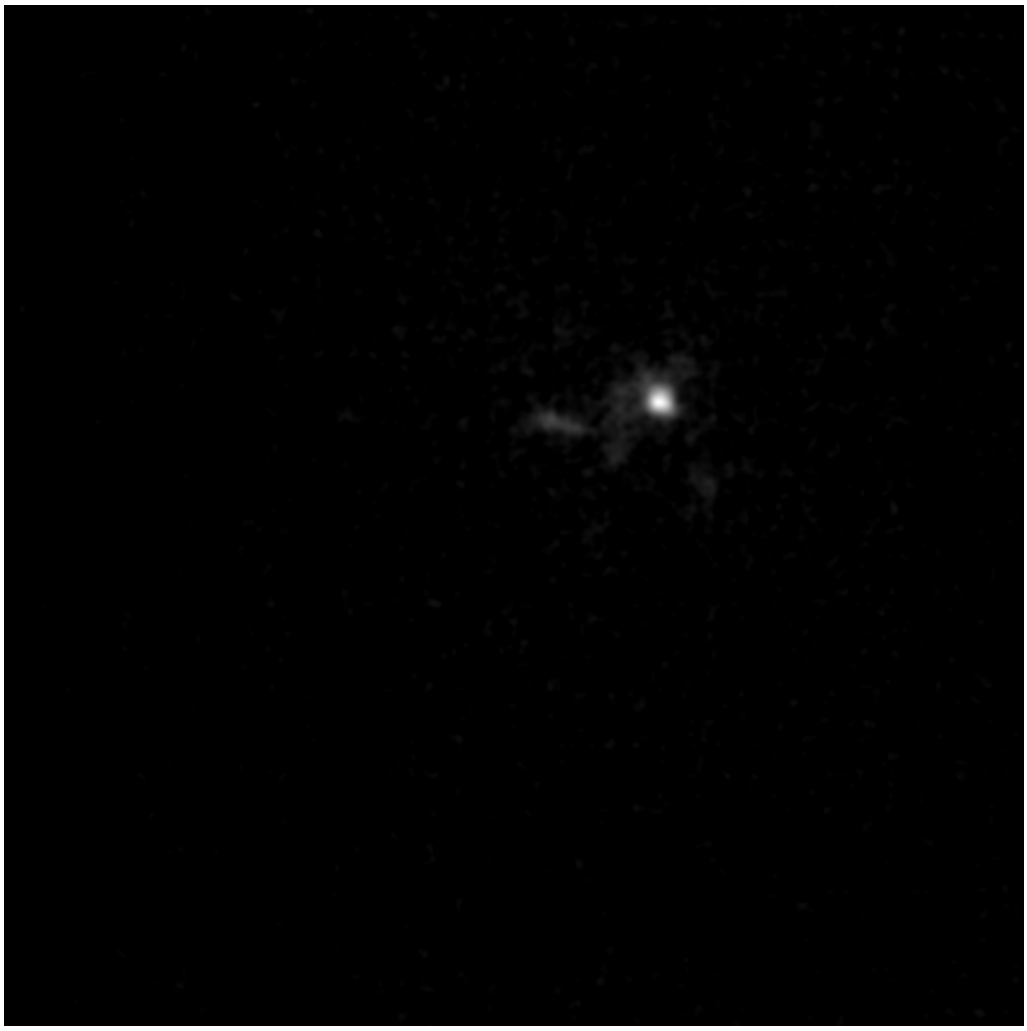

Figure A.5: The image after thresholding.

Finally, in the case of noise-deviation thresholding, there is often still some

remaining low-value noise far from the beam center (see Figure A.6). Since the RMS spot size metric is extremely sensitive to small amounts of noise far from the beam centroid, it is important to eliminate these pixels. In this case, a Difference of Gaussians (DoG) blob-detection algorithm is applied to the image.

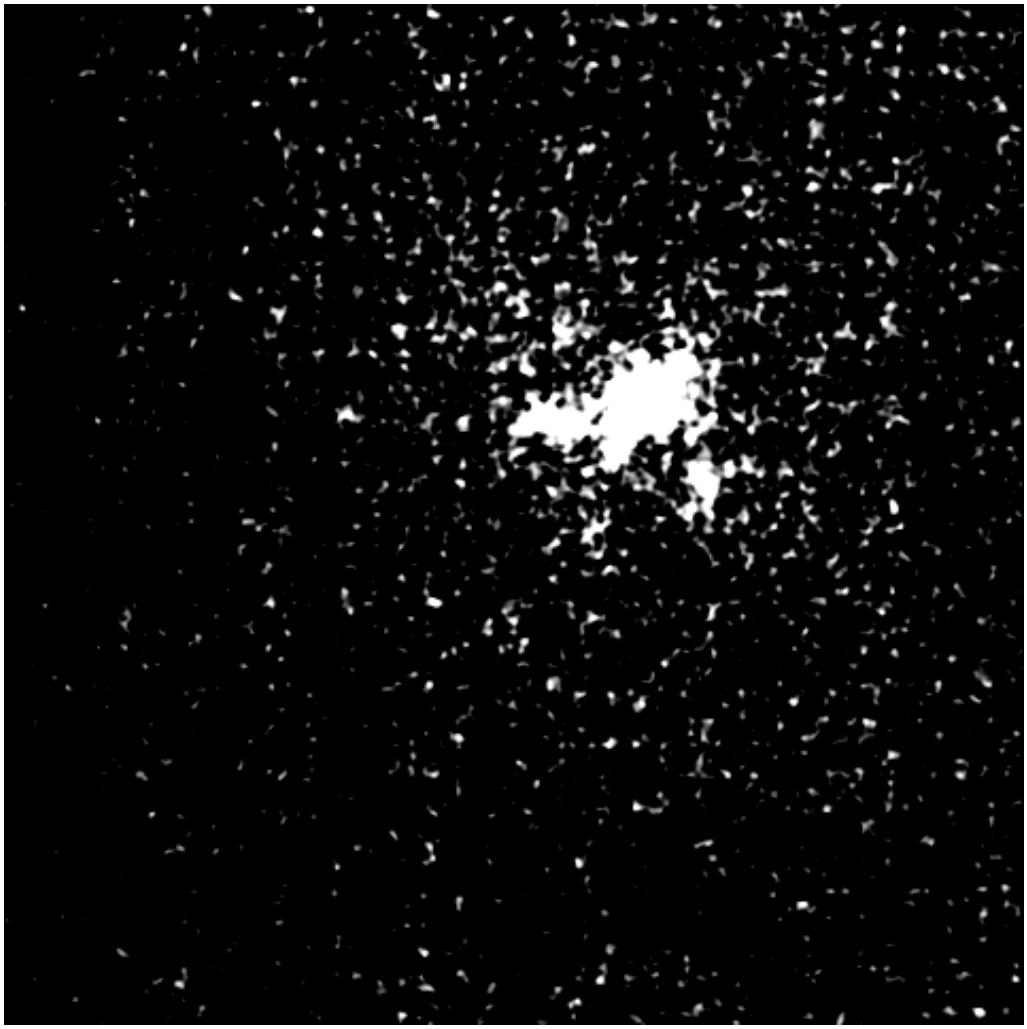

Figure A.6: The image after thresholding, contrast-enhanced in order to draw attention to low-amplitude noise.

A.1.1 Blob Detection

The DoG algorithm locates and estimates the size of bright spots on a dark background by convolving the image with successively larger Gaussian blur kernels, and taking the difference between successive blurred images. In regions of constant or near-constant amplitude, the amount of blur applied does not change the image much, so the difference is small. The difference image is dark and uniform in these regions. However, in regions where the image has edges, the amount of blurring strongly affects the size of the blurred spot. In these regions the difference image is bright. Blob location is determined by the location of a local maximum in the difference image; blob size is determined by the size of the Gaussian blur kernels which were used to detect the blob. The array of possible blob sizes is determined by the set of Gaussian kernels used to convolve the image: more discrete sizes leads to longer processing times and smaller blob size quantization error. For this reason, blob detection is not sufficiently precise to produce a true measurement of spot size.

Nevertheless, blob detection suffices to determine a reasonably-sized region of interest which excludes noise while including the beam. Every blob detected by the algorithm defines a circle with known position and radius, as visualized in Figure A.7. This radius is multiplied by three (empirically chosen), and the set of all pixels within the resulting circles forms the new region of interest. Pixels outside this region are set to zero, as in Figure A.8. For each image, the radius of the largest blob is reported for completeness. Typical results of this image cleaning procedure can be seen in Figure A.9.

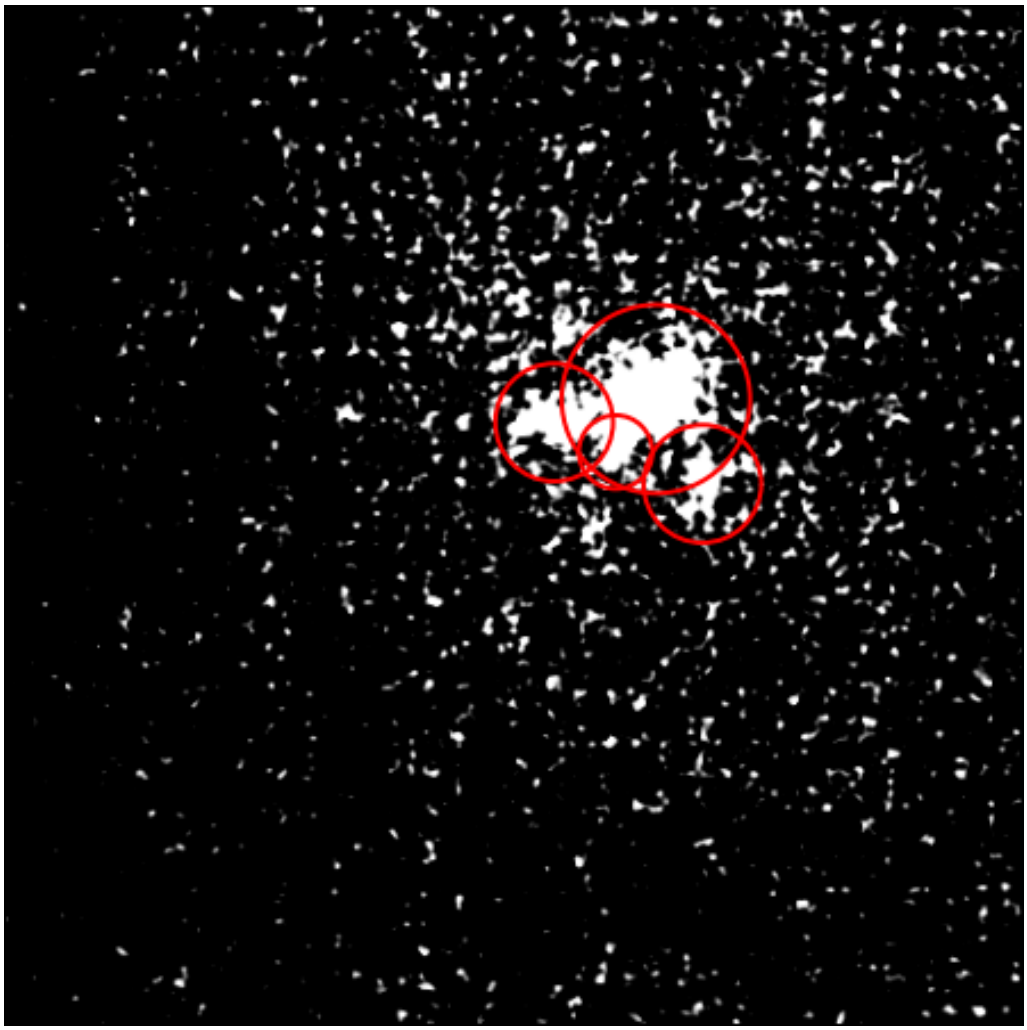

Figure A.7: Location and size of the blobs detected by the DoG blob-detection algorithm. The underlying image is contrast-enhanced.

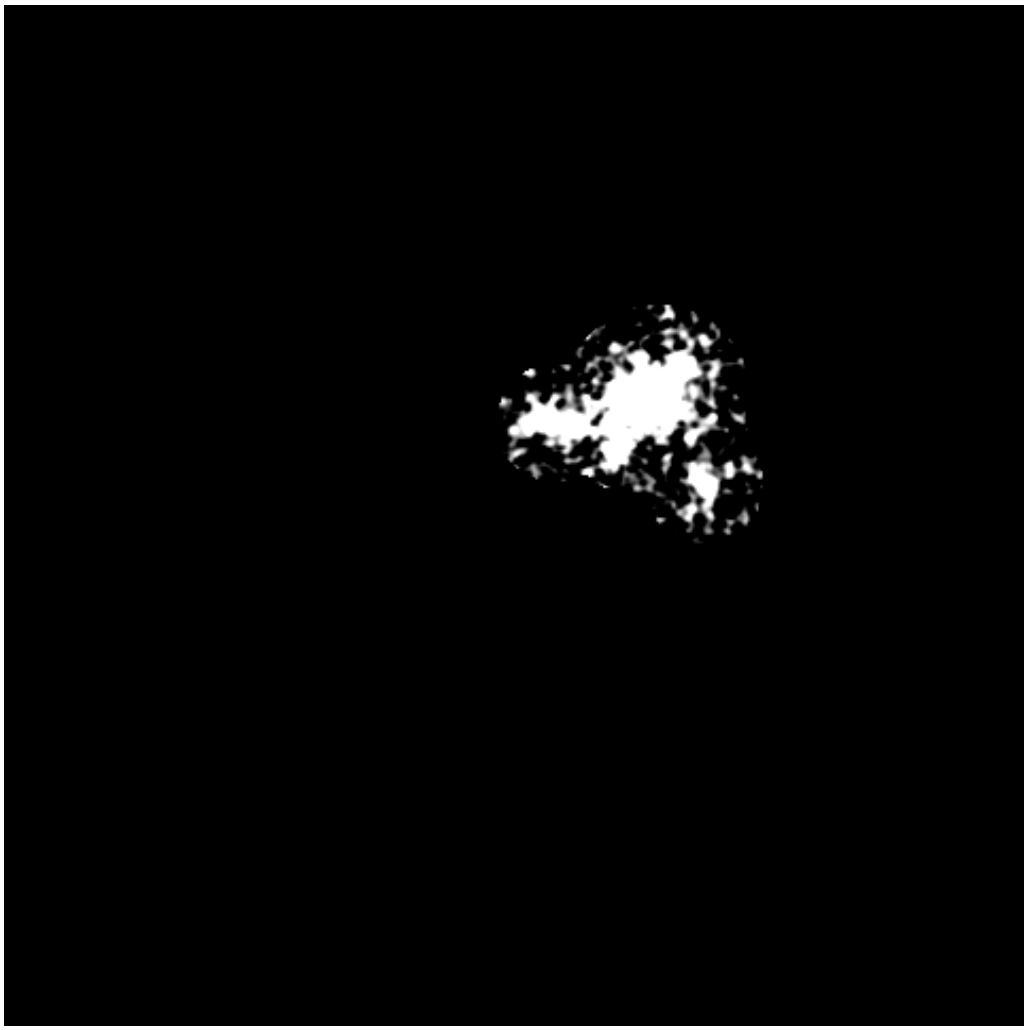

Figure A.8: Output of the DoG blob-detection algorithm. The image has been contrast-enhanced for visibility.

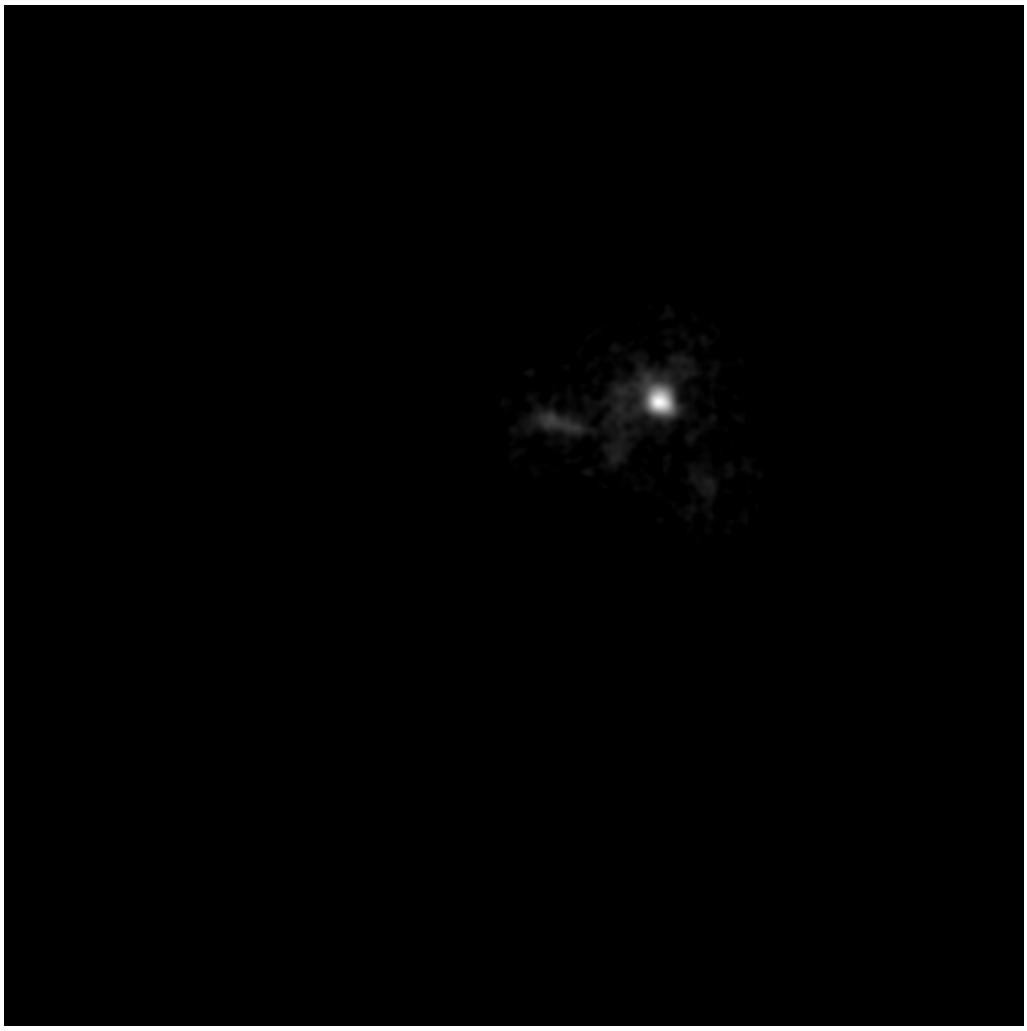

Figure A.9: Final image.

A.1.2 Beam Metrics

Proper beam analysis can begin now that image cleaning is done. The beam centroid is determined by calculating the first moment of the image in the x- and y-dimensions, as follows:

$$\alpha_0 = \frac{\sum P_{x,y}\alpha}{\sum P_{x,y}} \tag{A.1}$$

where α denotes either x or y.

The beam radius is then calculated in the x-, y-, and r-dimensions by calculating the second central moment of the image, as in the following equations:

$$R_\alpha = 2\sqrt{\frac{\sum P_{x,y}(\alpha - \alpha_0)^2}{\sum P_{x,y}}} \tag{A.2}$$

$$R_r = \sqrt{2}\sqrt{\frac{\sum P_{\vec{r}}|\vec{r} - \vec{r_0}|^2}{\sum P_{\vec{r}}}} \tag{A.3}$$

where $\vec{r} = \vec{x} + \vec{y}$ and $\vec{r_0} = \hat{x}x_0 + \hat{y}y_0$. The primary measurement is the radius in the r-dimension; the radius in the x- and y-dimensions are reported separately in order to detect beam asymmetry. The r-radius which is reported is $\sqrt{2}$ times the RMS radius of the beam. This metric was chosen because for a perfect Gaussian beam, it matches the $1/e^2$ intensity radius. It is also a commonly used definition of beam width throughout the literature, including the work of Siegman [68], the ISO standard for measuring laser beam quality (M-squared) [69], and the calculations of Andrews and Phillips [7].

Additionally, the 86.5% Power-In-The-Bucket (PIB) radius is reported. This is the radius of a circle centered on the beam centroid which contains 86.5% of the pixel value integrated over the entire image. Because it lacks the $|\vec{r}|^2$ factor, the PIB radius is not so sensitive to the presence of low-value pixels far from the centroid. It concentrates on the size of the central lobe of the beam while giving lower weight to the distribution of the wings. For a perfect Gaussian, the RMS matches the $1/e^2$ radius; for other beams, it is typically somewhat smaller.

A.1.3 Error Analysis

Error analysis has been performed for these procedures, by applying them to a series of noiseless images produced by simulation, to which artificial noise matching the spectrum and intensity distribution of real image noise has been added.

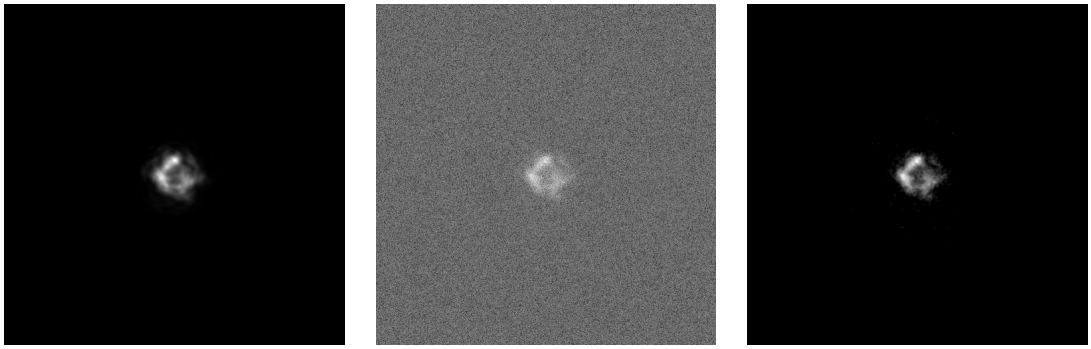

Table A.1: From left to right: the simulated beam without noise, with noise, and after image cleaning. Some low-amplitude portions of the beam are lost in exchange for eliminating the noise.

In this manner, the true r-radius can be measured under ideal conditions, and the error in determining the radius due to noise and beam cleaning can be assessed.

The results of this procedure are summarized in the following table:

	Without Cleaning	With Cleaning
Without Noise	0 %	-2.0 %
With Noise	634 %	-9.6 %

Table A.2: Percentage error in r-radius spot size determination relative to the noiseless simulated beam. The application of the beam measurement algorithm to the noiseless image produces zero error by definition. The presence of noise, in the absence of image cleaning, causes the beam size to be overestimated by a factor of more than 6. The image cleaning routines discussed above restore the accuracy of the beam size to within 10%.

The beam cleaning significantly reduces the noise-related error in beam size, while having only a small effect on the apparent beam size of an image without noise. There is a general tendency to underestimate the size of the beam. This is preferable to an overestimate, since small excesses of noise far from beam center can greatly inflate the apparent beam size.

Bibliography

[1] Rita Mahon, Christopher I. Moore, Harris R. Burris, Mike Ferraro, William S. Rabinovich, Linda M. Thomas, et al. Probability density of irradiance fluctuations observed over terrestrial ranges. *Applied optics*, 50(35):6476–6483, 2011.

[2] Tim Blackwell. Recent demonstrations of laser power beaming at DFRC and MSFC. In *BEAMED ENERGY PROPULSION: Third International Symposium on Beamed Energy Propulsion*, volume 766, pages 73–85. AIP Publishing, 2005.

[3] Phillip Sprangle, Bahman Hafizi, Antonio Ting, and Richard Fischer. High-power lasers for directed-energy applications. *Applied Optics*, 54(31):F201–F209, 2015.

[4] Andrey Nikolaevich Kolmogorov. The local structure of turbulence in incompressible viscous fluid for very large reynolds numbers. In *Dokl. Akad. Nauk SSSR*, volume 30, pages 299–303, 1941.

[5] Ronald L. Fante. Electromagnetic beam propagation in turbulent media. In *IEEE Proceedings*, volume 63, pages 1669–1692, 1975.

[6] R M Williams and C A Paulson. Microscale temperature and velocity spectra in the atmospheric boundary layer. *Journal of Fluid Mechanics*, 83(03):547–567, 1977.

[7] Larry C Andrews and Ronald L Phillips. *Laser beam propagation through random media*, volume 1. SPIE press Bellingham, WA, 2005.

[8] Christopher I Moore, Harris R Burris, Mena F Stell, Linda Wasiczko, Rita Mahon, William S Rabinovich, G Charmaine Gilbreath, William J Scharpf, et al. Atmospheric turbulence studies of a 16 km maritime path. In *Defense and Security*, pages 78–88. International Society for Optics and Photonics, 2005.

[9] J Peñano, B Hafizi, A Ting, and M Helle. Theoretical and numerical investigation of filament onset distance in atmospheric turbulence. *JOSA B*, 31(5):963–971, 2014.

[10] Joseph Peñano. Nonlinear focusing of ultrashort laser pulses in atmospheric turbulence. In *Propagation through and Characterization of Distributed Volume Turbulence and Atmospheric Phenomena*, pages PW2C–2. Optical Society of America, 2015.

[11] J Peñano, JP Palastro, B Hafizi, MH Helle, and GP DiComo. Self-channeling of high-power laser pulses through strong atmospheric turbulence. *Physical Review A*, 96(1):013829, 2017.

[12] V I Tatarskii. *The effects of the turbulent atmosphere on wave propagation.* 1971. trans. for NOAA by Israel Program for Scientific Translations, Jerusalem.

[13] R. Ball. The kolmogorov cascade, an entry in encyclopedia of nonlinear science (a. scott, ed.), 2004.

[14] EO Schulz-DuBois and I Rehberg. Structure function in lieu of correlation function. *Applied physics*, 24(4):323–329, 1981.

[15] A. V. Smol'yakov and V. M. Tkachenko. *The measurement of turbulent fluctuations.* Springer-Verlag, 1980.

[16] SF Clifford. The classical theory of wave propagation in a turbulent medium. In *Laser beam propagation in the atmosphere*, pages 9–43. Springer, 1978.

[17] Andrey Nikolaevich Kolmogorov. Dissipation of energy in locally isotropic turbulence. In *Dokl. Akad. Nauk SSSR*, volume 32, pages 16–18, 1941.

[18] Theodore von Karman. Progress in the statistical theory of turbulence. *Proceedings of the National Academy of Science of the United States of America*, 34(11):530, 1948.

[19] R. J. Hill and S. F. Clifford. Modified spectrum of atmospheric temperature fluctuations and its application to optical propagation. *JOSA*, 68(7):892–899, 1978.

[20] Geoffrey Ingram Taylor. The spectrum of turbulence. In *Proceedings of the Royal Society of London A: Mathematical, Physical, and Engineering Studies*, volume 164, pages 476–490. The Royal Society, 1938.

[21] DC Collis and MJ Williams. Two-dimensional convection from heated wires at low reynolds numbers. *Journal of Fluid Mechanics*, 6(3):357–384, 1959.

[22] Ting-i Wang, G R Ochs, and S F Clifford. A saturation-resistant optical scintillometer to measure c_n^2. *J. Opt. Soc. Am.*, 68(3):334–338, Mar 1978.

[23] B A H Dieterink. *LAS Mk II Scintillometer Manual.* Kipp and Zonen, 2001.

[24] A Consortini, Yi Yi Sun, C Innocenti, and Zhi Ping Li. Measuring inner scale of atmospheric turbulence by angle of arrival and scintillation. *Optics communications*, 216(1):19–23, 2003.

[25] Walter Koechner. *Solid-state laser engineering*, volume 1. Springer, 2013.

[26] Larry C Andrews, Ronald L Phillips, Cynthia Y Hopen, and MA Al-Habash. Theory of optical scintillation. *JOSA A*, 16(6):1417–1429, 1999.

[27] Phillip Sprangle, Antonio Ting, Joseph Penano, Richard Fischer, and Bahman Hafizi. Incoherent combining and atmospheric propagation of high-power fiber lasers for directed-energy applications. *Quantum Electronics, IEEE Journal of*, 45(2):138–148, 2009.

[28] Marc Sarazin and F Roddier. The eso differential image motion monitor. *Astronomy and Astrophysics*, 227:294–300, 1990.

[29] Robert Q Fugate, JM Spinhirne, JF Moroney, RA Cleis, MD Oliker, BR Boeke, BL Ellerbroek, CH Higgins, RE Ruane, DW Swindle, et al. Two generations of laser-guide-star adaptive-optics experiments at the starfire optical range. *JOSA A*, 11(1):310–324, 1994.

[30] C. Nelson, S. Avramov-Zamurovic, R. Malek-Madani, O. Korotkova, R. Sova, and F. Davidson. Measurements and comparison of the probability density and covariance functions of laser beam intensity fluctuations in a hot-air turbulence emulator with the maritime atmospheric environment. In *SPIE Optical Engineering+ Applications*, pages 851707–851707. International Society for Optics and Photonics, 2012.

[31] Christopher I Moore, Harris R BurrisJr, William S Rabinovich, Linda Wasiczko, Lee A Swingen, Rita Mahon, Mena F Stell, GC Gilbreath, William J Scharpf, et al. Overview of NRL's maritime laser communication test facility. In *Optics & Photonics 2005*, pages 589206–589206. International Society for Optics and Photonics, 2005.

[32] Ronald L Phillips and Larry C Andrews. Measured statistics of laser-light scattering in atmospheric turbulence. *JOSA*, 71(12):1440–1445, 1981.

[33] Laurent Jolissaint. Optical turbulence generators for testing astronomical adaptive optics systems: A review and designer guide. *Publications of the Astronomical Society of the Pacific*, 118(847):1205–1224, 2006.

[34] Christopher C Davis, Yimin Zhang, Mark L Plett, Penelope Polak-Dingels, Pierre R Barbier, and David W Rush. Characterization of a liquid-filled turbulence simulator. In *SPIE's International Symposium on Optical Science, Engineering, and Instrumentation*, pages 38–49. International Society for Optics and Photonics, 1998.

[35] Arun K Majumdar, John A DiUbaldo, and Alenka Brown-VanHoozer. Laboratory simulation of atmospheric turbulence for laser propagation: design and characterization. In *SPIE's International Symposium on Optical Science, Engineering, and Instrumentation*, pages 50–56. International Society for Optics and Photonics, 1998.

[36] Onur Keskin, Laurent Jolissaint, and Colin Bradley. Hot-air optical turbulence generator for the testing of adaptive optics systems: principles and characterization. *Applied optics*, 45(20):4888–4897, 2006.

[37] R. Salam, N. Lascoux, E. Salmon, R. Ackermann, J. Kasparian, and J.-P. Wolf. Propagation of laser filaments through an extended turbulent region. *Applied Physics Letters*, 91(17):–, 2007.

[38] W Nelson, J P Palastro, C Wu, and C C Davis. Enhanced backscatter of optical beams reflected in turbulent air. *JOSA A*, 32(7):1371–1378, 2015.

[39] Stuart W Churchill and Humbert HS Chu. Correlating equations for laminar and turbulent free convection from a horizontal cylinder. *International Journal of Heat and Mass Transfer*, 18(9):1049–1053, 1975.

[40] Steven Fiorino. Satellite and radar measurement of CT^2, Cn^2, and Cv^2. In *Propagation Through and Characterization of Distributed Volume Turbulence*, pages PM1E–1. Optical Society of America, 2014.

[41] F H Champagne, C A Friehe, J C LaRue, and J C Wyngaarde. Flux measurements, flux estimation techniques, and fine-scale turbulence measurements in the unstable surface layer over land. *Journal of the atmospheric sciences*, 34(3):515–530, 1977.

[42] Philip Sprangle, JR Peñano, and Bahman Hafizi. Propagation of intense short laser pulses in the atmosphere. *Physical Review E*, 66(4):046418, 2002.

[43] JR Peñano, P Sprangle, B Hafizi, A Ting, DF Gordon, and CA Kapetanakos. Propagation of ultra-short, intense laser pulses in air. *Physics of Plasmas*, 11(5):2865–2874, 2004.

[44] Robert W. Boyd. *Nonlinear Optics*. Academic Press, 2003.

[45] Jean-Claude Diels and Wolfgang Rudolph. *Ultrashort laser pulse phenomena*. Academic press, 2006.

[46] A Braun, G Korn, X Liu, D Du, J Squier, and G Mourou. Self-channeling of high-peak-power femtosecond laser pulses in air. *Optics letters*, 20(1):73–75, 1995.

[47] W Liu and SL Chin. Direct measurement of the critical power of femtosecond ti: sapphire laser pulse in air. *Optics Express*, 13(15):5750–5755, 2005.

[48] See Leang Chin. *Femtosecond laser filamentation*, volume 55. Springer, 2010.

[49] SL Chin, A Talebpour, J Yang, S Petit, VP Kandidov, OG Kosareva, and MP Tamarov. Filamentation of femtosecond laser pulses in turbulent air. *Applied Physics B*, 74(1):67–76, 2002.

[50] Magali Durand, Aurélien Houard, Bernard Prade, André Mysyrowicz, Anne Durécu, Bernard Moreau, Didier Fleury, Olivier Vasseur, Hartmut Borchert, Karsten Diener, et al. Kilometer range filamentation. *Optics express*, 21(22):26836–26845, 2013.

[51] K Krushelnick, A Ting, CI Moore, HR Burris, E Esarey, P Sprangle, and M Baine. Plasma channel formation and guiding during high intensity short pulse laser plasma experiments. *Physical review letters*, 78(21):4047, 1997.

[52] W Liu, F Théberge, J-F Daigle, PT Simard, SM Sarifi, Y Kamali, HL Xu, and SL Chin. An efficient control of ultrashort laser filament location in air for the purpose of remote sensing. *Applied Physics B*, 85(1):55–58, 2006.

[53] Nicolas Berti, Wahb Ettoumi, Sylvain Hermelin, Jérôme Kasparian, and Jean-Pierre Wolf. Nonlinear synthesis of complex laser waveforms at remote distances. *Physical Review A*, 91(6):063833, 2015.

[54] PL Kelley. Self-focusing of optical beams. *Physical Review Letters*, 15(26):1005, 1965.

[55] Robert R Alfano et al. The supercontinuum laser source. 1989.

[56] Philip E. Ciddor. Refractive index of air: new equations for the visible and near infrared. *Appl. Opt.*, 35(9):1566–1573, Mar 1996.

[57] Valeriy Petrovich Kandidov, Ol'ga Grigor'evna Kosareva, Mikhail Pavlovich Tamarov, A Brodeur, and SL Chin. Nucleation and random movement of filaments in the propagation of high-power laser radiation in a turbulent atmosphere. *Quantum electronics*, 29(10):911, 1999.

[58] R Ackermann, G Méjean, J Kasparian, J Yu, E Salmon, and J-P Wolf. Laser filaments generated and transmitted in highly turbulent air. *Optics letters*, 31(1):86–88, 2006.

[59] Aurélien Houard, Michel Franco, Bernard Prade, Anne Durécu, Laurent Lombard, Pierre Bourdon, Olivier Vasseur, Bruno Fleury, Clélia Robert, Vincent Michau, et al. Femtosecond filamentation in turbulent air. *Physical Review A*, 78(3):033804, 2008.

[60] B Hafizi, P Sprangle, and J Peñano. Quality of a laser beam in a nonlinear turbulent medium. In *Plasma Science, 2005. ICOPS'50. IEEE Conference Record-Abstracts. IEEE International Conference on*, pages 136–136. IEEE, 2005.

[61] Unpublished HELCAP simulation, 2015.

[62] B Hafizi, JR Peñano, JP Palastro, RP Fischer, and G DiComo. Laser beam self-focusing in turbulent dissipative media. *Optics letters*, 42(2):298–301, 2017.

[63] Donna Strickland and Gerard Mourou. Compression of amplified chirped optical pulses. *Optics communications*, 56(3):219–221, 1985.

[64] M Pessot, P Maine, and G Mourou. 1000 times expansion/compression of optical pulses for chirped pulse amplification. *Optics communications*, 62(6):419–421, 1987.

[65] M D Perry, D Pennington, B C Stuart, G Tietbohl, J A Britten, C Brown, S Herman, B Golick, M Kartz, J Miller, et al. Petawatt laser pulses. *Optics Letters*, 24(3):160–162, 1999.

[66] G DiComo, M Helle, J Peñano, A Ting, A Schmitt-Sody, and J Elle. Implementation of a long range, distributed-volume, continuously variable turbulence generator. *Applied Optics*, 55(19):5192–5197, 2016.

[67] Mathieu Aubailly, Mikhail A. Vorontsov, Gary W. Carhart, and Michael T. Valley. Video enhancement through automated lucky-region fusion from a stream of atmospherically-distorted images. In *Computational Optical Sensing and Imaging*, page CThC3. Optical Society of America, 2009.

[68] Anthony E Siegman. How to (maybe) measure laser beam quality. In *Diode Pumped Solid State Lasers: Applications and Issues*, page MQ1. Optical Society of America, 1998.

[69] Lasers and laser-related equipment – test methods for laser beam widths, divergence angles and beam propagation ratios – part 1: Stigmatic and simple astigmatic beams. standard, International Organization for Standardization, Geneva, CH, 2005.